1.61.2

Spectroscopic Signatures from First Principles Calculations: from surface adsorbates to liquids and polymers

Dissertation
zur Erlangung des Grades

"Doktor der Naturwissenschaften"

dem Fachbereich Physik
der Johannes Gutenberg-Universität Mainz
vorgelegt von

Tatiana Murakhtina
geboren in Udarnik, Russia

Mainz 2007

Contents

List of abbreviations

BLYP:	Becke Lee Yang Parr
BO:	Born-Oppenheimer
CPMD:	Car Parrinello molecular dynamics
CSGT:	continuous set of gauge transformations
DFT:	density functional theory
DFPT:	density functional perturbation theory
GC:	gradient correction
GIAO:	gauge-including atomic orbital
HK:	Hohenberg-Kohn
IGLO:	individual gauges for localized orbitals
KS:	Kohn-Sham
LDA:	local density approximation
MDPA:	methylenediphosphonic acid
NMR:	nuclear magnetic resonance
ppm:	parts per million
PW:	plane wave
PBE:	Perdew-Burke-Ernzerhoff
PVPA:	polyvinyl phosphonic acid
Ry:	Rydberg
TMS:	tetramethylsilane
VC:	virtual cell

Chapter 1

Introduction

The determination of local structural and dynamical properties of molecular systems and supramolecular assemblies has always been and still is a challenge for modern physics and chemistry. Many advanced techniques are capable of contributing to this quest, some of the most prominent being X-ray (1) and neutron scattering (2), electron crystallography (3; 4), infrared (IR) spectroscopy (5) and nuclear magnetic resonance (NMR) spectroscopy (6; 7).

It has become increasingly common to supplement experimental data with numerical simulations. Classical molecular dynamics (MD) techniques are performed for structures obtained via X-ray, electron diffraction or solution NMR methods in order to test their conformational stability (8; 9); quantum chemical calculations of vibrational frequencies can often help interpreting IR spectra (5; 10; 11; 12) and understanding the dynamical properties of condensed systems (10; 13; 14). For magnetic resonance experiments, accompanying ab-initio calculations have become standard for isolated molecules (15; 16; 17), and are becoming increasingly popular also for the solid state (18; 19; 20; 21; 22), as well as for liquids and solutions (23; 24; 25; 26).

In this work, three molecular systems of very different types are investigated

by means of first principles electronic structure calculations based on density functional theory (DFT) under periodic boundary conditions. Their microscopic structure and local conformations, like the hydrogen bonding networks, are obtained by ab-initio molecular dynamics simulations and further characterized by the calculations of spectroscopic responses. For all considered systems, the focus of the calculations lies in understanding the local hydrogen bonding network. This is one of the most prominent structural driving forces, which together with steric constraints and entropy leads to a specific equilibrium state, which defines the physical and chemical properties of a variety of materials. The computed spectroscopic signatures of local structural conformations and hydrogen bonding arrangements are used to get a deeper insight into a range of physical processes of interest which are investigated in this work: water adsorption on metallic surfaces, solvation of ions in aqueous solution and proton transfer in proton conducting polymers which are prototypes of fuel cell membrane materials. The calculation of response properties also allows for a direct comparison with experimental spectra, enabling a dialog between experiment and theory.

This thesis is divided into seven chapters including the introduction and the conclusion. In the chapters 2 and 3, the general theory of the quantum mechanical description used throughout this work and the theoretical framework for calculations of particular response properties, the atomic harmonic frequencies and NMR chemical shifts, are outlined.

Chapters 4, 5 and 6 are devoted to applications of these techniques, namely to the initial steps of water adsorption on metallic nickel surfaces, to the aqueous solvation of hydrochloric acid (HCl) and to first principles analysis of a proton conducting polymer system.

The ab-initio simulation of the structure and properties of water, where the dynamically fluctuating hydrogen bond network is the central structural driv-

ing force, is a difficult problem in computational chemistry. Important progress has been achieved in the direct simulation of the molecular structure in the liquid phase (27; 28), the understanding of its IR spectrum (10; 29), the Raman spectrum of ice (30), the NMR parameters in the liquid and supercritical phases (23; 24), and last but not least the hydrogen bond network of water on surfaces (31; 32; 33).

The peculiarity of surfaces is that they mix properties from both cases. Towards one side, the atoms and electrons feel the environment of the bulk crystalline phase. Towards the other side, the last atomic layer at the surface has unsaturated interface bonds, as in the case of an isolated molecule. Therefore, a proper theoretical model for an interface has to consider the Bloch character of the electrons in two dimensions, as well as the unsaturated bonding situation of the surface atoms. In order to achieve this, the most common representation of a real surface is a periodically repeated slab. In this model, the bulk phase is represented by atomic layers with a thickness of a few atoms which are separated from their periodic images by several angstroms of vacuum (34; 35).

In Chapter 4, the adsorption of water oligomers (molecule, dimer and trimer), both on a perfect (flat) surface and on a surface with a periodic step defect is investigated (33; 36). Of particular interest is the interplay of hydrogen bonding between the water molecules and the water-surface interaction, and the role of the step defect. The energetics, the electronic density rearrangements and the changes in IR vibrational modes and frequencies upon adsorption are determined. The computed IR spectra allow us to distinguish between relevant adsorption sites (perfect surface or the step defect) and sizes of adsorbed clusters. The results obtained by ab-initio calculations are verified by a comparison of calculated IR frequencies for adsorbed water clusters with corresponding experimental values from literature (37).

1. INTRODUCTION

In surface chemistry, IR spectroscopy is one of the the most widely used spectroscopic methods for the characterization of processes in heterogeneous catalysis. Direct monitoring of the interaction between adsorbed molecules and the catalysts, including the nature of adsorbed intermediates and analysis of products of catalytic reactions becomes available through *in-situ* experiments, where realistic catalytic conditions, i.e. pressures and temperatures, can be applied (38; 39).

As an example, the infrared absorption spectrum in the intramolecular OH stretching region reflects both a distribution of hydrogen-bond strengths and a size distribution of hydrogen-bonded water aggregates. This makes IR spectrometry a very suitable experimental method for characterization of water adsorption.

Another class of systems in which water and its H-bonding abilities is of central importance are aqueous solutions.

The solvation of molecules and ions is currently a very active field of research due to its high importance for a broad range of chemical, biological, and physical processes which take place in solution. The full microscopic structure of solutions is directly accessible from first principles molecular dynamics simulations (27; 28; 40). However, the size of systems which can be treated by ab-initio MD methods is limited by five hundred atoms. Hence, it is important to check such simulations for errors due to finite-size effects. For liquid water, it has been found that finite-size effects are of minor importance compared to the effects of other computational parameters such as temperature and the choice of exchange-correlation functional (41). The immediate comparison of ab-initio microscopic structure with experiment is however lacking with the excepting of the assignment of radial distribution functions to X-ray experimental data (8; 9). Beyond that, the theoretical prediction of spectroscopic parameters can provide an improved understanding of experimental findings (25; 26; 42; 43; 44; 45; 46; 47; 48).

Although neutron and x-ray scattering techniques have considerably increased

our knowledge about the geometry and charge distribution of water molecules in liquids, precise quantitative results are still lacking due to difficulties in extracting accurate and unambiguous information from the experimental data (49; 50; 51). Complementary to this, NMR experiments are able to probe local structure of solutions. While magnetic resonance techniques cannot provide the full structure in terms of three-dimensional atomic coordinates, the sensitivity to the local chemical environment of an atom is one of the key advantages of this method. Therefore, NMR is well suited to investigate molecular and supramolecular systems in solutions and their mechanisms of structure formation (52; 53; 54; 55; 56; 57; 58; 59).

In this context, Chapter 5 presents a combined experimental and ab-initio study of the ^{1}H NMR chemical shift resonance of aqueous hydrochloride (HCl) solution (60). Apart from pure water as a reference system, acid solutions at two concentrations are considered. Due to the very fast molecular motion at ambient conditions, there is a steady exchange of the water molecules between the hydronium ions, the chlorine solvation shells, and the regular water. Hence, the NMR experiment only shows a single resonance line, which is the statistical average over the water molecules in these three categories. From the first-principles calculations, however, the individual ^{1}H NMR signatures of the different complexes are available, which allowing for the clarification of the origin of the computed chemical shift distributions. It is shown that the contributions of Eigen and Zundel ions, regular water molecules and the chlorine solvation shell to the ^{1}H NMR resonance line are actually very distinct and almost independent on the acid concentration. The average chemical shifts are in very good agreement with experiment for both diluted and concentrated acid solutions.

The third system studied in this work, Chapter 6, consists of a proton conducting polymer which is a prototype for fuel cell membrane materials.

1. INTRODUCTION

In proton conducting materials, the interplay of hydrogen bonding networks and local molecular mobility has direct implications for industrial applications (61; 62). Their major use lies in the field of fuel cell technologies, on which the quest for clean portable energy sources has focused in the past decade. Among various fuel cell technologies, proton exchange membrane fuel cells (PEMFC) are one of the most promising power sources (63). Investigations in this area are focused on the development of flexible fuel cells, which could ideally operate with hydrogen gas, or alternatively other hydrogen-rich fuels such as methanol. Other challenges in the search for the optimal fuel cell membrane material are the high operating temperature of the cell, as well as the effect of carbon monoxide, which degrades the efficiency of the fuel cell catalyst. These questions are intrinsically linked with the microscopic structure and dynamics of the membrane. This involves in particular the interplay of hydrogen bonding networks, defects therein, and the resulting mobility of protons (63; 64).

There are two important mechanisms which govern the proton transport in the proton conducting membrane. According to the first one known as Grotthus mechanism, proton transfer occurs between acid groups donated protons and through reorganization of hydrogen bonds. The other mechanism involves a vehicle-style migration (65; 66), by which the proton is transported with the aid of carriers such as water in the form of H_3O^+. In promising candidates for proton exchange membranes, the Grotthus-like mechanism of proton transfer should dominate, since the difficulty in maintaining a high level of hydration above the boiling temperature of water significantly limits the applicability of the up to date fuel cells.

Supramolecular polymeric systems are extremely complex, both in structure and dynamics – not to mention their functionality. In order to investigate such systems with magnetic resonance methods, a great deal of knowledge regarding

the relationships between structure, atomistic dynamics and spectroscopic properties is crucial (67). This is particularly true if magnetic parameters such as chemical shifts or spin-spin couplings (6; 7) are to be used as sources of information. Therefore, a clear validation of the signatures of condensed phase packing effects both in NMR experiment and in quantum-chemical calculations is one of the arguments for the consistency in descriptions of such complex materials.

While NMR in liquid-state is a widespread routine characterisation method for many areas of science and medicine, its application to solid-state systems is not as frequent. This is partially due to the higher requirements concerning the experimental setup, as well as the complexity of the underlying theory. In particular, there are strong anisotropic interactions in solids, which give rise to a line broadening in the NMR spectra. However, in the last decades, important progress has been made in this field, notably regarding magic-angle-spinning (MAS) techniques, which are capable of averaging parts of the anisotropic interactions, hence reducing the experimental line widths. Using those novel techniques, both an increase in resolution and in sensitivity could be achieved, leading to reliable experimental measurements of individual NMR resonances in the solid state, especially for ^{1}H chemical shifts (54; 55; 56; 64; 68; 69; 70).

In this project, poly(vinyl phosphonic acid) is chosen as a model system to study the local structure and the proton conducting mechanism in phosphonic acid tethered polymers, since it contains a high concentration of acid groups and adopts a simple structure. It forms a strong hydrogen bonding network involving both P=O and P-OH as proton acceptor and proton donor groups. The hydrogen bonding between acidic groups is the most plausible candidate for the short-range proton transfer, which will in turn lead to a percolation phenomenon and long-range proton conduction. Therefore, the work is focused on the description of *local* H-bonding network and on calculations of ^{1}H NMR signatures of regular

acidic groups and polymer defects which may affect the proton conduction. Three modifications of the polymer: PVPA with regular POH groups, with an anhydride defect (resulting from the "condensation" of two phosphonic acid groups) and with a negatively charged (deprotonated) acidic group are investigated at two different temperatures (71). The molecular dynamics simulations reveal that deprotonation defects are trapped by anhydrides, which means that anhydrides may inhibit proton conduction in two ways, first via reducing the number of available OH groups, and secondly by immobilizing proton vacancies, which may occur in PVPA by spontaneous dissociation of phosphonic acid. Spectroscopic calculations provide chemical shift signatures of regular acidic groups and the neutral and negatively charged anhydride defects. The computed high-frequency shift for the anhydrides defects with respect to regular PVPA and their temperature dependence trends are consistent with experimental data obtained by Young Joo Lee in her high resolution solid-state NMR studies (71). According the ab-initio spectroscopic calculations, the new peak appearing in the experimental proton NMR spectra at lower temperature is assigned to a combination of neutral and charged anhydride defects.

Chapter 2

Density functional theory (DFT)

2.1 General

In the following sections, a brief overview will be given of the theories underlying the quantum mechanical description of matter used throughout this work.

When it comes to the calculations of the properties of matter through a numerical description of the atoms and electrons, a theoretical framework is needed to represent them in a suitable way. In this work, the density functional theory (DFT) approach in combination with gradient corrected exchange-correlation energy functionals is chosen (72; 73; 74; 75). A plane wave representation of the electronic structure is used together with the pseudopotential approximation. In combination with molecular dynamics (MD) simulations, this allows good statistical sampling and the efficient calculations of energetic, structural, dynamical and spectroscopic properties of matter, especially in the condensed phase.

The starting point is the Schrödinger equation, which is transformed to simplified formulations that can be treated by computer programs. Then, several additional approximations which are used to lower the consumption of computational resources are introduced. Finally, the details of the implementation that

is used for this work are explained.

2.2 Born-Oppenheimer approximation

The Schrödinger equation for a system containing n electrons and N nuclei has the form of an eigenvalue problem:

$$\hat{H}\Psi(\mathbf{r}_1,..,\mathbf{r}_n,\mathbf{R}_1,..\mathbf{R}_N) = E\Psi(\mathbf{r}_1,..,\mathbf{r}_n,\mathbf{R}_1,..\mathbf{R}_N), \tag{2.1}$$

The many body Hamiltonian operator $\hat{H}$ can be written in dimensionless form:

$$\begin{aligned}\hat{H} \;=\; & \sum_i -\frac{1}{2}\nabla_i^2 + \sum_I -\frac{1}{2M_I}\nabla_I^2 + \frac{1}{2}\sum_{i\neq j}\frac{1}{|\mathbf{r}_i-\mathbf{r}_j|} + \\ & \frac{1}{2}\sum_{I\neq J}\frac{Q_I Q_J}{|\mathbf{R}_I-\mathbf{R}_J|} - \sum_{iI}\frac{Q_I}{|\mathbf{r}_i-\mathbf{R}_I|}.\end{aligned} \tag{2.2}$$

by atomic units transformation:

$$\mathbf{r} \to \frac{\mathbf{r}}{a}\,;\; E \to \frac{E}{E_a} \tag{2.3}$$

where

$$a \;=\; \frac{4\pi\epsilon_0\hbar^2}{m_e e^2}\,;\; E_a = \frac{\hbar^2}{m_e a^2} \tag{2.4}$$

The Bohr radius $a = 0.529\mathring{A} \equiv 1bohr$ and Hartree energy $E_a = 27.212eV \equiv 1Hartree$ are the new units for a length and an energy respectively. Here, e and m_e are the electronic charge and mass, $\hbar$ is Planck's constant divided by 2π, and ϵ_0 is the permittivity of vacuum. In Hamiltonian 2.2, $\mathbf{r}_i$ and $\mathbf{R}_I$ designate the dimensionless position operators acting on the electrons i and the nuclei I, respectively. M_I and Q_I are the masses and charges of the nuclei in atomic units.

The Born-Oppenheimer (BO) approximation (75; 76) is based on the fact that the mass of the ions is much larger than the mass of the electrons. This implies that the typical electronic velocities are much larger than the ionic ones, and that by consequence, the dynamical evolution can be decoupled. Energetically, the decoupling corresponds to a separation of the spectra in such a way that in practice the electrons are always in their instantaneous ground state. The total wavefunction is therefore written as the product of the nuclear and electronic parts:

$$\Psi(\mathbf{r}_1,\ldots,\mathbf{r}_n,\mathbf{R}_1,\ldots,\mathbf{R}_N) \;=\; \Psi^{\mathrm{el}}_{\mathbf{R}_1,\ldots,\mathbf{R}_N}(\mathbf{r}_1,\ldots,\mathbf{r}_n)\Psi^{\mathrm{i}}(\mathbf{R}_1,\ldots,\mathbf{R}_N) \quad (2.5)$$

where the electronic wavefunction $\Psi^{\mathrm{el}}_{\mathbf{R}_1,\ldots,\mathbf{R}_N}(\mathbf{r}_1,\ldots,\mathbf{r}_n)$depends only parametrically on the ionic position variables. In most cases, this approximation turns out to be justified. This adiabatic behaviour leads to separating the Schrödinger equation (2.1) into two decoupled ones: the Schrödinger equation for the electrons in the electrostatic field of the fixed nuclei, and the other one for the nuclei, in which the potential function is given by the electronic energy eigenvalue for the corresponding nuclear positions. A further approximation is to treat the nuclei like classical particles, so that in the end, the nuclear position operators can all be turned into position variables. The quantum effects are then limited to the electronic wavefunctions, which obey a simpler Schrödinger equation:

$$\hat{H}^{\mathrm{el}}\Psi^{\mathrm{el}}_{\mathbf{R}_1,\ldots,\mathbf{R}_N}(\mathbf{r}_1,\ldots,\mathbf{r}_n) \;=\; E^{\mathrm{el}}_{\mathbf{R}_1,\ldots,\mathbf{R}_N}\Psi^{\mathrm{el}}_{\mathbf{R}_1,\ldots,\mathbf{R}_N}(\mathbf{r}_1,\ldots,\mathbf{r}_n) \quad (2.6)$$

with

$$\hat{H}^{\mathrm{el}} \;=\; \sum_i -\frac{1}{2}\nabla_i^2 + \frac{1}{2}\sum_{i\neq j}\frac{1}{|\mathbf{r}_i-\mathbf{r}_j|} - \sum_{iI}\frac{Q_I}{|\mathbf{r}_i-\mathbf{R}_I|}. \quad (2.7)$$

The impact of the neglected quantum nature of the nuclei has been the subject of several recent theoretical investigations. Solvated excess proton in water and liquid hydrogen fluoride have been studied to estimate for the influence of zero-point energy and quantum tunneling on the proton solvation structure and diffusion (77; 78; 79). It was shown that the quantum mechanical delocalization of the hydrogens due to the zero-point vibrations is significant even at room temperature and can considerably alter the transport properties of an excess proton. However, the average structural properties of water are found to be almost unaffected by nuclear quantum effects. Also, the proton tunneling is shown to play an important role in phase transitions between various phases of ice (80) and for the structure of molecules or clusters with low isomerization barriers. The ab-initio path integral (PI) technique (81; 82) considers both nuclei and electrons as quantum particles and therefore allows us to treat these quantum effects. However, the computational demands of such PI molecular dynamics calculations are very high compared to the conventional DFT approach.

It is common to represent the interaction between nuclei and electrons, the last term in Eq. (2.7), by a generalized external potential $v_{\text{ext}}(\mathbf{r})$:

$$\hat{H}^{\text{el}} = \sum_i -\frac{1}{2}\nabla_i^2 + \frac{1}{2}\sum_{i\neq j}\frac{1}{|\mathbf{r}_i - \mathbf{r}_j|} + \sum_i v_{\text{ext}}(\mathbf{r}_i). \tag{2.8}$$

However, the exact quantum mechanical treatment of systems consisting of mutually interacting electrons is not possible at present, even within the BO approximation. Therefore, many concepts have been developed to overcome the complexity of the problem and to introduce physically reasonable simplifications.

In the following sections, one of the currently most popular theories will be described in detail. Its main idea is to take the electronic density instead of the wavefunction as the fundamental variable, thus reducing the degrees of freedom

drastically.

2.3 Hohenberg-Kohn and Kohn-Sham formalism

Density functional theory is based primarily on two theorems by Hohenberg and Kohn (72). The first one states:

> The all electron many body ground state wavefunction $\Psi(\mathbf{r}_1, \ldots, \mathbf{r}_n)$ of a system of n interacting electrons is a unique functional of the electronic density $n(\mathbf{r})$.

$$\Psi(\mathbf{r}_1, \ldots, \mathbf{r}_n) = \Psi[n(\mathbf{r})](\mathbf{r}_1, \ldots, \mathbf{r}_n) \tag{2.9}$$

$$n(\mathbf{r}) = \int d^3r_2 \int d^3r_3 \ldots \int d^3r_n \, |\Psi(\mathbf{r}_1, \ldots, \mathbf{r}_n)|^2 \tag{2.10}$$

The immediate consequence of this theorem is that all physically measurable quantities based on the electronic structure are in fact unique functionals of the electronic ground state density alone. Note that in general, there is no closed expression for these functionals.

In Eq. (2.7), the electronic Hamiltonian is completely determined by the Coulomb potential of the nuclei, which can be generalized to a universal external potential $v(\mathbf{r})$. Since the all electron wavefunction is well defined through the variational principle from this fixed Hamiltonian, this wavefunction can also be considered as a functional of this external potential. Thus, an equivalent formulation of the Hohenberg Kohn theorem states that the ground state electronic density determines the external potential. It shall be noted here that this external potential is not equal to the Coulomb potential created by the electronic

density itself, since this interaction is taken into account by the second term in Eq. (2.7). This theorem, however, can not be applied to any arbitrary density but only to those that result from the solution Ψ of the true Schrödinger equation. If a density can be obtained this way, it is said to be v-representable.

The second Hohenberg-Kohn theorem is essentially a minimum principle for the density. In contrast to the ordinary variational principle, which is formulated only with respect to the wavefunctions in combination with the energy functional, it states:

> For all v-representable densities n, the one that minimizes the energy functional with a given external potential is the ground state density, i.e. the density which corresponds to the solution of the Schrödinger equation.

The Hohenberg Kohn theorems show that it is possible in principle to calculate all quantities of physical interest from the electronic density alone. The remaining problem, how to find this density in practice, is more involved than it seems at first glance. In terms of wavefunctions, the total electronic energy is given by the expectation value of the Hamiltonian, Eq. (2.8):

$$E^{\mathrm{el}} = \mathcal{E}_{\mathrm{tot}}[\Psi] \quad = \quad \left\langle \Psi \left| \sum_i -\frac{1}{2}\nabla_i^2 + \frac{1}{2}\sum_{i\neq j}\frac{1}{|\mathbf{r}_i - \mathbf{r}_j|} + \sum_i v_{\mathrm{ext}}(\mathbf{r}_i) \right| \Psi \right\rangle \quad (2.11)$$

Here and in the following, calligraphic letters indicate a functional, whereas arabic ones designate a scalar quantity.

There are no closed expressions to calculate the first two parts of the total energy directly from the electronic density only, because the involved operators ∇_i and $\frac{1}{|\mathbf{r}_i - \mathbf{r}_j|}$ act on individual orbitals. In order to turn DFT into a practical tool for real calculations, Kohn and Sham (73) proposed an indirect approach to this functional by introducing a fictitious system of independent, non interacting

electrons. Their goal was to tune the electrical potential of this fictitious system in such a way that will eventually lead to the same electronic density as for the true system.

The idea is to define a new functional subtracting from Eq. (2.11) several terms calculated from the wave function of a non interacting gas of electrons with the same density as would have the exact solution of interacting particles. Let $|\varphi_i\rangle$ be the single particle wavefunctions of the independent electron gas. Its kinetic energy and density are:

$$\mathcal{T}[\varphi] = -\frac{1}{2}\sum_i \langle\varphi_i|\nabla^2|\varphi_i\rangle \tag{2.12}$$

$$n(\mathbf{r}) = \sum_i |\varphi_i(\mathbf{r})|^2. \tag{2.13}$$

This density is by construction equal to the one of the interacting electrons. If the density were a classical charge distribution, its interaction energy would be:

$$\mathcal{E}_{\mathrm{H}}[n] = \frac{1}{2}\int d^3r \int d^3r' \frac{n(\mathbf{r})n(\mathbf{r}')}{|\mathbf{r}-\mathbf{r}'|}. \tag{2.14}$$

$\mathcal{E}_H[n]$ is called the Hartree energy of the system. Finally, the interaction with the external potential remains:

$$\mathcal{E}_{\mathrm{ext}}[n] = \int d^3r\, v_{\mathrm{ext}}(\mathbf{r})n(\mathbf{r}) \tag{2.15}$$

Thus, the Kohn Sham energy functional of the fictitious non interacting system is:

$$\mathcal{E}_{\mathrm{KS}}[n] = \mathcal{T}[\varphi_{[n(\mathbf{r})]}] + \mathcal{E}_{\mathrm{H}}[n] + \mathcal{E}_{\mathrm{ext}}[n]. \tag{2.16}$$

Substitution of $\mathcal{T}$, $\mathcal{E}_{\mathrm{H}}$ and $\mathcal{E}_{\mathrm{ext}}$ in the energy functional of the interacting system introduces an error even when assuming identical electronic densities. The error contains all many body effects which cannot be treated in an exact way. This difference between the correct functional and the one which can be computed, $\mathcal{E}_{\mathrm{KS}}$, shall be compensated by the exchange-correlation functional $\mathcal{E}_{\mathrm{xc}}$ of the system, which still needs to be defined. Formally, it is given by the difference between Eq. (2.11) and Eq. (2.16):

$$\mathcal{E}_{\mathrm{xc}}[n] \quad = \quad \mathcal{E}_{\mathrm{tot}}[n] - \mathcal{E}_{\mathrm{KS}}[n]. \tag{2.17}$$

If this functional is known, one is able to compute the ground state density of interacting system by minimizing the total energy $\mathcal{E}_{\mathrm{KS}} + \mathcal{E}_{\mathrm{xc}}$. However, no closed expression has been found up to date for this. Several approximations for $\mathcal{E}_{\mathrm{xc}}$ proposed in literature are discussed in the next section.

The minimization of the total electronic energy functional must be done requiring the electronic wavefunctions be orthonormal to each other:

$$\langle \varphi_i | \varphi_j \rangle \quad = \quad \delta_{ij} \quad \forall i, j. \tag{2.18}$$

This is achieved by a Lagrange multiplier method (83) in combination with the stationarity condition for the energy functional:

$$\frac{\delta}{\delta \varphi_i(\mathbf{r})} \left(\mathcal{E}_{\mathrm{KS}} + \mathcal{E}_{\mathrm{xc}} \right) \quad = \quad 0. \tag{2.19}$$

This technique yields the Kohn Sham equations, which read:

$$\left[-\frac{1}{2}\nabla^2 + v_{\mathrm{H}}(\mathbf{r}) + v_{\mathrm{xc}}(\mathbf{r}) + v_{\mathrm{ext}}(\mathbf{r}) \right] \varphi_i(\mathbf{r}) \quad = \quad \epsilon_i \, \varphi_i(\mathbf{r}). \tag{2.20}$$

Here, ϵ_i are the eigenvalues of the KS Hamiltonian and the potentials are the derivatives of the corresponding energy functionals with respect to the density:

$$v_{\mathrm{H}}(\mathbf{r}) = \frac{\delta}{\delta n(\mathbf{r})}\,\mathcal{E}_{\mathrm{H}}[n] = \int d^3r' \frac{n(\mathbf{r}')}{|\mathbf{r}-\mathbf{r}'|} \tag{2.21}$$

$$v_{\mathrm{xc}}(\mathbf{r}) = \frac{\delta}{\delta n(\mathbf{r})}\,\mathcal{E}_{\mathrm{xc}}[n] \tag{2.22}$$

$$v_{\mathrm{ext}}(\mathbf{r}) = \frac{\delta}{\delta n(\mathbf{r})}\,\mathcal{E}_{\mathrm{ext}}[n] = \sum_I \frac{Q_I}{|\mathbf{r}-\mathbf{R}_I|} \tag{2.23}$$

Since these potentials still depend on the density, Eq. (2.20) has to be solved self-consistently. For a density computed from a set of trial wavefunctions, the potentials are calculated, and inserted in (2.20). Then, a better set of trial wavefunctions is obtained and the procedure is repeated until the changes in the orbitals and the density are neglegible according to a chosen convergence criterion.

At first sight, this single particle formulation due to Kohn and Sham has some similarity with a mean-field approach: the independent electrons move in the electrostatic field created by themselves and by the nuclei. However, the many body effects are taken into account through the exchange-correlation functional, even if there is no straightforward way to write it down.

In the Kohn-Sham formalism outlined above, electrons are treated as spinless particles, with the same Kohn-Sham orbital φ_i for the both spin-up and spin-down electrons. While this is appropriate for closed-shell systems, in which the total spin for each electronic shell is equal to zero, open-shell systems with one or more unpaired electrons require a different treatment. In such systems, it cannot be assumed that the spatial orbitals of doubly occupied electronic states are equal for spin-up and spin-down electrons. For the latter case, spin-polarized density

functional theory has been developed (74; 84) which assigns individual spatial orbitals to all spin-up and all spin-down states.

2.4 Exchange-correlation functionals

As already mentioned, DFT is formally an exact theory, but the difficulties related to the many body nature of the Schrödinger equation have only been reformulated in the exchange-correlation energy functional. To proceed to a practical calculation, an approximation has to be found for this expression. Even if nowadays, where there is a tendency towards more elaborate theories, a very popular one is the local density approximation (LDA) which yields good results in a large number of systems and which is still used in ab initio calculations (74; 84).

In this approximation, the exchange-correlation energy functional is chosen to have the same formal expression as the one of a uniform electron gas with the same density:

$$\mathcal{E}_{\mathrm{xc}}^{\mathrm{LDA}} = \int d^3r \, \varepsilon_{\mathrm{xc}}(n(\mathbf{r}))\, n(\mathbf{r}), \tag{2.24}$$

where the function $\varepsilon_{\mathrm{xc}}(n(\mathbf{r}))$ depends locally on the density at the position $\mathbf{r}$. This function has been calculated through a Monte Carlo simulation (85), providing the total energy of the ground state of a homogeneous interacting electron gas. This data, which was obtained for several densities, has been parametrized (86), yielding a function usable in Eq. (2.24).

Considering the way this approximation has been obtained, it is obvious that for a uniform system, it is exact. Furthermore, it is expected to be still valid for a slowly varying electronic density. In other cases, its behaviour is not well controlled. It is used anyhow, mainly because of its ability to reproduce exper-

imental ground state properties of many systems. Although there is no direct proof why it works correctly, it turns out that LDA can successfully deal with atoms, molecules, clusters, surfaces and interfaces. Even for dynamical processes like the phonon dispersion, it has been shown to yield good results (87; 88). However, in the course of time, many systems have been found that are incorrectly described by LDA. The most popular examples of this class are dielectric constants and related quantities, as well as weak bonds, in particular hydrogen bonds. In the field of metals, the ground state structure of crystalline iron is predicted to be paramagnetic fcc instead of ferromagnetic bcc (89).

Various corrections have been introduced in the course of the years to improve the local density approximation, but none of them has yet been generally accepted as being 'the best'. The class of gradient-corrected (GC) functionals can in many situations significantly increase the accuracy of DFT. These functionals assume that the exchange correlation energy does not only depend on the density, but also on its spatial derivative:

$$\mathcal{E}_{\mathrm{xc}}[n, \nabla n] \;=\; \int d^3r \; \varepsilon_{\mathrm{xc}}[n(\mathbf{r}), \nabla n(\mathbf{r})] \; n(\mathbf{r}) \tag{2.25}$$

Among the GC schemes two of the popular ones, also used in this work, are the Perdew-Burke-Ernzerhoff (PBE) (90) functional and the BLYP functional, which is constructed from the exchange functional of Becke (91) and the correlation functional of Lee, Yang, and Parr (92). For illustration, the the exchange-correlation function for the BLYP functional is given below:

$$
\begin{aligned}
\varepsilon_{\rm xc} &= \varepsilon_{\rm xc}[n(\mathbf{r}), \nabla n(\mathbf{r})] \\
&= -\left(C_X + \beta \frac{x[n]^2}{1 + 6\beta \sinh^{-1} x[n]}\right) n^{1/3} \\
&\quad -a \, \frac{1 + b\, n^{-5/3} \left[C_F\, n^{5/3} - 2\tfrac{1}{9} t_W[n] + \tfrac{1}{18}\nabla^2 n\right] \mathrm{e}^{-c\, n^{-1/3}}}{1 + d\, n^{-1/3}} \qquad (2.26) \\
x[n] &= \frac{|\nabla n|}{n^{4/3}} \qquad (2.27) \\
t_W[n] &= \frac{1}{8}\frac{|\nabla n|^2}{n} - \frac{1}{8}\nabla^2 n \qquad (2.28)
\end{aligned}
$$

where for simplicity, an implicit dependence $n \equiv n(\mathbf{r})$ is assumed. The parameters $C_X, C_F, \beta, a, b, c, d$ are chosen in such a way that to fit the known exchange-correlation energy of selected atoms in their ground state.

2.5 Pseudopotential approximation

The Kohn Sham equations, Eq. (2.11), can be solved expanding the KS orbitals in a complete set of known basis functions. Among the various existing possibilities, only the plane wave (PW) basis set shall be discussed in further detail. When describing a periodic system, they have many numerical advantages, besides their conceptual simplicity. PWs allow a simple integration of the Poisson equation for the calculation of the Hartree potential, Eq. (2.14), and for the calculation of the kinetic energy expression, Eq. (2.12).

Due to the large oscillations of the core orbitals in the neighborhood of the atoms, plane waves cannot be used directly in the Kohn Sham formalism, Eq. (2.20). These oscillations would require an enormous number of plane waves in order to achieve an acceptable accuracy. However, chemical reactions involve exclusively the valence electrons which are relatively far away from the nuclei.

In contrast to this, the core electrons remain almost unaffected by the chemical bonding situation. Thus, they can be approximated to be "frozen" in their core configurations, independent of the chemical environment of the atom. This approximation considerably simplifies the task of solving the Kohn Sham equations, by eliminating all the degrees of freedom related to the core orbitals.

A further simplification consisting of mapping the core electrons out of Eq. (2.20) is done by the introduction of pseudopotentials. In the Hamiltonian, the nuclear potential is replaced by a new one, whose lowest energies coincide with the energies of the valence electrons in all-electron calculations. In addition, this pseudopotential is required to reproduce the shape of the valence wavefunctions in regions sufficiently far from the nucleus. Close to the nucleus, the strong oscillations of the valence orbitals due to orthogonality requirements in the all-electron case are smoothed out.

In typical pseudopotentials, there is an attractive Coulomb term, whose charge is given by the atomic valence, as well as a short-ranged term, which is supposed to reproduce the effects of core-valence orthogonality, core-valence Coulomb interaction, exchange and correlation between core and valence. In practice, these requirements are only partially satisfied. Nevertheless, it turns out that pseudopotentials allow the description of the valence properties up to a very good accuracy with a reasonable number of plane waves.

Common pseudopotentials are mostly norm-conserving. This means that in addition to reproducing the all-electron valence wavefunctions outside a certain core radius, the charge of the pseudo-wavefunction inside this core region is required to be identical to the corresponding charge in all-electron calculations. Several expressions of such pseudopotentials have been proposed in (93; 94; 95; 96; 97).

In general, it turns out that the number of plane waves necessary to obtain

physically meaningful valence orbitals can be drastically reduced by means of pseudopotentials.

2.6 Plane wave representation

There are basically three possibilities to represent the electronic wavefunction in terms of basis functions:

- Localized basis sets have a direct physical meaning, derived from the atomic orbital picture. Often, radial Gaussians combined with spherical harmonics are used to this purpose. They are commonly used in quantum chemistry program packages, since they can be used in all-electron schemes to increase the overall accuracy.

- Plane waves are more suited for calculations of periodic solids, as they naturally have the desired periodicity. They have a striking conceptual simplicity, and the kinetic energy and Coulomb interaction expressions between them are straightforward to implement. In addition, plane waves are not attached to the ions, so that moving the latter during a simulation does not give rise to any Pulay forces (98). To obtain a physical picture of the electronic state, they have to be transferred to direct space or R-space. This can be done very efficiently by using the Fast Fourier Transformations technique (99).

- Mixed schemes try to combine the advantages of localized basis functions in the regions close to the nuclei with the computationally very efficient description by plane waves in the interstitial space (100).

In the ab initio code underlying this work, plane waves are used for the basis set. One of their drawbacks is that fast oscillations in R-space cannot be

represented easily. Nevertheless, adopting the pseudopotential approximation introduced above the plane wave description is sufficiently accurate and provides an efficient method to analyze extended systems, in particular under periodic boundary conditions.

The electronic orbitals in a periodic system can be written according to Bloch's theorem (76):

$$\psi_{n,\mathbf{k}}(\mathbf{r}) \quad = \quad \varphi_{n,\mathbf{k}}(\mathbf{r}) \ \exp[i\mathbf{k}\cdot\mathbf{r}], \tag{2.29}$$

with a wavevector $\mathbf{k}$, a band index n and a function $\varphi_{n,\mathbf{k}}(\mathbf{r})$ which is periodic in space, with the periodicity of the primitive cell:

$$\varphi_{n,\mathbf{k}}(\mathbf{r}+\mathbf{R}) \quad = \quad \varphi_{n,\mathbf{k}}(\mathbf{r}) \tag{2.30}$$

for any lattice vector $\mathbf{R}$. In the plane wave representation, this periodic function can therefore be expanded as:

$$\varphi_{n,\mathbf{k}}(\mathbf{r}) \quad = \quad \frac{1}{\sqrt{\Omega}} \sum_{\mathbf{G}} c_{n,\mathbf{k},\mathbf{G}} \ \exp[i\mathbf{G}\cdot\mathbf{r}], \tag{2.31}$$

where Ω is the volume of the primitive cell and $\mathbf{G}$ are the reciprocal space vectors. These vectors are characterized through

$$\frac{1}{2\pi} \, |\mathbf{G}\cdot\mathbf{R}| \quad \in \quad \mathbb{N} \tag{2.32}$$

with $\mathbb{N}$ representing the set of integer numbers and $\mathbf{R}$ being any lattice vector. Thus, Eq. (2.30) is automatically satisfied. In fact, Eq. (2.31) is a discrete complex Fourier series development of the wavefunction $\varphi_{n,\mathbf{k}}$. The coefficients can be

obtained by means of the inverse transformation:

$$c_{n,\mathbf{k},\mathbf{G}} = \frac{1}{\sqrt{\Omega}} \int_{\Omega} d^3r \; \varphi_{n,\mathbf{k}}(\mathbf{r}) \; \exp[-i\mathbf{G}\cdot\mathbf{r}]. \tag{2.33}$$

In practice, the wavefunction $\varphi_{n,\mathbf{k}}(\mathbf{r})$ is not known for all points $\mathbf{r}$ in space, but rather on a finite mesh. Thus, the integral in Eq. (2.33) must be transformed into a discrete sum.

In the reciprocal space representation, the kinetic energy of an orbital can be simply written as

$$\mathcal{T}_n = -\frac{1}{2} \langle \varphi_{n,\mathbf{k}} | \; \nabla^2 \; | \varphi_{n,\mathbf{k}} \rangle \tag{2.34}$$

$$= \frac{1}{2\Omega} \sum_{\mathbf{G}} |\mathbf{k}+\mathbf{G}|^2 \; |c_{n,\mathbf{k}}|^2. \tag{2.35}$$

The accuracy of a calculation is determined by the number of plane waves in the series (2.31). In practice, this is commonly controlled through a maximum value for the contribution to the kinetic energy expression, Eq. (2.35), called cut-off energy E_c. Only those vectors $\mathbf{G}$ are taken into account which satisfy

$$\frac{1}{2} |\mathbf{k}+\mathbf{G}|^2 \leq E_c. \tag{2.36}$$

For sampling the first Brillouin zone over all possible values of the $\mathbf{k}$-vector, one considers the electronic wave functions at fixed $\mathbf{k}$-points that are distributed at representative positions of the Brillouin zone. Thus, the wave functions of a region of $\mathbf{k}$-space are represented by the wave function of a single $\mathbf{k}$-point. In this way one can define a regular mesh of $\mathbf{k}$-points and replace the integral over the first Brillouin zone by a discrete sum over the chosen $\mathbf{k}$-point mesh. Several schemes to construct such $\mathbf{k}$-point meshes have been proposed in the literature (101; 102; 103). Within this approximation only the electronic states

at a finite number of **k**-points are needed to calculate the electronic density and hence all physical quantities of interest. The error induced by this approximation can be reduced systematically by increasing the density of the **k**-point mesh.

For insulators it turns out that usually only a small number of **k**-points is required to get good converged results. By increasing the size of the supercell, the volume of the Brillouin zone becomes smaller and smaller. Therefore, with the increase of a supercell's size fewer **k**-points are needed. For most insulators often only $\mathbf{k} = 0$ (Γ-point approximation) is used. For metallic systems, on the other hand, much denser **k**-point meshes are required in order to get an appropriate sampling.

2.7 Car-Parrinello molecular dynamics (CPMD)

The basic idea underlying most of ab-initio molecular dynamics (MD) methods is to compute the forces acting on the nuclei, which are treated as classical particles, from electronic structure calculations that are performed "on-the-fly" as the atoms and molecules move on their trajectories.

In Born-Oppenheimer MD the static electronic structure problem is straightforwardly solved, given in each molecular dynamics step the set of fixed nuclear positions at that instance of time. The instantaneous forces on the nuclei are obtained as gradients of the computed total electronic energy with respect to nuclear positions. After the nuclei have been moved according to these forces substituted into the classical Newtonian equations of motion, the new forces could then be obtained by re-solving the KS-equations 2.20 under the new external potential. The advantage of the scheme is a relatively big time step for the integration of molecular dynamic equations, since no electronic dynamics is involved in the time-depended equations of motion for the nuclei, i.e. they can be integrated on

the time scale given by nuclear motion. However, this means that the electronic density has to be fully optimized self-consistently for every timestep.

An alternative approach for ab-initio MD simulations which has turned out to be more efficient in many cases was introduced by Car and Parrinello in 1985 (104). This scheme has been used extensively since then for simulating real materials previously inaccessible for such studies. The forces acting on the classical nuclear degrees of freedom are calculated from the electronic ground state along the trajectory. This involves adiabatically evolving of the ground-state electronic wavefunction along with the nuclear motion by introducing fictitious classical dynamics on the electronic degrees of freedom, KS orbitals. The following extended Lagrangian describes this technique:

$$\begin{aligned}\hat{L}(\mathbf{R}_I, \dot{\mathbf{R}}_I, \varphi_i, \dot{\varphi}_i) &= \sum_I \frac{1}{2M_I}\dot{\mathbf{R}}_I^2 + \sum_i \frac{1}{2\mu_i}\langle\dot{\varphi}_i|\dot{\varphi}_i\rangle - E^{\mathrm{el}}(\mathbf{R}_I, n(\mathbf{r})) - \\ &\quad \sum_{i,j}\Lambda_{ij}(\langle\varphi_i|\varphi_j\rangle - \delta_{ij}). \qquad (2.37)\end{aligned}$$

Here, M_I are the masses of the nuclei and μ_i $(= \mu)$ are the fictitious masses or inertia parameters associated with the electronic degrees of freedom. $\mathbf{R}_I$ are the position vectors of the nuclei. The last term represents orthonormality requirements for the wavefunctions with associated Lagrangian multipliers Λ_{ij}.

The physical total energy of the system, which is a sum of E^{el} and the kinetic energy of nuclei, remains always close to the exact Born-Oppenheimer surface, with fluctuations of a magnitude comparable to the fictitious kinetic energy of electronic orbitals, the second term in 2.37. In the adiabatic limit, where electronic and nuclear degrees of freedom are decoupled, the Car-Parrinello approach yields accurate nuclear trajectories. Proper adiabaticity is ensured by the appropriate choice of the fictitious electron mass μ (105). While a small value

necessitates a short timestep for the integration of the equations of motions, too large of a value will increase the coupling of the nuclear and electronic subsystems. An optimal range for the fictitious electron mass turns out to be from 200 up to 900 a.u. depending on the system under consideration. Also the available computer resources play a role, since smaller μ leads to faster fictitious electronic dynamics and hence requires a smaller time step, which in turn means more MD steps for the same simulation time.

The Car-Parrinello forces deviate at most instants of time from the exact Born-Oppenheimer force. However, this does not disturb the physical time evolution due to the intrinsic averaging effect of small-amplitude high-frequency oscillations within a few molecular dynamics time steps, i.e. on the sub-femtosecond time scale which is irrelevant for nuclear dynamics.

2.8 Treating metals: DFT with fractional occupation numbers

In this section, an extension to conventional DFT is introduced, which allows density functional-based calculations of zero-gap systems like metals. The absence of a band gap means that the higher occupied and lower unoccupied orbitals are energetically very close, which introduces a number of complications with respect to the conventional DFT description in which occupied/empty states are clearly separated. First, the absence of a band gap leads to a partial occupation of states close to the Fermi level. This can be understood from a statistical mechanics point of view. At nonzero temperature, the electronic states just below Fermi level (ϵ_F) will have an average occupation somewhat lower than 2, while those above will not be completely empty. Secondly, the dispersion relation $\epsilon(\mathbf{k})$ is qualitatively

different from that of a system with a nonzero gap. For insulating crystals (as we discussed above in section 2.6) it is often sufficient to assume flat energy bands, which can be described correctly by a single crystal moment (also called **k**-vector or **k**-point), normally the Γ-point (**k**=0). For metallic systems, however, this approximation is not adequate, since a metal is characterized by a Fermi surface crossed by partially occupied bands. This metallic behavior requires the Brillouin zone to be sampled by a set of explicit points in the calculations.

The theoretical formalism for the treatment of metals is often based on the Mermin functional (106; 107), which can be seen as an extension of the ground-state DFT to finite electronic temperature. It can be understood as an approach to achieve fractional occupation numbers $f_{n,\mathbf{k}}$ of the bands according to the Fermi distribution function:

$$f_{n,\mathbf{k}} = \left(1 + \mathrm{e}^{\beta(\varepsilon_{n,\mathbf{k}} - \mu_c)}\right)^{-1}. \tag{2.38}$$

where β is $(k_B T)^{-1}$ and μ_c is the chemical potential of the electrons which is equal to the Fermi energy. For insulators, the chemical potential μ_c lies between two energy levels, and the occupation numbers $f_{n,\mathbf{k}}$ in eq. (2.38) are either 0 or 1. Metallic systems are characterized by the fact that the chemical potential is located inside a band, so that the Brillouin zone dispersion cannot be neglected. Then, the electronic potential is defined implicitly by the condition of charge conservation, i.e. by a fixed total number of electrons:

$$N = \sum_{n,\mathbf{k}} f_{n,\mathbf{k}}. \tag{2.39}$$

According to Mermin theory, the electronic free energy (a function of T and μ_c) is shown to be a functional of electronic density $n(\mathbf{r})$, analogous to the

Hohenberg-Kohn (HK) energy functional discussed in previous sections. Like the Hohenberg-Kohn idea, the Mermin theorem is also based on the assumption that the nuclei can be considered as being instantaneously fixed, providing the external potential in which the electrons move. However, unlike the HK theory, in which the electronic density changes adiabatically (keeping close to the ground state surface and therefore having zero entropy), the Mermin idea instead keeps the electron temperature fixed. This approach assumes that the thermal equilibration of the electrons is much faster than the time scale of the atomic motion, so that the electrons always remain very close to thermal equilibrium. This turns out to be a good approximation for metals.

While the standard Kohn-Sham equations of DFT essentially remain unmodified (106; 108; 109), it is necessary to rewrite the equation for the electronic density, in order to take into account the fractional occupation numbers of the electronic orbitals and the effect of $\mathbf{k}$-points other than $\mathbf{k} = 0$. This eventually leads to:

$$n(\mathbf{r}) \quad = \quad \sum_{i,\mathbf{k}} f_{i,\mathbf{k}}(\beta) |\varphi_{i,\mathbf{k}}(\mathbf{r})|^2 \tag{2.40}$$

where the fractional occupation numbers $f_{i,\mathbf{k}}$ are obtained from the Fermi-Dirac distribution at electronic temperature T in terms of Kohn-Sham eigenvalues $\epsilon_{i,\mathbf{k}}$. Note that the summation over the bands in eq. (2.40) has to include a certain number of bands which would be unoccupied by $T = 0$ (virtual states). Another difficulty in the actual self-consistent calculation of the orbitals $\varphi_{i,\mathbf{k}}$ stems from the dependence of the electronic density $n(\mathbf{r})$ on the Kohn-Sham energies $\epsilon_{i,\mathbf{k}}$.

Due to this additional complexity, the numerical solution of the final equations is computationally significantly more expensive than comparable calculations for insulators. However, they have become feasible for realistic systems,

e.g. for surfaces consisting of unit cells of up to four layers of 5×5 atoms, using a Monkhorst-Pack mesh (102) of 4×4×1 **k**-points for sampling the first Brillouin zone.

Chapter 3

Spectroscopic properties from density functional theory

3.1 General

Knowledge of the electronic density (or electronic orbitals) is only one of the goals of computational chemistry. In itself, the electronic density has only a limited value, but many important physical and chemical quantities can be derived from it. The most prominent ones are the equilibrium geometries and corresponding molecular energies, as well as atomic forces and dynamical conformations at finite temperatures. Another very important class of quantities are response properties, like IR-, UV-, Raman and nuclear magnetic resonance (NMR) frequencies, which can provide direct comparison of the computed spectroscopic parameters with measured spectra. They can also be used for an indirect validation of computational results obtained for properties which are not easily accessible from experiment, like structural properties of low-ordered systems or the character of an H-bond network. Being included in the same computational framework, the calculation of spectroscopic parameters is a tool to enable the dialogue between

theory and experiment.

In the following sections, the theoretical description of two spectroscopic properties which are of particular interest in this work is outlined. The atomic harmonic frequencies and NMR chemical shifts are considered within the formalism of density functional theory under periodic boundary conditions.

3.2 IR frequencies

The adsorption of infrared radiation by a molecule can be observed when the molecule changes its dipole moment during its vibrational or rotational motion. These regular fluctuations in dipole moment interact with the external electrical field of the radiation. If the frequency of the infrared radiation matches a natural vibrational frequency that induces a change in the molecular electric dipole, a transfer of energy takes place which results in a change in the amplitude of the molecular vibration and as a consequence in the adsorption of the radiation. Similarly, the rotation of asymmetric molecules around their centers of mass results in a periodic dipole fluctuation which can interact with radiation. In a quantum mechanical description, this interaction would correspond to the transition between the ground state and excited vibrational or rotational energy levels. The theoretical framework for calculations of vibrational IR spectra will be outlined in the next sections.

3.2.1 Normal modes

The energy of a molecule can be presented as a sum of electronic, vibrational, rotational and translational contributions. As the first approximation, all these contributions can be considered separately. Electronic energy transitions normally give rise to absorption or emission in the ultraviolet or visible regions of

the electromagnetic spectrum. Pure rotation would appear in adsorption lines in the microwave region or the far infrared. Molecular vibrations cover most of the infrared region of the spectrum.

In the classical treatment of nuclei, where they are considered as point particles with a mass, a molecule with N atoms has $3N$ degrees of freedom. After substracting the degrees of freedom which correspond to translational and rotational motion of the molecules, $3N-6$ internal degrees of freedom are left for non-linear molecules (or $3N-5$ for linear ones). It can be shown (5) that these $3N-6$ internal degrees of freedom of non-linear molecules correspond to $3N-6$ independent normal modes of vibration. These normal modes are characterized by the fact that in each of these modes, all the atoms in the molecule vibrate in a concerted way with the same frequency and pass simultaneously through their equilibrium positions. Hence, each normal mode can be described by its amplitude, the scalar normal coordinate Q_i, which varies periodically. In addition to Q_i, a 3N-dimensional vector $\mathbf{u}_i$ describes the orientation of the displacement of each atom in such a mode. If the vibrations are harmonic or their amplitudes remain small, normal modes of vibration can be excited independently of each other, so that normal coordinates are also independent in the sense that each of them makes individual independent contributions to the total vibration potential and kinetic energies. Therefore the contributions of normal coordinates can be treated separately. Thus, the complex vibrational motion of a molecule can be written as a superposition of normal modes of vibration, whose frequencies (also called natural vibrational frequencies) define the IR absorption spectra for the molecule.

3.2.2 Change in molecular dipole moment

The dipole moment of a system of two point charges is determined by the magnitude of the charge difference and the distance between the two centers of charge. In a complex molecule, the positive charge represents the total charge of the nuclei concentrated at the center of gravity of the nuclei, and the negative one corresponds to the electronic charge located in the center of gravity of electrons.

In a spectrometer, a molecule is irradiated with a wide band of infrared frequencies (e.g. 200-4000 cm^{-1} for the middle-infrared region). Since the wavelength of the radiation is much greater than the size of most molecules, the electric field of the photon in the vicinity of a molecule can be considered uniform over the whole molecule. This electric field exerts forces on the molecular charges which act in opposite directions for the opposite charges. Therefore the oscillating field of the photon will exert forces tending to induce the dipole moment of the molecule to oscillate at the photon frequency. At certain frequencies when the external radiation and the nuclei oscillate simultaneously the forced dipole fluctuation will tend to activate the nuclear vibration. The more the dipole moment changes during a vibration, the more easily the photon's electric field can activate this mode and vice versa. This leads to the following selection rule: in order to adsorb infrared radiation, a molecular vibration must cause a change in the dipole moment of the molecule. It can be shown that the intensity of an infrared adsorption band is proportional to the square of the changes in the dipole moment caused by the normal mode giving rise to this band.

According to the time correlation function formalism of linear response theory (110), the infrared spectrum can be computed from the dipole moment autocorrelation functions. In the harmonic approximation, when the total dipole moment can be written as a linear combination of contributions from effective normal

modes of the system, the quantum correlation functions can be replaced (111) by classical ones. This replacement allows the calculation of condensed-phase systems with many degrees of freedom on realistic time scales. Thus, vibrational frequencies and intensities can be computed by sampling dipole moment auto-correlation functions along molecular dynamics trajectories.

3.2.3 Dynamical matrix

In the harmonic approximation, there is also an alternative approach for a calculation of the infrared adsorption spectra which does not require molecular dynamics simulations. Harmonic frequencies of normal vibrational modes can be computed by the diagonalization of the dynamical matrix of a system. The concept of the dynamical matrix can be understood if we consider a classical one-dimensional oscillator. In this system, a frequency of vibrational motion is determined by the steepness of the harmonic potential:

$$V^{HO}(x) = \frac{kx^2}{2} = \frac{m\omega^2 x^2}{2} \tag{3.1}$$

An analogous expression can be also obtained for a system with many intrinsic nuclear degrees of freedom. Around the equilibrium geometry, the total energy of the system can be expanded with respect to the displacements of nuclear coordinates from equilibrium positions: $\delta\mathbf{R}_\alpha = \mathbf{R}_\alpha - \mathbf{R}_\alpha{}^{eq}$. The expansion is written as

$$E(\mathbf{R}) = E(\mathbf{R}^{eq}) + \sum_\alpha \left.\frac{\partial E}{\partial \mathbf{R}_\alpha}\right|_{\mathbf{R}^{eq}} \delta\mathbf{R}_\alpha + \frac{1}{2}\sum_{\alpha\beta} \left.\frac{\partial^2 E}{\partial \mathbf{R}_\alpha \partial \mathbf{R}_\beta}\right|_{\mathbf{R}^{eq}} \delta\mathbf{R}_\alpha \delta\mathbf{R}_\beta + o(\mathbf{3})2)$$

where the Greek letters are the nuclear indices, $\alpha = 1, N_I$ (N_I is the number of atoms).

The first term in 3.2 is the equilibrium energy. The second one represents the forces acting on nuclei at the equilibrium geometry and therefore must be equal to zero, because a local minima of electronic potential energy surface is characterized by the forces $\mathbf{F}_\alpha = -\frac{\partial E}{\partial \mathbf{R}_\alpha}\Big|_{\mathbf{R}_\alpha^{eq}} = 0$. In the harmonic approximation, all terms of the third and higher orders are neglected in the energy expansion 3.2, such that only the quadratic term remains representing the harmonic oscillations of the nuclei around the equilibrium position given by the electronic potential.

The dynamical matrix of the system of particles is defined in Cartesian coordinates by:

$$D_{\alpha i \beta j} = (M_\alpha M_\beta)^{-\frac{1}{2}} \left(\frac{\partial^2 E_{ion}}{\partial R_{\alpha i} \partial R_{\beta j}} + \frac{\partial^2 E_{KS}}{\partial R_{\alpha i} \partial R_{\beta j}}\right)\Big|_{\mathbf{R}_\alpha^{eq}, \mathbf{R}_\beta^{eq}} \tag{3.3}$$

where again the ions are indicated with Greek indices and the Cartesian coordinates with Latin ones. This matrix has $(3N_I)$x$(3N_I)$ dimensionality and it is symmetric by definition, hence its eigenvalues are real. In terms of its eigenvectors $u_{\alpha i}^{(a)}$ and eigenvalues $\lambda^{(a)}$, the dynamical matrix can be written as:

$$D_{\alpha i \beta j} = \sum_a u_{\alpha i}^{(a)} \lambda^{(a)} u_{\beta j}^{(a)T} \tag{3.4}$$

where $a = 1, 3N_I$. Then, the second term of the energy expression 3.2 can be transformed the following way:

$$E^{(2)}(\mathbf{R}) = \frac{1}{2} \sum_{\alpha i, \beta j, a} (M_\alpha M_\beta)^{\frac{1}{2}} u_{\alpha i}^{(a)} \lambda^{(a)} u_{\beta j}^{(a)T} \delta R_{\alpha i} \delta R_{\beta j} \tag{3.5}$$

At this stage, a new set of 3N coordinates $Q^{(a)}$ is introduced:

$$Q^{(a)} = \sum_{\alpha i} (M_\alpha)^{\frac{1}{2}} u_{\alpha i}^{(a)} \delta R_{\alpha i} \tag{3.6}$$

which allow us to rewrite the complex energy expression 3.2 as a superposition of simple individual contributions:

$$\delta E^{(2)}(\mathbf{R}) \quad = \quad \frac{1}{2}\sum_{a} \lambda^{(a)} {Q^{(a)}}^2 \tag{3.7}$$

The constant term $E(\mathbf{R}^{eq})$ is omitted in 3.7 , since it does not contribute to vibrational motion.

The new expression 3.7 has the form of a set of $3N_I$ superimposed oscillators of the form given in 3.1. Based on this analogy, $Q^{(a)}$ are defined as the normal coordinates for $3N_I$ independent normal modes, whose frequencies $\omega^{(a)}$ are given by the eigenvalues of dynamical matrix: $\lambda^{(a)} = {\omega^{(a)}}^2$. From these $3N_I$ frequencies, six ones corresponding to translational and rotational degrees of freedom are equal to zero, while the remaining $3N_I - 6$ are the harmonic frequencies of normal modes of vibration.

For a calculation of the dynamical matrix, the contribution from ionic repulsion potential E_{ion} in 3.8 can be obtained straightforwardly. The second term in 3.8 which comes from the electron-nuclei interactions is computed either by perturbation theory methods (112) or with a finite differences technique. According the latter, six small displacements of each nucleus from its equilibrium position ${\mathbf{R}_\alpha}^{eq}$ in both directions of three coordinate axis are considered. For each of $6N_I$ new geometries the electronic Kohn-Sham energy and forces acting on the nuclei are calculated. Knowing the forces, which are the first derivatives of the total energy with respect to the nuclear positions, the second derivatives are then computed as

$$\frac{\partial^2 E_{KS}}{\partial R_{\alpha i} \partial R_{\beta j}} \quad = \quad \frac{\Delta F_{\alpha i}}{\Delta R_{\beta j}} \tag{3.8}$$

where $\Delta R_{\alpha i} = \Delta R$ is the finite displacement parameter. This parameter has to be chosen in such a way that the nuclear displacement of this procedure will be much smaller than the interatomic distances.

Thus, by computing and diagonalization of dynamical matrix of the system the harmonic frequencies of normal vibrational modes can be found, which in turn correspond experimental infrared adsorption spectra.

3.3 NMR chemical shifts

The NMR chemical shift is derived from the Larmor frequency of the nuclear spin of an atom, which describes the precession of the spin when the system is placed in a magnetic field. Since the electrons also react to the external field, the total magnetic field responsible for this precession is the superposition of the external field and the field induced by the electronic response. The latter is heterogeneous field created by local ring currents of electronic orbitals. The interaction of electron spins with external magnetic field is not considered here, since for the closed-shell system the total electron spin is equal to zero. Hence, non-equivalent atoms feel different total magnetic fields, and their nuclear spins therefore have different energy levels. The nuclear shielding tensor is defined as a proportionality matrix between the induced field at the position of a nucleus and the externally applied field:

$$\sigma(\mathbf{R}) \;=\; \frac{\partial \mathbf{B}^{\mathrm{ind}}(\mathbf{R})}{\partial \mathbf{B}^{\mathrm{ext}}}. \tag{3.9}$$

In order to obtain this tensor numerically, the impact of the magnetic field on the electronic orbitals has to be calculated. It acts through a vector potential $\mathbf{A}(\mathbf{r})$ in the Hamiltonian of the electronic system, whose effect on the orbitals is usu-

ally calculated by perturbation theory. The outline of the theoretical framework described in detail in (112; 113) will be presented in the next sections.

3.3.1 Magnetic perturbation theory

According to the Maxwell's equation, a magnetic field $\mathbf{B}$ is divergence-free and therefore can be represented by a vector potential $\mathbf{A}$ which has to satisfy the relation

$$\mathbf{B} = \nabla \times \mathbf{A}(\mathbf{r}) \tag{3.10}$$

The vector potential is an auxiliary quantity, it has no direct physical meaning. For a given magnetic field, a whole class of vector potentials exist which fulfill the constituting equation 3.10.

It contains a degree of freedom in form of an arbitrary scalar function $\Phi_g(\mathbf{r})$ whose gradient may be added to $\mathbf{A}(\mathbf{r})$ without affecting the resulting magnetic field:

$$\mathbf{A}(\mathbf{r}) \mapsto \mathbf{A}'(\mathbf{r}) = \mathbf{A}(\mathbf{r}) + \nabla\Phi_g(\mathbf{r}) \tag{3.11}$$

$$\mathbf{B}' = \nabla \times (\mathbf{A}(\mathbf{r}) + \nabla\Phi_g(\mathbf{r})) = \nabla \times \mathbf{A}(\mathbf{r}) = \mathbf{B}. \tag{3.12}$$

$\Phi_g(\mathbf{r})$ is called the gauge function, and its choice should not affect any physical results (gauge invariance). A typical choice for $\mathbf{A}$ in the case of a desired homogeneous magnetic field $\mathbf{B}$ is

$$\mathbf{A}(\mathbf{r}) = -\frac{1}{2}\,(\mathbf{r} - \mathbf{R}_g) \times \mathbf{B} \tag{3.13}$$

where a particular class of gauge functions was taken. It obviously satisfies

eq. (3.10). A cyclic variable $\mathbf{R}_g$ is called the gauge origin of the vector potential $\mathbf{A}$ and describes a translation of the origin of the coordinate system by $\mathbf{R}_g$. This gauge origin does not change the physics of the system, but furthermore it will be shown that a careful choice of the gauge function is essential for ensuring good numerical accuracy.

The incorporation of the magnetic field into the system's Hamiltonian is done by replacing the standard momentum operator by its generalized expression in the presence of a magnetic field (114):

$$\hat{\mathbf{p}} \mapsto \hat{\boldsymbol{\pi}} = \hat{\mathbf{p}} - e\mathbf{A}(\hat{\mathbf{r}}) \tag{3.14}$$

This generalized momentum replaces the standard momentum operator $\hat{\mathbf{p}}$ in the Hamiltonian. Developing the latter in powers of the magnetic field (i.e. in powers of $\mathbf{A}$), this yields a linear and a quadratic term:

$$\hat{H}^{(1)} = -\frac{e}{m}\hat{\mathbf{p}} \cdot \mathbf{A}(\hat{\mathbf{r}}) \tag{3.15}$$

$$\hat{H}^{(2)} = -\frac{e^2}{2m}\mathbf{A}(\hat{\mathbf{r}}) \cdot \mathbf{A}(\hat{\mathbf{r}}). \tag{3.16}$$

with the momentum operator $\hat{\mathbf{p}}$, and the charge e and mass m of the electron. These modifications of the field-free Hamiltonian are treated within perturbation theory and represent the first and second order perturbation Hamiltonians.

Density functional perturbation theory (DFPT), also known as the coupled perturbed Kohn-Sham (KS) method (112) provides the electronic linear response $|\varphi_i^{(1)}\rangle$ to the magnetic field. The total wavefunction is then obtained as $|\varphi_i\rangle = |\varphi_i^{(0)}\rangle + |\varphi_i^{(1)}\rangle$.

3.3.2 Electronic current density

The electronic current density at a position $\mathbf{r}'$ is defined as the expectation value of the current operator:

$$\hat{\mathbf{j}}_{\mathbf{r}'} = \frac{e}{2m}\left[\hat{\boldsymbol{\pi}}|\mathbf{r}'\rangle\langle\mathbf{r}'| + |\mathbf{r}'\rangle\langle\mathbf{r}'|\hat{\boldsymbol{\pi}}\right]. \tag{3.17}$$

Using first order perturbation theory, one can show (113) that the first non-vanishing term in the expansion of the expectation value for the induced electronic current density is given by:

$$\begin{aligned}\mathbf{j}^{(1)}(\mathbf{r}') = {} & \frac{e}{2m}\sum_j \langle\varphi_j^{(0)}|\left(\hat{\mathbf{p}}|\mathbf{r}'\rangle\langle\mathbf{r}'| + |\mathbf{r}'\rangle\langle\mathbf{r}'|\hat{\mathbf{p}}\right)|\varphi_j^{(1)}\rangle + \text{c.c.} \\ & -\frac{e^2}{m}\sum_j \mathbf{A}(\mathbf{r}')\,\langle\varphi_j^{(0)}|\mathbf{r}'\rangle\langle\mathbf{r}'|\varphi_j^{(0)}\rangle\end{aligned} \tag{3.18}$$

The two terms of the expression 3.18 are called para– and diamagnetic current densities, respectively. Both contributions individually depend on the gauge, whereas the total current $\mathbf{j} = \mathbf{j}^{(1)}(\mathbf{r}')$ is gauge-independent. However, the two contributions are large numbers and have opposite signs. For the choice of the vector potential given in eq. 3.13, $\mathbf{A}(\mathbf{r})$ is linear in the gauge origin $\mathbf{R}_\text{g}$. Therefore, the diamagnetic current also grows linearly in $\mathbf{R}_\text{g}$, and paramagnetic term must compensate this in order to fulfill the invariance of the total current. Thus, for large distances $|\mathbf{r} - \mathbf{R}_\text{g}|$, the current density $\mathbf{j}$ results from the cancellation of two large terms, making the actual calculation rather challenging. In a computer simulation using a finite basis set, the gauge invariance of $\mathbf{R}_\text{g}$ is no longer numerically verified.

To circumvent the problem, the so-called "$\mathbf{R}_\text{g} = \mathbf{r}$"–variant of the continuous set of gauge transformations (CSGT method (115)) is used (113) . In this ap-

proach, for each point $\mathbf{r}'$ in space at which the current density is calculated, the gauge origin $\mathbf{R}_g$ is set to $\mathbf{r}'$. Thus, the last term of eq. 3.18 vanishes analytically and the cancellations of large numbers no longer occurs.

However, the formalism described above still cannot be straightforwardly applied to extended systems. The position operator in equation 3.18 is nonperiodic and in systems considered under periodic boundary conditions it is ill-defined. One possibility to overcome the problem is to restart at eq. 3.13 and to assume that the external magnetic field is modulated with a cosine along its direction (116): $\mathbf{B}(\mathbf{r}) = \mathbf{B}_0 \cos \mathbf{q} \cdot \mathbf{r}$, with a finite wavevector $\mathbf{q}$. This results in a periodic vector potential which is then well-defined under periodic boundary conditions (117; 118). The physically relevant case $\mathbf{B}(\mathbf{r}) = \mathbf{B}_0$ is obtained by extrapolating numerically the results for $q \to 0$. However, this is computationally relatively demanding since the same calculation has to be done several times, for several values of $\mathbf{q}$. In addition, this method always requires many k-points apart from Γ to be included, because $|\mathbf{q}|^{-1}$ typically far exceeds the unit cell dimensions.

An alternative proposed and applied by Sebastiani et al. (113; 119) is the transformation of the Bloch wavefunctions into maximally localized Wannier orbitals (120) for which a suitably modified saw-tooth position operator can be defined. It was shown that in an insulator the resulting localized wavefunctions decay exponentially (121). Thus, the unit cell for the system can be chosen such that the lattice parameter is larger than the decay length for these Wannier orbitals and the orbitals are significantly different from zero only within a limited region of the cell. Then, virtual cells for position operator are assigned to the corresponding wavefunctions. The virtual cell walls are located in that region of space where the orbital density is close to zero over a certain range, as shown in figure 3.1. At the point where the switching between images occurs, a smoothing

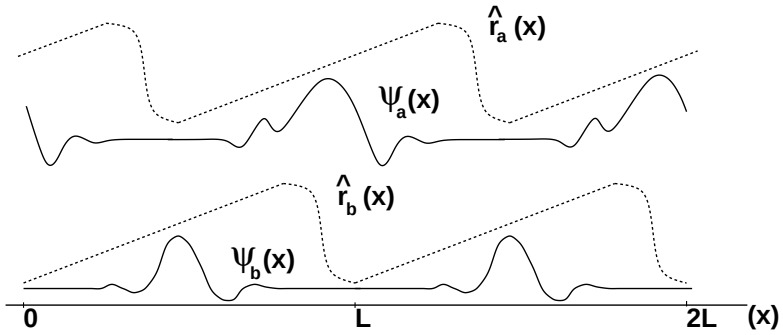

Figure 3.1: Individual position operators of two different localized Wannier orbitals

function is applied in order to avoid sharp jumps. Since this unphysical jump takes place in the region where the wavefunctions have zero amplitude, it has no effect on any calculated quantities. Thus, the new periodic position operator is defined which is identical in every virtual cell and all its replica, and therefore matches the periodically boundary conditions.

3.3.3 Induced field, susceptibility and shielding

Once the induced electronic current density 3.18 is properly defined and can be treated numerically, the induced inhomogeneous magnetic field can be obtained by the Biot-Savart law:

$$\mathbf{B}^{\mathrm{ind}}(\mathbf{r}) \;=\; \frac{\mu_0}{4\pi}\int d^3r'\,\frac{\mathbf{r}'-\mathbf{r}}{|\mathbf{r}'-\mathbf{r}|^3}\times\mathbf{j}(\mathbf{r}'), \tag{3.19}$$

where μ_0 is the permeability of the vacuum. The integral in eq. (3.19) is well-known as the solution of the Poisson equation for the electrostatic field. Since the system is treated under periodic boundary conditions, the current density $\mathbf{j}(\mathbf{r})$ is periodic and can be represented in reciprocal space. The difficulty lies in the point that $\frac{1}{|\mathbf{r}'-\mathbf{r}|}$ is not periodic. Under periodic boundary conditions, the convergence of eq. (3.19) in reciprocal space is not assured generally; but with

the exception of the $\mathbf{G} = 0$ component. In this case, its Fourier transform can be computed in a straightforward way (122) and reads:

$$\mathbf{B}^{\mathrm{ind}}(\mathbf{G} \neq 0) \quad = \quad \mu_0 \, i \, \frac{\mathbf{G}}{|\mathbf{G}|^2} \, \times \, \mathbf{j}(\mathbf{G}). \tag{3.20}$$

where the $\mathbf{j}(\mathbf{G})$ denote the vectors of Fourier coefficients, defined in analogy to equation 2.33. The $\mathbf{G} = 0$ component of the field depends on the bulk magnetic susceptibility tensor, χ, and the shape of the sample. In general, it is expressed as:

$$\mathbf{B}_0^{\mathrm{ind}} \quad = \quad \kappa \, \chi \, \mathbf{B}^{\mathrm{ext}} \tag{3.21}$$

with the macroscopic bulk susceptibility χ and a prefactor which describes the dependence on the macroscopic geometry of the system.

The bulk susceptibility χ can be expressed (113) as a function of the orbital electronic current:

$$\chi \quad = \quad \frac{\mu_0}{2\Omega} \, \frac{\partial}{\partial \mathbf{B}^{\mathrm{ext}}} \int_{\Omega} d^3r \; \mathbf{r} \times \mathbf{j}(\mathbf{r}), \tag{3.22}$$

where the integral is done over one unit cell of volume Ω. In the case of a spherical system, κ is given by $\kappa = 2/3$ (113).

As we already discussed above, the chemical shift tensor, one of the main physical observables calculated in this work, is defined as the proportionality factor between the induced and the externally applied magnetic field at the positions of the nuclei:

$$\sigma(\mathbf{R}) \quad = \quad \frac{\partial \mathbf{B}^{\mathrm{ind}}(\mathbf{R})}{\partial \mathbf{B}^{\mathrm{ext}}}. \tag{3.23}$$

Hence, it can be straightforwardly calculated since the induced magnetic field is known.

In experiment, this shielding tensor is measured and quoted relative to a reference material, e.g. for hydrogen commonly tetramethylsilane (TMS). This yields the chemical shift tensor:

$$\delta(\mathbf{R}) \quad = \quad \sigma^{ref}(\mathbf{R}) - \sigma(\mathbf{R}) \tag{3.24}$$

The trace of this tensor is the central quantity measured in NMR spectroscopy.

Chapter 4

Initial steps of water adsorption on metallic surfaces: water oligomers on nickel

4.1 Motivation

Transition metal surfaces play a crucial role for many reactions in heterogeneous catalysis. Their catalytic functionality can be affected by a variety of factors, such as the morphology of the surface, defects, or poisoning. The most prominent example of poisoning is the adsorption of CO on platinum and similar surfaces (123; 124; 125). Another important issue is the co-adsorption of several species, which may have an important influence on dissociation processes (125; 126).

More generally, the adsorption of small molecules from the environment can significantly modify the catalytic efficiency of such metal surfaces. One particular case in this scenario is the adsorption of water. Therefore, the interaction of water with metal surfaces is of tremendous importance for industrial applications and

of very high relevance in surface chemistry. The fundamental mechanisms of the initial phases of this adsorption process has been the subject of a variety of recent experimental and theoretical investigations (31; 32; 127; 128; 129; 130) and is still a matter of intense controversy (131; 132; 133).

There is evidence that the water molecules can approach the surfaces in both hydrogen-up and hydrogen-down orientations. Depending on the metal species, a water monolayer can be formed through simultaneous binding of all water molecules to the surface, e.g. in the case of Pt(111), or alternatively as a partially dissociated layer, which is the case for Ru(0001) (32; 127).

The deposition of isolated water molecules has already been studied on several flat metallic surfaces, such as Ru(0001), Rh(111), Pd(111), Pt(111), Cu(111) and Ag(111) (134; 135; 136). An interesting mechanism for dimer diffusion through a combined proton tunneling and molecular rotation scheme has been proposed recently (137).

In most of these studies the presence of a full highly symmetric water monolayer is assumed. However, the *process* of wetting, which is initiated by the adsorption of a single water molecule or small water clusters, is still poorly understood. From the view of an adsorbing water molecule, the surface has to compete thermodynamically with larger water clusters or simply the gas phase. Both phases provide a significantly larger entropic contribution to the free energy, which has to be compensated by a corresponding energy difference. Therefore, the theoretical investigation of the structural and energetic properties of the initial adsorption process on realistically modeled surfaces deserves particular attention. Also the crucial role of surface defects on the adsorption processes is not always considered, especially in theoretical studies.

In this work, the aim is to focus on a realistic description of the initial steps of water adsorption, going beyond a single adsorbed molecule but without imposing

a complete coverage of the surface. For this purpose, the adsorption of a sequence of water oligomers on nickel is studied. Starting from an isolated molecule, a water dimer as well as a trimer are investigated, paying particular attention to the influence of hydrogen bonding on the adsorption energy and the structure of the adsorbate.

Inspired by previous studies (138; 139; 140; 141), not only at a perfect surface is considered, but also the simplest possible defect, a one-dimensional step. This is realized by using a surface in the (221) direction. The adsorption-enhancing effect of such steps has also been shown recently by experimental studies of germanium deposition on silicon surfaces (142).

A simple step defect on the nickel surface has the potential to enhance the adsorption energy of the initial water molecule by as much as 40 % (33). Also the incremental adsorption energy of an additional second water molecule is higher than at a defect-free adsorption site. In principle, these adsorption energies can be determined experimentally, but spectroscopic parameters are often easier to obtain. First-principles calculations of experimentally accessible spectra are very scarce, also because of the relatively high computational cost involved in realistic and accurate calculations.

In this work, ab-initio calculations of IR peaks as a function of adsorption sites and cluster sizes enable for the first time a direct comparison of measurements and calculations. The initial steps of water adsorption on different nickel surfaces are characterized by means of their harmonic frequencies. It will be shown how the vibrational modes and frequencies of water clusters (monomer, dimer and trimer) are modified upon adsorption. Furthermore, the complex water-nickel vibrational modes involving the nickel-oxygen bond will be described. As recent theoretical and experimental studies have shown, both the antisymmetric and the symmetric stretch vibrations can promote catalytic processes such as the chemisorption of

methane on nickel (143). Finally, it will be illustrated how the eigenmodes of the adsorbates could be used as a first step in modeling the dissociation of water which in turn may eventually lead to corrosion and surface passivation (144).

4.2 Computational details

The flat and stepped surfaces are modeled within density functional theory (DFT) under periodic boundary conditions as two-dimensional slabs with a finite thickness. The hexagonal supercells have been chosen containing 3 (111)-layers for the (221) step and 4 (111)-layers for the flat surface, with 16 nickel atoms for the water monomer on the flat surface, 36 for the water dimer and trimer on the flat, and 22 for the monomer and dimer on the step surface. The step-defect has been modeled by the (221) surface because it is the smallest possible configuration. This setup ensures that the water oligomers are always separated from their lateral periodic images by at least 5 $\mathring{A}$ for the step and 7,5 $\mathring{A}$ for the flat surfaces. In the third dimension, the slabs are separated by about 10 $\mathring{A}$ of vacuum.

For all surfaces, a plane-wave cutoff of 60Ry has been used, together with Troullier-Martins pseudopotentials (95) in the Kleinman-Bylander scheme, as well as a special pseudopotential by Lee (145) for nickel. The plane wave cutoff convergence has been checked on a water dimer geometry optimization at 60Ry and at 100Ry. The resulting hydrogen bond energies are 0.2400eV and 0.2398eV, which represents a difference that lies well below the numerical noise of the method. All calculations have been done with the PBE exchange-correlation functional (146). The electronic structure has been computed using the implementation of the Mermin functional (106; 108) in the CPMD code. A $4\times4\times1$ and a $3\times3\times1$ k-point mesh within the Monkhorst-Pack scheme (102) have been used to sample the Brillouin zone for the step and flat surfaces, respectively. Using

this computational setup, the recently published results of Michaelides et al (34) could be reproduced for the adsorption of a complete water monolayer within a numerical tolerance of 50 meV.

Geometry optimization for the adsorption energy calculations has been done until the norm of the atomic forces dropped below a threshold of $2 \cdot 10^{-3}$ Hartree/bohr. A test calculation with a convergence criterion of $3 \cdot 10^{-4}$ Hartree/bohr taken for the geometry optimization has revealed that the resulting change in the total energy was less than 0.05 eV. An estimator for the artificial energy lowering due to the periodicity of our simulation cell has also been computed. The periodicity causes the water molecules to interact electrostatically with their own images, and this interaction is therefore an artifact of the modelling approach. An isolated water molecule in the same computational box as for adsorbed monomer has a total energy which is about 0.01 eV lower than that in a box of twice the lattice constant.

All adsorption energies have been computed (33) with respect to a single isolated water molecules in the same simulation box (thus eliminating the dipole interaction error):

$$\Delta E \quad = \quad E\left[\mathrm{Ni} \cdot (\mathrm{H_2O})_n\right] - E\left[\mathrm{Ni}\right] - n\, E\left[\mathrm{H_2O}\right]. \tag{4.1}$$

This definition also allows us to obtain directly the incremental adsorption energies for an additional water molecule, which would be more involved when considering the adsorption energy of the water cluster as an entity (i.e. when taking $E\left[(\mathrm{H_2O})_n\right]$ instead of $n\, E\left[\mathrm{H_2O}\right]$).

Furthermore, electron density difference maps have been computed for selected energetically favorable configurations (33) , showing the rearrangement of the density between the surface-adsorbed $\mathrm{Ni}\cdot(\mathrm{H_2O})_n$ complex and the fragments.

For visualizing these maps, color-coded slices were plotted with the projected electron density differences $\delta\rho$ defined as

$$\delta\rho(x,z) \;=\; \int dy \;\Big(\rho^{\mathrm{Ni}\cdot(\mathrm{H_2O})_n}(\mathbf{r}) - \rho^{\mathrm{Ni}}(\mathbf{r}) - \rho^{(\mathrm{H_2O})_n}(\mathbf{r})\Big). \tag{4.2}$$

Here, in contrast to the definition of the energy difference, the density plots compare the adsorbed system with the water oligomer cluster and the isolated surface. In this way, the density displacements due to the *formation* of hydrogen bonds between the water molecules are not plotted, while the *modifications* of these densities due to the adsorption become visible. The density difference maps were computed in orthorhombic cells obtained by doubling the original hexagonal unit cells and by cutting out a suitable orthorhombic subpart of at least the size of the original setup. This was necessary for a proper visualization of the densities with the program Molekel (147).

For calculations of the IR frequencies, geometry optimizations were done on a significantly tighter level than for adsorption energies, such that the norm of the atomic forces dropped below a threshold of $4\cdot 10^{-4}$ atomic units. Although this further optimization changes the total energy only by negligible amounts, the accuracy of the calculated vibrational frequencies is very sensitive to the convergence norm of the atomic forces.

The frequency calculations were done using a finite displacement scheme (as described in detail in section 3.2) with the symmetric displacement step of 0.025 $\mathring{A}$. According test calculations, the further increasing of the displacement step would shift the system too far from local equilibrium and therefore produce the incorrect frequencies. The dynamical matrix was computed for all water atoms and the nickel atom which is bonded to the first adsorbed water. The coordinates of all other nickel atoms were fixed. This scheme has been checked

to reproduce the frequencies of the relevant modes within estimated numerical accuracy, by doing a frequency calculation in which the modes of the six first neighbors of the bonding nickel atom were also included in the dynamical matrix. For the latter, the computed IR frequencies differ insignificantly (within few cm^{-1}) from ones calculated when only water and bonded nickel atom were free.

4.3 Numerical accuracy discussion

The fractional occupation numbers DFT approach as outlined in section 2.8 allows a realistic treatment of the electronic structure of metallic systems, such as transition metal surfaces as well as adsorption processes on them. However, this method has the same deficiencies, as all density functional theory based methods, such as the incorrect description of van der Waals interactions. Further sources of errors are the use of the pseudopotential approximation and the incomplete basis set. Also the finite size of the computational box and the chosen number of **k**-points for sampling the Brillouin zone is necessarily a compromise between the numerical accuracy and computational costs.

In order to obtain an estimate for the systematic errors of computed IR frequencies in our scheme, a series of geometry optimization and spectroscopic properties test calculations has been made on water oligomers. The *absolute* errors in vibrational frequencies due to the different energy cut-off and pseudopotentials have been laid within 60 cm^{-1}.

An other important simplification concerning IR spectra calculations is the harmonic approximation for the calculations of the vibrational frequencies. When ab-initio predicted harmonic frequencies are compared with experimental IR spectra, which reflect an anharmonic potential energy surface, the higher vibrational frequencies tend to be overestimated while lower frequencies are not. Therefore,

in the literature, the theoretical harmonic frequencies are often empirically scaled to facilitate a comparison with experiment (148; 149). According this procedure, the adjusted frequencies are calculated as

$$\nu_i^s = \nu_i exp(-a\nu_i) \tag{4.3}$$

where ν_i^s and ν_i are scaled and unscaled frequencies corresponding to the vibrational mode i, and a is an fitting factor. This method allows to scale down larger vibrational frequencies while lower ones remain unaffected. In this work however, the computed frequencies have not been scaled with any empirical factors for the sake of clarity.

In order to make a reliable comparison to experiment, the change in the asymmetric/symmetric splitting in OH-stretch modes due to the formation of hydrogen bond has been computed. This change has been obtained from the difference in the frequencies for H-bonded and H-free stretch modes for H-donor molecule in water dimer and asymmetric and symmetric OH-stretch for a monomer:

$$\Delta\nu = (\nu_{\text{OH-free}} - \nu_{\text{OH-bond}})_{\text{dimer}} - (\nu_{\text{a}} - \nu_{\text{s}})_{\text{monomer}} \tag{4.4}$$

where ν_{a} and ν_{s} are frequencies of asymmetric and symmetric OH-stretch modes, respectively. It has been found that the discrepancies between computed and experimental (150) values of $\Delta\nu$ are about 20-30 cm^{-1}, which means that a significant part of the absolute errors has been canceled.

Since quantum mechanical treatment of nuclei lies out of the scope of this work, all quantum nuclear effects are neglected in reported calculations. To estimate the error caused by this classical approximation for the nuclei, the effect of zero-point motion on adsorption energies has been computed. For that, the

contributions in total ground state energies from the lowest vibrational states of the nuclei have been calculated. Using the expression for the energy of quantum harmonic oscillator: $E_{vib} = h\nu(n + \frac{1}{2})$ with $n = 0$ and the harmonic frequencies obtained by diagonalization of the dynamical matrix of considered systems (as outlined in 3.2), the change in adsorption energies has been calculated as:

$$\Delta E = \frac{h}{2}\Big(\sum_i \nu_i\,[\mathrm{Ni}\cdot(\mathrm{H_2O})_n] - \sum_i \nu_i\,[\mathrm{Ni}] - \sum_i \nu_i\,[(\mathrm{H_2O})_n]\Big) \qquad (4.5)$$

The computed zero-point shifts in adsorption energies for water clusters on flat nickel surface were less than 0.05eV.

Taking all these issues into account, we consider the error bars for calculated *changes* in IR frequencies as $\sim$30 cm^{-1}. The tolerance for computed adsorption energy *differences* is taken as 0.05 eV, according the test calculations discussed here and in 4.2.

While the estimated numerical accuracy is not sufficient for a reliable comparison of absolute frequency values, the calculated *trends* and *differences* are more trustworthy since they profit from error cancellations in the computational scheme. If the pseudopotential approximation, e.g., induces a certain red shift error in a particular mode, it will do so in the system of interest as well as in the reference system, so that the error cancels out at first order. Therefore, all vibrational modes of the water clusters on the flat and stepped surfaces have been compared with their counterparts of the corresponding clusters in vacuo. This enables the reduction of the impact of the numerical errors from the various computational approximations involved in the calculations.

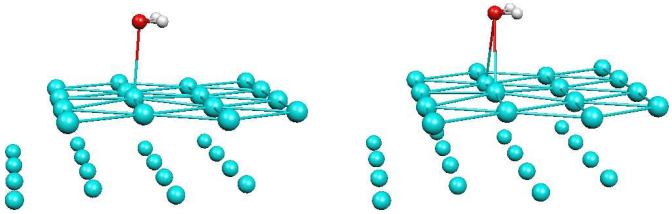

Figure 4.1: Pictogram of the two adsorption sites for the flat (111) nickel surface which constitute local minima of the potential energy surface: top (left) and bridge (right). Only two layers of nickel atoms are shown: the first surface layer is drawn with bonds, the second layer as spheres only.

4.4 Adsorption energies: flat and stepped surfaces

Starting with an absorption of a single water molecule, the corresponding absorption geometries have been optimized (33) for three typical adhesion sites: "top", "bridge" and "hollow" for a flat (111) nickel surface, as well as the "top" and "bridge" sites on a 221-surface which represents a step defect. Pictograms illustrating the top and bridge geometries on the flat and stepped surfaces are shown in figures 4.1 and 4.2. Despite the tetrahedral location of the lone pairs of the oxygen atom, the geometry optimization yields a flat arrangement of the molecule, so that the protons are found at the same distance from the surface as the oxygen (for both flat and step cases). The corresponding adsorption energies for these configurations which exhibit a (local) minimum of the potential energy surface have been calculated according the procedure described in section 4.2. The values of the adsorption energies as well as the distances between the bonded oxygen and nickel atoms are given in table 4.1. One can notice, that the energies of the top site differ from those of the bridge position by typically a factor of two in favor of the top configuration. Since the hollow system relaxed to the top site, we did not not consider it further.

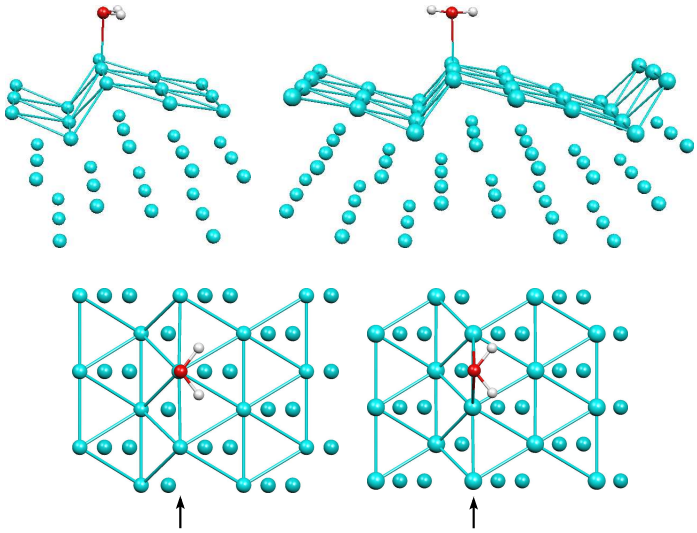

Figure 4.2: Pictogram of the two adsorption sites for the stepped (221) nickel surface: top/cis (upper left), top/trans (upper right). A comparison with the bridge site is given below, from a top view: top/cis (lower left), and bridge/cis (lower right). As in figure 4.1, the atoms of the top layer are drawn with bonds, those of the deeper layers as spheres only.

A possible vertical adsorption geometry for the flat surface on the hollow site and a tilted one (with one OH-bond parallel to the surface and the other OH normal to it) on the atop site have been explicitely checked (33). For both initial geometries, the optimization yields a flat orientation, and in the case of the hollow site, the oxygen atom also moves over to the atop site. Intermediate energy values from the optimization process are in the area of 0.1 eV during the turning process. This indicates that when the water molecule approaches the surface vertically, the adsorption strength is roughly half as large as in the parallel orientation. These results are in full agreement with the orientations found by Ranea, Michaelides and others (134; 135; 137) for water configurations on various other metallic surfaces.

Similar to the case of an adsorbed benzene molecule (138), the adsorption of a water molecule is significantly stronger on the surface with the step defect

	ΔE,eV	d_{Ni-O}, Å
$(H_2O)_2$	0.22	
$Ni_{flat}\cdot (H_2O)_{1,atop}$	0.242	2.26
$Ni_{flat}\cdot (H_2O)_{1,bridge}$	0.10	3.02
$Ni_{step}\cdot (H_2O)_{1,atop,\ trans}$	0.403	2.12
$Ni_{step}\cdot (H_2O)_{1,bridge,\ trans}$	0.249	2.46
$Ni_{step}\cdot (H_2O)_{1,atop,cis}$	0.397	2.10
$Ni_{step}\cdot (H_2O)_{1,bridge,cis}$	0.137	2.51
$Ni_{flat}\cdot (H_2O)_{2,atop}$	0.675	2.12
$Ni_{step}\cdot (H_2O)_{2,atop}$	0.900	2.09
$Ni_{flat}\cdot (H_2O)_{3,atop}$	1.26	2.08
$Ni_{flat}\cdot (H_2O)_{3,bridge}$	1.09	2.24

Table 4.1: Adsorption energies (ΔE) computed relative to isolated water molecules according to eq. (4.1), such as to include also the hydrogen bonding energy and the Ni-O bond lengths (d_{Ni-O}) for the various water oligomers and surfaces (33).

than on the flat one. The adsorption energy for the latter is roughly equivalent to one hydrogen bond (cf. the $(H_2O)_2$ value in table 4.1), while the step provides about twice that attraction. There exists a cis and a trans orientation (both shown in figure 4.2) for the step defect, but their adsorption energy is almost the same. Thus, the top position on the step surface reaches the highest energy value, which is also approximately equal to the typical hydrogen bond energy of a fourfold-coordinated liquid water molecule.

The second step in water adsorption on the surface is the attachment of a second water molecule to the first one. For this purpose, the geometries of a water dimer on the both nickel surfaces (flat and with the step defect) have been optimized (33). Since the monomer adsorption is energetically significantly more favorable on the top site than in the bridge position (see table 4.1), only the first configuration has been considered further.

The computed Ni-O bond distances and adsorption energies for the water dimer are shown in table 4.1. The energies are taken relative to isolated water

molecules in order to have a common reference for all systems. On both the flat and the step surfaces, the attachment of an additional water molecule to the first one through a hydrogen bond yields an additional 0.43 eV and 0.5 eV, respectively. These energies are at least twice as large as would be expected for a standard hydrogen bond (cf. the water dimer in table 4.1), leading again to an adsorption strength that is comparable to that of a water molecule in liquid water. Especially on the step defect, two water molecules attach with an energy that is equivalent to four hydrogen bonds, while still possessing two hydrogen bond acceptor sites (one on each oxygen) and two dangling donor protons. Thus, the dimer adsorption on the metal surface can energetically compete with the solvation of the second molecule in liquid water, even though the optimized cluster on the surface is not directly comparable to the situation in liquid water due to the high dynamics of the hydrogen bond network at finite temperature.

For the flat surface, a part of this increased energy probably stems from the decreased Ni-O bond distance compared to the water monomer, whereas the step surface does not show this effect as much.

Finally, the adsorption of a third water molecule onto an H_2O dimer on the flat nickel surface has been considered (33). As before, the energy and the bonding distance of the first water are shown in table 4.1 for both the bridge and the top sites. The energy difference between bridge and top geometries is conserved upon adsorption of further molecules, implying that the secondary water molecules do not feel any significant influence from the adsorption site of the first one 4.1. It is surprising that the third water increases the total adsorption energy by almost 0.6 eV, thus practically doubling the value of the dimer.

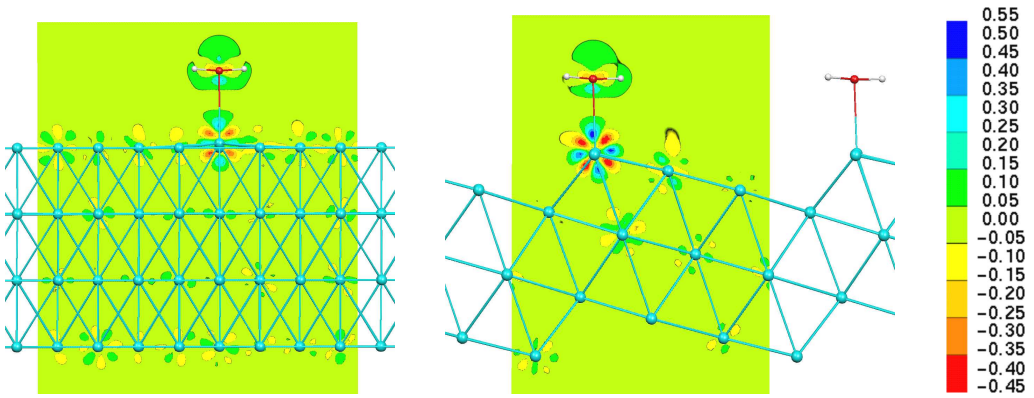

Figure 4.3: Density difference plots for the adsorption of a water molecule on the flat (left, atop configuration) and the step surfaces (right, atop trans configuration). The scale is given in units of e/Å^3.

4.5 Electron density difference maps

To understand the water adsorption in more details and to investigate the origin of the computed adsorption energies the electron density differences have been calculated (33) according to Eq. (4.2). Some of the corresponding electron density difference maps for both the flat and step surfaces are shown in figure 4.3 and figure 4.4. The plots represent the density of the aggregate minus the sum of the densities of the isolated surface and the water oligomers at the top site for the flat nickel (top-trans configuration for the step).

4.5.1 Adsorption strength at a step defect

Figure 4.3 illustrates the electronic density distributions for the case of a water monomer adsorption on both the flat and the step surfaces. The formation of a weak bond between the surface nickel atom and the oxygen is clearly visible through the displacement in electronic density (dark green regions). To some extent, an additional density on top of the water molecule is also found, while relatively little is removed from the central area around the oxygen. Most of

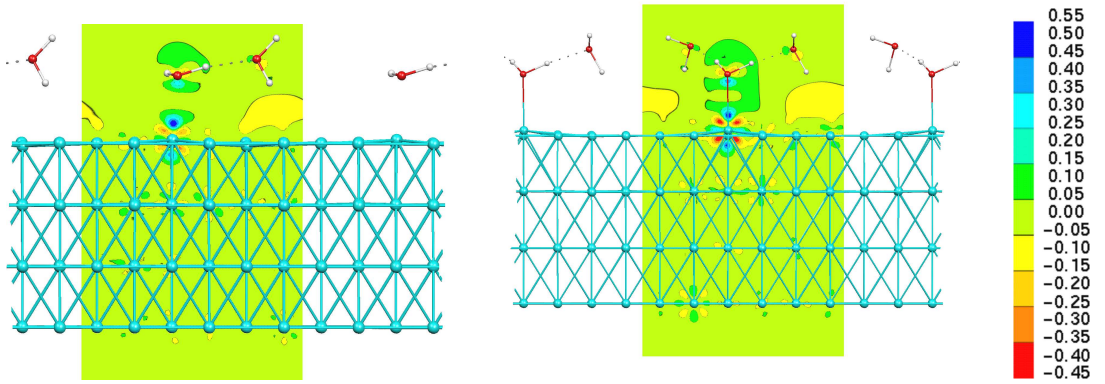

Figure 4.4: Electron density difference plot for the adsorption of a water dimer and trimer on the flat surface.

the electronic density is taken from the bonding nickel atom, which is strongly polarized, and its first neighbors.

Similar to the case of an adsorbed benzene molecule (138), the polarization of the nickel atom which is bonded to the water molecule is significantly stronger on the step surface than on the flat one. Thus, the density deference plots are consistent with previously calculated adsorption energies. For the perfect surface, electronic density plots demonstrate a weaker polarisation of the bonding and neighboring nickel atoms as well as a lower electronic concentration in the nickel-oxygen region, which leads to a weaker Ni-O bond and lower absorption energy.

4.5.2 Characterization of non-covalent bonding

The electronic density difference for the dimer adsorption on the flat surface is shown in figure 4.4 (left). According to Eq. (4.2), the isolated water *dimer* is taken as reference system, in order to suppress the charge difference due to the water-water hydrogen bond, and to show rather how much this hydrogen bond is *changed* due to the adsorption on the surface. The plot reveals that the bonding mechanism of the first water molecule is essentially the same as for the monomer,

except that the charge displacement around the first water is now less symmetric than before. There is a region of strongly increased electron density leading to a Ni-O bond, and an additional charge increase on top of the first water molecule. Furthermore, the amount of electronic charge density which is found on top of the bonding Ni atom is significantly stronger than for the water monomer (deep blue color in figure 4.4 (left) compared to light blue in figure 4.3 (left)).

It is interesting to note that the second water molecule does not bind directly to the surface, it is even repelled from it. The second oxygen is not accumulating any electronic density towards the metal surface, and there is a distinguishable region of decreased electron density (yellow color coding) below the hydrogen which points towards the surface. In contrast to this, the hydrogen bond between the two water molecules becomes slightly stronger than in the isolated dimer, as seen by the polarization of the H-bond accepting oxygen.

The same trend is significantly more pronounced on the density difference map of the trimer, shown in figure 4.4 (right) for the top site. The plot reveals a highly increased electronic charge density in the Ni-O bond region, at the expense of the areas below the dangling protons of the secondary water molecules. Together with a very high polarization of the binding nickel atom as well as slightly stronger hydrogen bonds between the waters, this indicates a much stronger binding of the first oxygen atom, which is translated in turn in much higher adsorption energy, almost twice as large as for the dimer case.

It is interesting that this increased binding of the first water is practically not related to any of its geometric properties, but is rather due to the mere presence of secondary water molecules, which constitute a kind of a first solvation shell. These additional water molecules perturb and repel the electron density at the metal surface in the neighborhood of the initial molecule in such a way that the polarization of the bonding nickel is significantly increased. This phenomenon

is already visible for the adsorbed dimer, but even stronger in the presence of a third water molecule.

4.6 IR vibrational frequencies

In this section, DFT calculations of IR signatures of small water clusters adsorbed on nickel surfaces are reported. According to the results from the adsorption energy calculations presented in table 4.1, the top configuration is energetically favorable in both the flat and the step cases, while the adsorption energies for two possible trans and cis water orientations for the step defect case are almost the same. Thus, only the top adsorption site for the flat surface and the top-trans site for the surface with a defect are considered (see figure 4.5), which are the most energetically favorable configurations. This study clarifies in detail the effect of a step defect on vibrational modes and their frequencies. Also the changes in IR frequencies when a second and third molecule are added to the initially attached one are investigated. Particular features are the modification of certain water modes due to hydrogen bonding and the appearance of new vibrational modes involving the nickel-oxygen bond. The computed red shift of

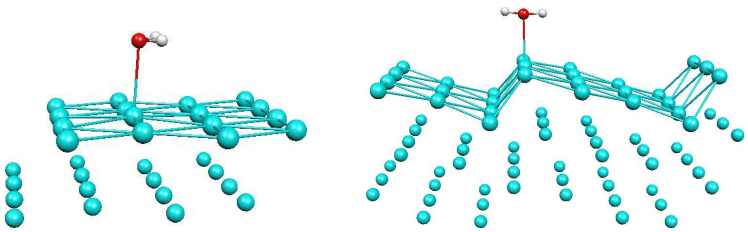

Figure 4.5: Pictogram of the most energetically favorable adsorption sites, which are chosen for IR spectroscopic calculations: top for the flat (111) (left) and top-trans for stepped (221) (right) nickel surfaces. Again, only two layers of nickel atoms are shown: the first surface layer is drawn with bonds, the second layer as spheres only.

OH-stretch and bending modes due to the adsorption is in a qualitative agreement with experiment. Although the numerical accuracy is not yet comparable to experiment, it will be shown that these calculations allow for characterization of and distinguishing between relevant adsorption configurations - e.g. whether the water is adsorbed on a flat surface or at a step defect.

4.6.1 Vibrational modes: adsorbed and free water oligomers

The computed harmonic frequencies for free and adsorbed water oligomers are presented in table 4.2. There, we define the first water as the H-bond donor molecule that is adsorbed on the nickel surfaces. The second and the third waters are H-bond acceptors. If the OH covalent bond points into vacuum we label the corresponding stretch vibration as "H free", if it points to the surface the label is "H-Ni", and finally "H bonded" defines the OH stretch of the hydrogen bonded mode. All these possible orientations are illustrated in figure 4.6.

Calculated vibration modes of the small adsorbed water clusters reveal strongly coupled motion of water molecules as well as a complex interaction of water with

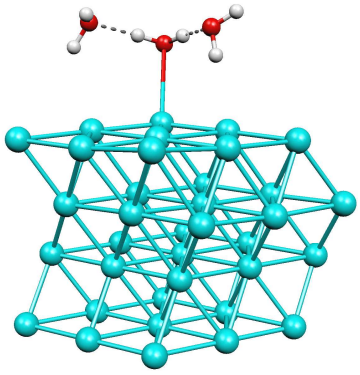

Figure 4.6: Configuration of the water trimer adsorbed on the flat Ni surface. Central molecule is defined as the 1^{st} water in table 4.2, left and right ones are the 2^{nd} and 3^{rd} waters in table 4.2, respectively.

	System	OH-stretch H free	OH-stretch H bonded	OH-stretch H-Ni	Bending	Ni-O	Other modes
monomer							
1^{st} water	Free	3833a, 3724s			1586		
	Flat Ni	3664a, 3564s			1536	174	513, 392, 200, 196, 98
	Step Ni	3733a, 3619s			1544	241	477, 467, 196, 155, 112
dimer							
1^{st} water	Free	3792	3568		1616		
	Flat Ni	3702	3092		1611	217	887, 607, 404, 318, 297, 188, 184, 120
	Step Ni	3728	3052		1591	318	990, 559, 521, 437, 294, 249, 212, 192, 139, 105
2^{nd} water	Free	3829a, 3721s			1589		
	Flat Ni	3750		3449	1558		474, 404, 318, 297, 148
	Step Ni	3742		3363	1556		521, 437, 294, 249, 212, 192, 161, 139, 105
trimer							
1^{st} water	Free		3692a, 3610s		1608		
	Flat Ni		3268a, 3227s		1636	368	919, 876, 674, 479, 266, 248, 237, 188, 187, 184, 158, 135
2^{nd} water	Free	3842a, 3729s			1614		
	Flat Ni	3755		3434	1555		479, 374, 266, 248, 237, 188, 187, 184, 158
3^{rd} water	Free	3834a, 3722s			1653		
	Flat Ni	3747		3419	1547		479, 374, 266, 248, 237, 188, 187, 184, 158

Table 4.2: Calculated vibrational frequencies for adsorbed and free water oligomers, cm^{-1}. The 1^{st} water corresponds the central molecule in fig (4.6), the 2^{nd} and 3^{rd} ones are left and right waters in fig (4.6), respectively. Frequencies of asymmetric and symmetric OH-stretch modes are denoted by a and s letters, respectively.

the nickel surfaces. The corresponding frequencies are listed in table 4.2. The nickel-oxygen binding is separated from other water-nickel modes, since this vibration, as we show later, is very sensitive to the surface type and the size of adsorbed clusters and therefore can be used for characterization of relevant adsorption configurations.

The calculations of IR intensities would enable the detection of modes which are symmetry-allowed but have low intensity in the spectrum (silent modes) or those that might be hidden in experimental spectra below other more intense peaks. However, for metallic solids (and surfaces) the calculations of IR intensities is not straightforward. This is because the electronic dipole moment in metallic systems is difficult to define due to delocalization of electronic orbitals. Thus, the problem of IR intensities in metallic systems can not presently be addressed within the implementation used.

In the next sections, it will be discussed in detail how the stretch and bending modes of water are modified upon adsorption and in particular, how the shift in IR frequencies depends on the surface type and on the hydrogen bonding situation. It will also be shown, how the new modes of adsorbed water oligomers can be used to distinguish the perfect nickel surface from the one with the step defect.

4.6.2 Red and blue shifts due to the adsorption

For the water monomer, both asymmetric and symmetric OH-stretch modes are red shifted by about 200 cm^{-1} on the flat Ni surface (table 4.2) while on the step defect the red shift is only half as large. This red-shift shows a weakening of the OH bonds in the adsorbate in both cases. It is interesting that the flat surface lowers the stretch frequencies more than the step, although the adsorption

energy and thus the Ni-O bond (table 4.1) are stronger for the latter (2.26 $\AA$ and 2.12 $\AA$ of Ni-O bond length for flat and step case correspondingly). This increased adsorption strength is also reflected in the electronic density plots 4.3 as well as in the computed Ni-O oscillation, which is at 174 cm^{-1} on the flat surface but at 241 cm^{-1} on top of a defect. The stronger adsorption could go along with a reduced strength of the OH bonds, which apparently is not the case. Instead, it seems that the flat surface has a stronger repulsive effect on the hydrogens than the stepped one. In the latter, there is more free space between the surface and the protons, which constrains the OH vibrations less than in the flat case. The bending mode is red shifted approximately 50 cm^{-1}, independently of the surface structure.

In the gas-phase water dimer, each molecule has one symmetric and one asym-

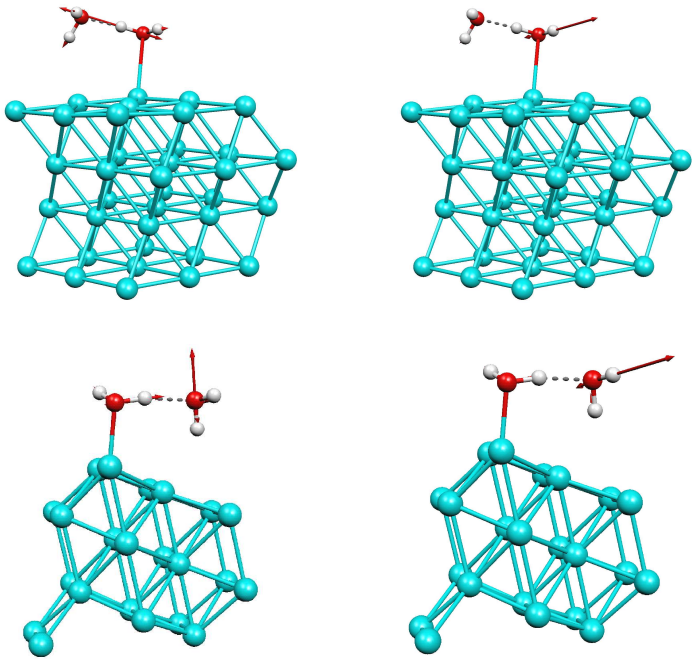

Figure 4.7: Pictogram of selected isolated OH vibrations for adsorbed water dimer on the flat Ni surface (up) and on the step defect (down). Only the first layer of Ni atom is shown.

metric OH-stretch mode, with slightly lowered frequencies for the hydrogen bond donor. Upon adsorption, the symmetry of these modes is broken and they transform into isolated OH vibrations. Some of these new modes are illustrated in figure 4.7, where OH stretch for the hydrogen bond donor on the flat surface and for the acceptor molecule on the step defect are shown. However, for both the donor and the acceptor molecules we still obtain one high-frequency mode and one at reduced frequency. The strongest stretch modes appear at about the same frequencies as the symmetric stretch of the acceptor molecule in the isolated water dimer, both on the flat surface and on the step. Also for the bending modes, only little differences are visible between the isolated dimer and the two adsorbates. In contrast to this, the four bond stretch modes of the free water dimer are transformed due to the adsorption into individual OH stretch modes, some of which are strongly red-shifted with respect to the vacuum dimer. The changes in this high-frequency region of IR spectra for free and adsorbed water dimer are illustrated in figure 4.8. In particular on the flat surface, the new OH modes of the H-bond acceptor molecule are now split by almost 300 cm^{-1} (3750 cm^{-1} and 3449 cm^{-1}), while its symmetric/antisymmetric modes in vacuo show only a split of ∼100 cm^{-1} (3829 cm^{-1} and 3721 cm^{-1}). The first adsorbed water (H-bond donor) even demonstrates a splitting of ∼600 cm^{-1} between its OH bond stretches (3702 cm^{-1} and 3092 cm^{-1}), while in the isolated dimer the difference is only 220 cm^{-1} (3792 cm^{-1} and 3568 cm^{-1}). This reflects the fact that the first water molecule is much more strongly bonded to the nickel surface than the second one.

The asymmetric/symmetric stretch splitting is even more pronounced on the step defect (11 % more for the H-bond donor and 26 % more for the acceptor molecule compared to adsorption on the perfect surface), which is again confirmed the stronger adsorption on this type of defects. Most of these high-frequency

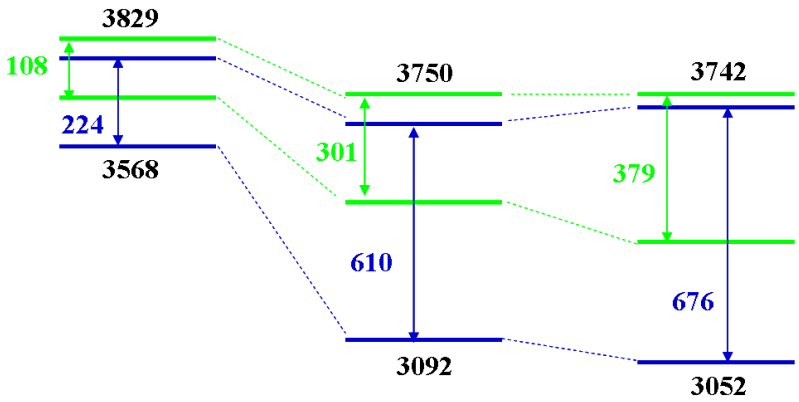

Figure 4.8: OH-stretch frequencies for a water dimer in vacuo (left), on the flat Ni surface (middle) and on the step defect (right). Blue lines: H-bond donor water molecule, green lines: H-bond acceptor molecules, symmetric/asymmetric splitting is shown in blue and green for donor and acceptor molecules, respectively. Absolute values of the strongest and the weakest stretch vibration for each of three systems are written in black. All frequencies are given in cm^{-1}.

stretch modes, however, are not suitable to a proper discrimination between the flat and the step adsorption site. Only the effect to the actual adsorption is of course clearly visible.

For the incremental adsorption of a third water molecule, we considered only the flat surface, for which the geometry is shown in figure 4.6. As expected from the symmetry of the system, the second and the third water molecule have very similar vibrational modes and frequencies, resulting in a quasi-degeneracy of the spectrum. The dependence of OH-stretch vibrations on cluster size, i.e. on hydrogen bonding, is illustrated in figure 4.9. Compared to the adsorbed dimer, the OH-stretch modes of the trimer free protons appear at about the same frequencies ($\sim$3750 and $\sim$3450 cm^{-1}), showing similar $\sim$300 cm^{-1} asymmetric/symmetric splitting due to the adsorption.

In contrast to this, the H-bond donor protons of adsorbed molecules produce a specific pattern in computed IR spectra. The trimer OH-stretch modes

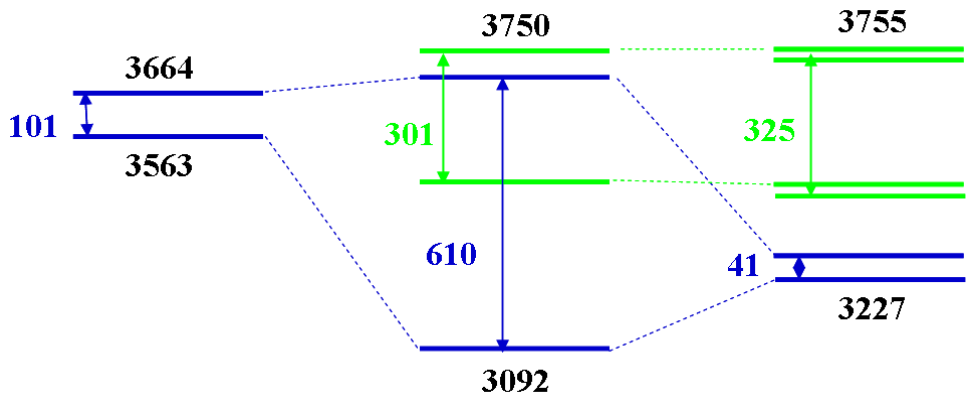

Figure 4.9: OH-stretch-frequencies for water oligomers on the flat Ni surface: monomer (left), dimer (middle) and trimer (right). Blue lines: H-bond donor water molecule, green lines: H-bond acceptor molecules, symmetric/asymmetric splitting is shown in blue and green for donor and acceptor molecules, respectively. Absolute values of the strongest and the weakest stretch vibration for each of three systems are written in black. All frequencies are given in cm^{-1}.

(3227/3268 cm^{-1}) are about 150 cm^{-1} higher in frequency than the corresponding mode for the dimer (3092 cm^{-1}) and about 350-400 cm^{-1} lower than for the monomer as shown in figure 4.9. While the bending modes remain almost unchanged upon adsorption, the clearly visible differences in the OH-stretch region of the spectra might provide us with an opportunity to distinguish between sizes of absorbed water oligomers.

4.6.3 Role of a step defect

For adsorbed monomer, there are several vibration modes which might be used to distinguish the surface type. First, there is the Ni-O oscillation, which is at 174 cm^{-1} on the flat surface but at 241 cm^{-1} on top of a defect (table 4.2). This blue shift reflects a stronger binding potential of the defect site, which is consistent with computed adsorption energies (table 4.1) and electronic density plots 4.3. Secondly, an interesting difference arises in wagging and twisting water modes.

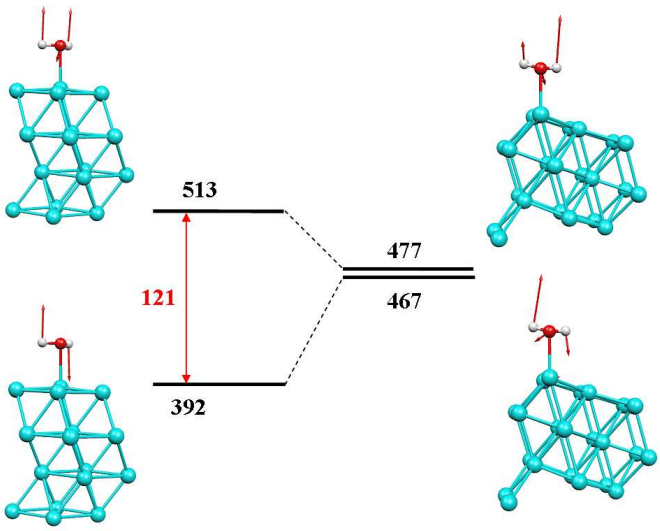

Figure 4.10: Wagging and twisting modes for water monomer adsorbed on the ideal Ni surface (left) and on the Ni surface with a step defect (right). The splitting is shown in red, absolute values of the vibration frequencies are written in black. All frequencies are given in cm^{-1}.

The protons, which are not bonding to the surface (see the density difference plots in figure 4.3) may oscillate symmetrically or asymmetrically towards the surface as it shown in figure 4.10. On flat nickel these two modes differ by 120 cm^{-1} while they are almost indistinguishably on the step, where the distance to the nearest Ni atom is larger for both protons. Although this phenomenon is somewhat unexpected, it provides a mean to discriminate the adsorption on the two surface modifications.

The computed dimer OH-stretch modes reveal that the frequency of the proton motion towards the nickel surface (the lowest OH-stretch for the acceptor molecule) is clearly affected by the adsorption site (see figure 4.8). The step surface yields a mode which is about 90 cm^{-1} higher than the corresponding mode on the flat. Also the two Ni-O modes at 217 cm^{-1} for the flat surface and 318 cm^{-1} for the stepped one show a significantly higher frequency for the step defect (see figure 4.11), again in agreement with computed adsorption energies

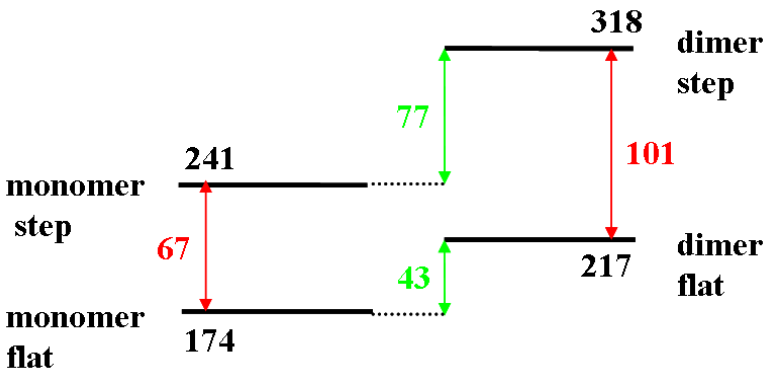

Figure 4.11: Ni-O vibration frequencies for the monomer (left) and the dimer (right) adsorbed on the flat (down) and stepped (up) surfaces. Differences due to the step defect are shown in red, due to the hydrogen bonding in green. Again, all frequencies are given in cm^{-1}.

and Ni-O bond lengths (table 4.1).

For trimer, the Ni-O mode of the central water molecule is about 150 cm^{-1} higher than for the dimer (368 cm^{-1} vs. 217 cm^{-1}). This clearly indicates that the Ni-O bond of the first adsorbed water is strengthened due to the arrival of the third molecule (in agreement with changes of Ni-O bond length: from 2.26 $\mathring{A}$ for monomer, to 2.12 $\mathring{A}$ for dimer and 2.08 $\mathring{A}$ for trimer) as had already been reported previously in table 4.1. The electronic density which constitutes the weak bond between the surface nickel atom and the oxygen of the adsorbed water is mostly taken from the bonded nickel atom, which is strongly polarized due to the adsorption, and its first Ni neighbors. This bonding mechanism remains essentially the same for all small water clusters that we have studied (see the density difference plots in figure 4.3 and figure 4.4).

Thus, there may be a way to discriminate the two adsorption sites from those vibrations.

An other interesting feature of the step defect shown in figure 4.11 is an enhancing of the hydrogen bonding effect, by which the second and the third

water molecules increase the adsorption energy and make stronger the nickel-oxygen bond which reveals in Ni-O bond length (table 4.1) as well as in electronic density plots 4.3, 4.4. The change in the nickel-oxygen bond frequency due the H-bonding with the second water is almost twice as large on the step defect than on the flat nickel (77 cm^{-1} vs. 43 cm^{-1}), see figure 4.11. The effect of the H-bonding on the computed Ni-O vibration frequency of adsorbed water has nearly the same magnitude as the step defect of the nickel surface.

4.6.4 Comparison with experiment

There are only a few experimental IR studies in the literature about water adsorbed on nickel surfaces (37). Also, the specific configurations of the investigated adsorbates and their cluster size have always had a somewhat speculative character. At low coverages around θ=0.03, it can safely be assumed that only monomolecular clusters are formed, while at high coverage (θ=0.66), the water is found in a hexagonal close-packed structure (37), the so-called ice-like bilayer. The details of the water structure at intermediate coverages are not known with certainty. In the experimental studies, the assignment of frequencies to modes and even to oligomers is based on experience and has a somewhat empirical character. Thus, a direct assignment of the frequencies of (37) to our calculated IR signatures is not possible. However, a comparison of the set of computed frequencies with the experimental spectra gives us the possibility to obtain structural features about intermediate water coverages.

It table 4.3, the computed and the experimentally observed red shifts of the IR frequencies upon adsorption for the lowest coverage that presumably corresponds to adsorbed water monomers (37) are presented. While for the flat nickel surface the agreement with experiment is reasonably good, the experimental spectrum

Vibrational mode	Flat Ni (calc)	Step Ni (calc)	Ni (exp) (37)
Assym. stretch	169	100	181
Sym. stretch	161	105	181
Bending	52	42	18

Table 4.3: Red shift in stretch and bending frequencies of water monomer due to the adsorption on a nickel surface in cm^{-1}. The frequencies of adsorbed molecule were referenced to the corresponding values in vacuum.

would not fit to the set of frequencies computed for the adsorption on the step site.

IR frequencies computed with using the deuteron mass have been also calculated, in order to compare to the IR study of ref. (37). Table 4.4 shows the frequencies of OH-stretch and bending modes thus obtained for the water oligomers, together with the experimental IR lines at θ=0.03, θ=0.1 and θ=0.33 coverage. Although a perfect match is not obtained, a reasonable agreement with the calculated spectra is found. The monomer asymmetric stretch mode $2684cm^{-1}$ does not appear in experimental spectra, since it is prohibited by the surface selection rule. The experimental lines around 2632 cm^{-1} and 2562 cm^{-1} are not among our computed dimer and trimer frequencies. This might be a consequence both of the anharmonicity error in computed frequencies discussed in section 4.3 and of the broadness together with a relatively low intensity of these experimental peaks in spectra (37). The low-lying peaks around 2460 cm^{-1} at both θ=0.1 and θ=0.33 coverages and 2434 cm^{-1} for the latter provide an evidence that already at low coverage, some clusters of more than one water molecule may have formed on the surface.

In their paper (37) experimentalists report that due to the broadness of some of measured peaks, i.e. at $2701cm^{-1}$ and at $2638cm^{-1}$, they cannot exclude the existence of more than two kinds of adsorbate species on the surface at relatively

D_2O oligomers (calc)			D_2O clusters (exp) (37)		
			coverage		
monomer	dimer	trimer	0.03	0.1	0.33
	OD-stretch				
2684	2735	2738		2701	2696
	2695	2731		2632	2638
2567	2500	2488	2474	2562	2560
	2248	2480		2463	2460
		2400			2434
		2327			
	Bending				
1125	1173	1191	1161	1186	1190
	1140	1138		1175	
		1133			

Table 4.4: Comparison of calculated IR frequencies with experiment for the deuterated water oligomers adsorbed on the flat (111) nickel surface. The frequencies are given in cm^{-1}.

lower coverages. Therefore, this questions deserves further investigations, also from the experimental side.

4.7 Conclusions

In this chapter, the energetic details and the electronic mechanism of the adsorption of water oligomers on nickel surfaces with and without a step defect are reported. The data shown indicates an increased binding strength on the step and in "top" geometries. The findings are in good agreement with previous theoretical and experimental results for similar systems (130), where an energetic enhancement of water adsorption was found along step defects on platinum surfaces.

The electronic density difference maps show that additional water molecules tend to strengthen the nickel–oxygen bond. This effect leads to a significant

stabilization of the binding of the first water molecule and to strongly increased binding energies of the dimer and trimer complexes, which can definitively compete with those found in liquid water. The second and third water molecules increase the total binding energy by the equivalent of more than two hydrogen bonds each, which corresponds to the average binding energy per molecule of standard fourfold coordinated water.

Furthermore, the vibrational properties of water oligomers absorbed on flat and stepped nickel surfaces are investigated. The changes in the stretch and bending modes as well as the frequencies of new water-nickel modes appeared due to adsorption are calculated.

It is shown that a step, which is the simplest possible surface defect, influences significantly the vibrational modes and frequencies of the small absorbed clusters as well as the shift in frequencies due to the adsorption. Also the question of how the new modes of adsorbed water oligomers can be used to distinguish the perfect nickel surface from the one with the step defect is discussed.

The dependencies of computed IR frequencies on the surface type and on the hydrogen bonding situation are consistent with the adsorption energy calculations and electronic density difference maps and complementary to this, provide us with an opportunity to verify theoretical results by available experimental data.

Although the agreement with experiment is qualitative, our accuracy is sufficient to characterize vibrational modes and distinguish between relevant adsorption sites (perfect surface or the step defect) and sizes of adsorbed clusters.

Chapter 5

Aqueous solvation of HCl: proton NMR signatures of solvated ions

5.1 Motivation

The investigation of the microscopic structure and dynamics of complex aqueous solutions is a challenging topic for modern physics and chemistry. The nature of the interactions between water molecules and dissolved ions is crucial for a broad range of chemical, biological, and physical processes that occur in solution. Biomacromolecular folding and self-assembly, for example, which take place in aqueous solutions are strongly affected by the microscopic surrounding (151). In order to investigate the solvation of ions and molecules, a variety of experimental methods are successfully applied, such as Raman and IR spectroscopy (5), ultrafast spectroscopy (152; 153; 154; 155; 156) and neutron and x-ray diffraction techniques (1). However, precise quantitative results are still rare due to severe difficulties in extracting accurate and unambiguous information from experimental data.

In crystalline systems, scattering experiments can provide very accurate atomic

coordinates. Liquid systems, however, lack the required long-range order, which limits the applicability of these scattering techniques. Complementary to this, NMR experiments are able to probe local structure without the need of long-range order. Their sensitivity to the local chemical environment of an atom is one of the key advantages of this method. The dependence of the NMR chemical shifts of a given stable molecule on its chemical surrounding is well-established for solutions, where the change in the NMR resonance is called the solvent shift. Its nature and magnitude are due to the interaction of the solvent molecules with the solute, which can be hydrogen bond networks, van-der-Waals forces, or other non-bonded interactions. While the NMR signal is very sensitive to changes in the average structural configuration, the intrinsic duration of the measurement process is too long compared to the fast fluctuations of the molecular arrangement in solutions. Hence, the NMR signal yields an average over all fluctuations and does not allow us to get individual lines of protons involved in exchange processes. A case in point are acidic molecules, which dissociate in aqueuos solution into charged ions, one of which is a proton. Such an excess proton will migrate and exchange with regular water protons via a Grotthus-style hopping process. According to the Grotthus idea, the excess positive charge, not the proton itself, migrates through the hydrogen-bonded network by a concerted series of hydrogen-bond formation and breaking steps. This process happens on a sub-picosecond timescale and is therefore averaged in the ^{1}H NMR spectrum.

In recent years, much attention has been dedicated to the solvation shell structures and the dynamics of ions in aqueous solutions and a variety of ab initio molecular dynamics simulations of aqueous acids have been performed (10; 25; 26; 28; 42; 43; 44; 45; 46; 47; 48). While the full microscopic structure of solutions are easily accessible from ab initio simulations (27; 28; 40), there is often no immediate comparison with experiment with the exception of the assignment

of radial distribution functions to X-ray experimental data (8; 9).

However, the ab-initio simulation of the structure and magnetic resonance properties of liquid water and aqueous solutions is not yet routinely done. This is partly due to the dynamically fluctuating hydrogen bond network as the central structural driving force, which requires an expensive phase-space sampling of the NMR parameters. The theoretical investigation of nuclear shieldings and chemical shifts can not only improve greatly our knowledge about detailed structure of ionic solvation shells but also bridge the gap between experiment and theory. Proton chemical shifts are very sensitive to the character of the hydrogen bond network and are accessible via ab initio calculations. Moreover, they provide an opportunity to compute the individual NMR signatures of a variety of species and sub-structures that cannot be resolved in experiment.

In this chapter, the first-principles calculation of the ^{1}H NMR chemical shift distribution of an HCl aqueous solution as a function of concentration is presented. The ab-initio results are validated by comparing the computed averaged chemical shifts with experimental spectra obtained by liquid-state ^{1}H NMR experiments for the same concentration values. To clarify the origin of the obtained chemical shift distributions, the set of ab initio proton shifts is decomposed into contributions from different types of geometrical configurations: Eigen-/Zundel-complexes, the first solvation shells of the Cl^- ions, and the regular water molecules. Finally, the computed histograms of instantaneous ^{1}H NMR chemical shifts are analyzed and discussed in term of calculated individual NMR chemical shift signatures of solvated species.

5.2 Methods and computational details

5.2.1 Ab-initio molecular dynamics simulations

In this work, a pure water system consisting of 64 H_2O molecules, a singly protonated water (64 H_2O molecules and one H^+), as well as HCl solutions at two concentrations have been studied. These acidic samples contained three and six (dissociated) H^+Cl^- molecules, with 61 and 58 water molecules, respectively, yielding concentrations of c=2.6M and c=4.9M.

A periodic supercell of a=15.6 $\AA$ / box length has been used for all systems, such that the known experimental densities at the two different acid concentrations are reproduced. The computational setup was the same as in a previous Car-Parrinello (CP) simulation (47), which had been done on a larger sample (∼128 molecules for the acidic solutions). It has been found that all structural parameters (such as radial distribution functions) were essentially identical in the two molecular dynamics (MD) runs.

All MD simulations have been performed at an average temperature of T=330K. This value is somewhat higher than the corresponding experimental temperature, in agreement with recent findings that Car-Parrinello MD simulations at temperatures closed to the triple point tend to yield overstructured water (41; 157). The reason is the known overestimation of the H-bonds strength caused by the exchange-correlation functionals, leading to a stiff structure of liquid water which exhibits too less fluctuations. For the generation of MD trajectories, all hydrogen atoms were assigned the mass of the deuterium isotope in order to improve decoupling of the dynamics of the ionic and electronic subsystems over a longer period of time and to increase computational efficiency, allowing a larger timestep in the numerical integration of the equations of motion. For the fictitious electronic mass in the Car-Parrinello Lagrangian, a value of 700 a.u. was chosen,

corresponding a timestep of 6.0 a.u. (0.145 fs). All simulations were run for at least 15 ps after equilibration to gather proper statistics.

The calculations have been performed in the framework of density functional theory using the gradient corrected exchange- correlation functionals proposed by Becke (91) and Lee, Yang, and Parr (BLYP) (92), which is known for a good description of aqueous systems (10; 40). The Kohn-Sham orbitals were expanded in plane waves with an energy cutoff of 70 Ry. Only valence electrons were considered explicitly, with a semi-local norm conserving Martins-Troullier pseudopotential taking into account the interactions between core and valence electrons.

5.2.2 NMR calculations along the MD trajectories

The calculations of the NMR chemical shifts have been done on the basis of the previously obtained CP trajectories as described above. The same computational setup has been used for all systems, in order to provide a consistent description for all concentrations. For the spectroscopic calculations, pseudopotentials of Goedecker type (96; 158) as in previous studies (159) have been used, since these potentials turned out to be somewhat more accurate than the softer Martins-Troullier variants.

The choice of the deuterium isotope in the MD simulations is not crucial in this context, since the atomic masses and spins do not figure in the electronic ground-state and magnetic perturbation Hamiltonians. Hence, the chemical shifts obtained for protons are analytically identical to those for deuterons, for a given molecular conformation. Only in Newton's equation of motion (which govern our molecular dynamics simulations), the atomic masses appear explicitely, which results in somewhat different trajectories when using deuterons instead of protons.

Experimentally, the observed H/D isotope shift is caused by the different spatial extension of the two nuclei (a nuclear quantum effect). Such an effect could be computed by ab-initio path-integral calculations or similar techniques (81; 160; 161), which is beyond the scope of the present work. However, this isotope shift is usually not very large (162), although some particular molecules represent exceptions to this rule (163). Furthermore, such an isotope effect would manifest itself as an essentially constant offset in the NMR chemical shifts, leading to the same relative shifts between different HCl concentrations.

Twenty snapshots for acids and sixteen for water were extracted from the MD simulations, and their proton nuclear shieldings were computed under full consideration of the periodic boundary conditions, following the method described in refs. (113; 119; 164). For illustration, a snapshot taken from one of the simulations at high concentration is shown in figure 5.1. This scheme provided about 2000 individual shielding values for water and 2500 for each of the considered acid concentrations. These values would correspond to a sample where the atoms were frozen at their instantaneous positions. The computed nuclear shieldings were referenced to the time- and atom-averaged shielding of the pure liquid water system, $\sigma^{\mathrm{ref}} = \sigma(\text{pure } H_2O)$, according to the usual experimental convention:

$$\delta(X) \;=\; \frac{1}{3}\,\mathrm{Tr}\;\sigma^{\mathrm{ref}} - \frac{1}{3}\,\mathrm{Tr}\;\sigma(X) \tag{5.1}$$

so that $\delta(\text{pure } H_2O)$=0ppm. With respect to TMS (i.e. using $\sigma^{\mathrm{ref}} = \sigma(\mathrm{TMS})$ instead of eq. (5.1)), our liquid water would have its NMR chemical shift resonance at $\delta^{\mathrm{TMS}}(H_2O)$=5.9ppm. While this value is somewhat above the experimental one (4.8ppm), it is in agreement with previous ab-initio NMR calculations for several liquid water systems (23; 24), which also overestimated the proton shifts. The observed deviations illustrate the deficiencies of the BLYP xc-functional to

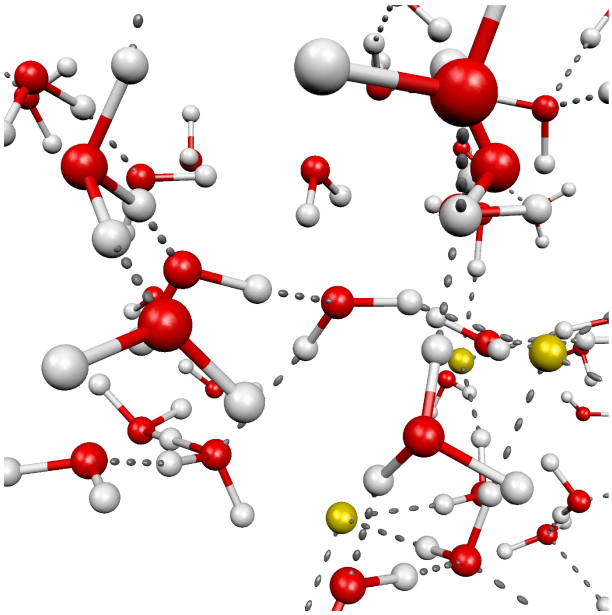

Figure 5.1: Geometry of a snapshot taken from the MD-simulations at 4.9M HCl concentration. Apart of the normal hydrogen bonding network of water, the solvation of some of the chlorine ions (yellow) as well as a Zundel ion (bottom left) and two hydronium ions (top left and bottom right) are visible.

describe the hydrogen bond network of water, which turns out to be somewhat over-structured (41; 105; 157). Nevertheless, the computational methods used here have already been successfully used to predict and interpret experimental solid-state NMR data (159).

The calculation of the NMR parameters for a series of configurations yields a large set of individual (instantaneous) ^{1}H NMR chemical shifts. In contrast to this, experiment measures the *ensemble average* of the ^{1}H NMR chemical shift over all hydrogen nuclei and over a measuring time in the range of microseconds or more. As a consequence, the histograms obtained from instantaneous NMR calculations cannot be measured directly and the global average over ab-initio chemical shift distributions shall be calculated in order to obtain the experimentally accessible resonance line.

Furthermore, it is important to verify that within the comparatively short simulations time of about 20 ps, all relevant relaxation processes have taken place, and that computed statistical averages are accurate. In order to verify this point, the results for different simulation windows out of the trajectories have been compared. Ten momentaneous configurations have been extracted from each of the trajectories pieces between 10-12ps and 19-21ps for diluted acid as well as between 6-8ps and 11-13ps for concentrated ones, and eight snapshots for each of intervals between 10-15ps and 26-31ps for water trajectories. The results show that our statistical averages are sufficiently converged in this respect. All MD simulations and NMR chemical shift calculations have been performed within the CPMD program suite (165; 166).

5.2.3 Proton NMR measurements in HCl solutions

For a direct experimental validation, diluted and concentrated HCl(aq) solutions with c ≈2.6M and c ≈4.9M have been prepared. The solutions were titrated against a high-precision 0.1M NaOH solution in order to determine the exact experimental concentrations, which deviated only insignificantly (±0.07M) from the desired values, as used in the simulations. Liquid-state NMR spectra were recorded on a Bruker DPX spectrometer operating at 250 MHz ^{1}H Larmor frequency. The measured chemical shifts are presented in figure 5.2. The shifts of acidic samples were referenced to the NMR resonance line of pure water, which was measured separately before and after the HCl solutions. In this way, it is ensured that no drift was induced by changes in the shimming of the magnet. The measurements with several samples have been repeated in order to estimate the reproducibility of the results. It has been found that the discrepancies for a given concentration were below 0.1ppm.

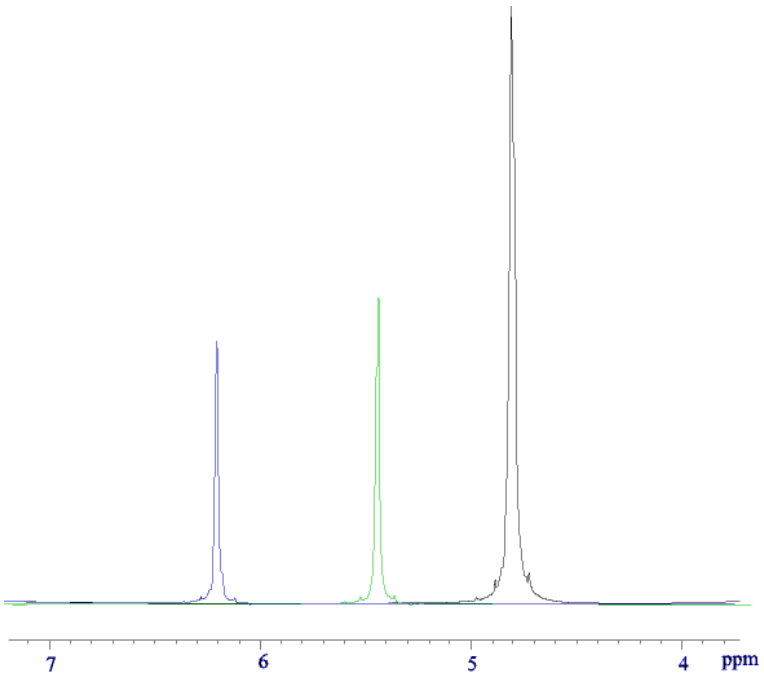

Figure 5.2: Experimental ^{1}H NMR chemical shift spectra for pure water (black) and HCl solutions at two concentrations, $c \approx$2.6M (green) and $c \approx$4.9M (blue). The axis for the chemical shifts is inverted, which is the historically grown convention in NMR spectroscopy.

It is worthwhile mentioning that the linewidth obtained in liquid-state NMR chemical shift measurements is related to many physical effects, such as the imperfect shimming and differently filled NMR tubes. The width of the computed histograms is *not* related to this linewidth, since experimental measurements return only the ensemble average of the contributions of all protons.

A related consequence of this averaging process is that NMR spectroscopy is not able to discriminate between individual instantaneous hydrogen bonds. There is a presently ongoing controversy about the equivalence of the four H-bonds in liquid water (152; 153; 154; 155). While it would be possible to detect inequivalent hydrogen bonds from the calculations, there is no way to verify such conclusions from the experimental side.

5.3 Spectroscopic calculations

5.3.1 Variety of H-bonding in chemical shift distributions

The histograms of instantaneous ^{1}H NMR chemical shift values have been computed for the four liquids systems. For the pure water sample, the resulting distribution is shown in figure 5.3. As mentioned above, the calculated nuclear shieldings are referenced such that the average value of the chemical shifts (marked by a solid line in the distribution) is $\delta(H_2O)$=0ppm. The distribution has a similar shape to the one obtained previously for a different liquid water sample (24). It resembles a slightly non-symmetric Gaussian with a half-width of about 6ppm. This large spread is due to the variety of hydrogen bonding situations in liquid water, ranging from very weak (towards negative δ-values) to very strong (towards positive δ-values). The observed asymmetry in $n(\delta)$ is due to the fact that the H-bonding strength cannot be significantly weaker than that of an isolated molecule (which corresponds to about δ^{H_2O} ≈-6ppm when using our referencing

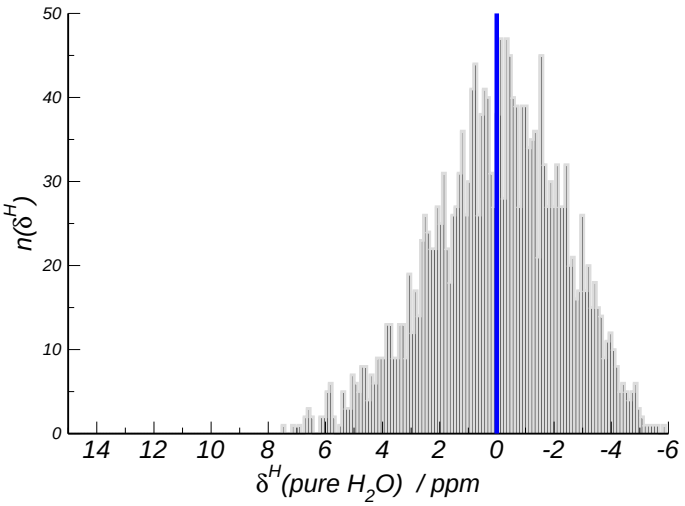

Figure 5.3: Histogram of the computed instantaneous NMR chemical shift values for pure water. The nuclear shieldings are referenced such that the averaged NMR shift, which is shown as a solid line, appears at δ(pure H_2O)=0ppm.

to the shielding of pure liquid water), while there is in principle no limit in the direction of increasing H-bonding strength.

Fast molecular motion in aqueous solutions does not allow experimentalists to detect individual contributions of different hydrogen bonding situations by means of proton NMR measurements. As one can see in figure 5.2 the experimental proton NMR peaks of water and acidic samples are very sharp and represent only an ensemble average over all detected proton shifts within the measuring time. And as it was mentioned before, the broadness of experimental lines *does not* reproduce an existing variety of H-bonding network arrangements, while it becomes clearly visible in calculated chemical shift distributions (figures 5.3 and 5.4). Therefore, the computed proton chemical shift histograms are interesting results, which might give a better insight into microstructure of liquid water and aqueous acidic solutions.

5.3.2 Chemical shift histograms of HCl

The NMR chemical shift histograms of the acidic samples with c(HCl)=2.6M and c(HCl)=4.9M are shown in figure 5.4. As the proton chemical shift distribution for the pure water system 5.3 they demonstrate a wide range of possible H-bonding situations. The computed spectra of acidic solutions have some similar features with the spectrum of liquid water together with very specific ones. While the shape of the acidic distributions around their central peaks is still of Gaussian type, they exhibit a significantly more pronounced tail towards positive δ-values. Their intensity is almost twice as strong for the higher acid concentration.

Here, these tails move the *average* chemical shifts away from the *maximum* of the central peak, which in both acids is still located at the value found for pure water (δ=0ppm, dotted lines). The shift difference between the high concentrated

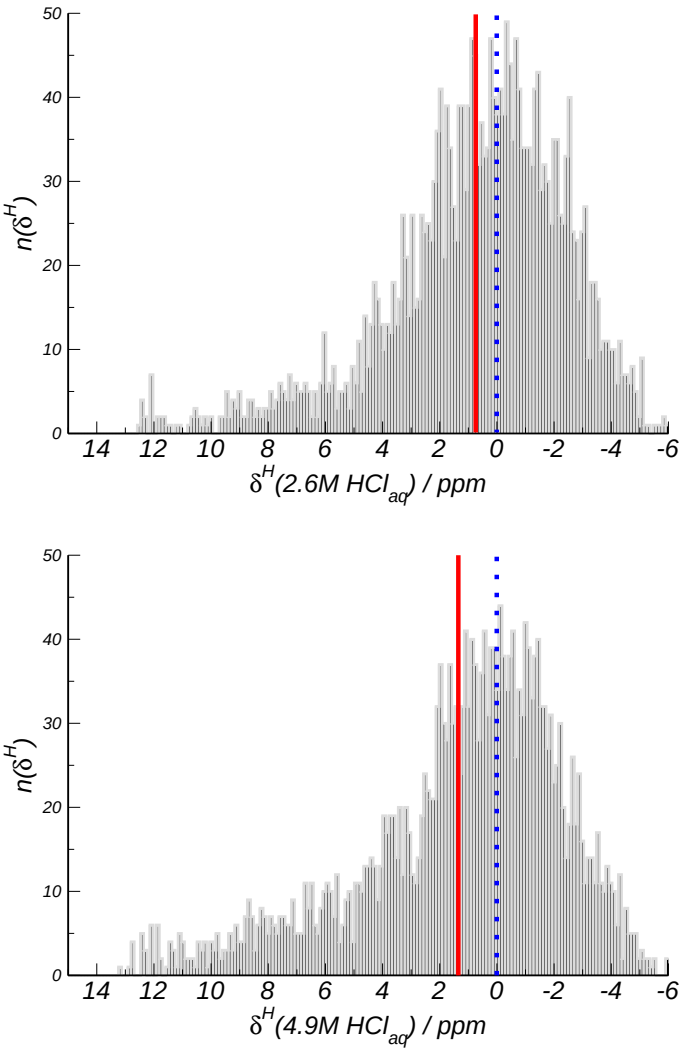

Figure 5.4: Histograms of the computed instantaneous NMR chemical shift values for c=2.6M (up) and c=4.9M (down), referenced to pure water. The averaged NMR resonance lines of the HCl solutions are shown as solid lines, together with the pure water reference (dotted) as a guide for the eye.

acid and pure water turns out to be about twice as large as for the more diluted solution.

In a neutral water system, the observed high-frequency shift values would correspond to very strong hydrogen bonding of the concerned protons. Hence, the question arises which structural features are responsible for these signals. While

it could simply be a consequence of stronger distortions of the H-bonding network due to the solvated ions, it could also be a characteristic NMR resonance from both the protons in the H_3O^+ complexes and those in the direct neighborhood of the Cl^- ions. The fact that the deviation of the average shift appears to have a roughly linear dependency on the HCl concentration is already an indication for the latter assumption. To clarify the origin of the observed chemical shifts distribution, a decomposition of the computed spectra into individual contributions of chosen groups of protons is made. The first solvation shells of chlorine ions, the Eigen and Zundel complexes and the remaining regular water protons are considered. The results are presented in the next section.

5.3.3 ^{1}H NMR signatures of solvated ions

To make a decomposition of the set of obtained proton shifts into contributions from different geometrical classes of configurations, first the chosen classes should be defined. $H_3O^+/H_5O_2^+$ complexes, protons in the first solvation shell of Cl^- ions, and the protons in regular water molecules shall be distinguished. For

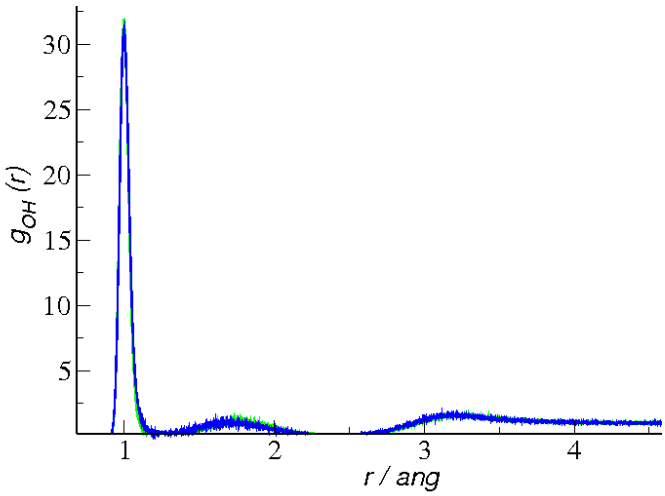

Figure 5.5: O-H radial distribution functions (RDF) for the diluted (green) and concentrated (blue) HCl solutions (47).

this purpose, the geometric criteria derived from the radial distribution functions computed in ref. (47) and shown in figures 5.5 and 5.6 have been used. While the radial distribution functions are a measure for the structure of a liquid, they average out many of the subtle conformational features and therefore cannot be directly used to define hydronium ions. One cannot distinguish between the hydronium cations and regular water protons in figure 5.5. The Eigen/Zundel complexes have been defined via the protonation number of the central oxygen atoms. An Eigen cation was assumed when an oxygen was bonded to three protons with $d_{\text{O-H}} \leq 1.3\mathring{A}$ which corresponds the first maximum in figure 5.5. A Zundel complex corresponds in turn to the case where two (previously detected) Eigen cations share one proton. For different snapshots taken from MD trajectories, the total number of Eigen and Zundel ions was equal to the number of Cl^- anions but with different ratio of $H_3O^+/H_5O_2^+$ complexes. In contrast to the common definition of Eigen complexes ($H_9O_4^+$), the three waters surrounding the central hydronium (H_3O^+) were not included in the averaging of our NMR data, since their hydrogen bonding situation is closer to that of regular water.

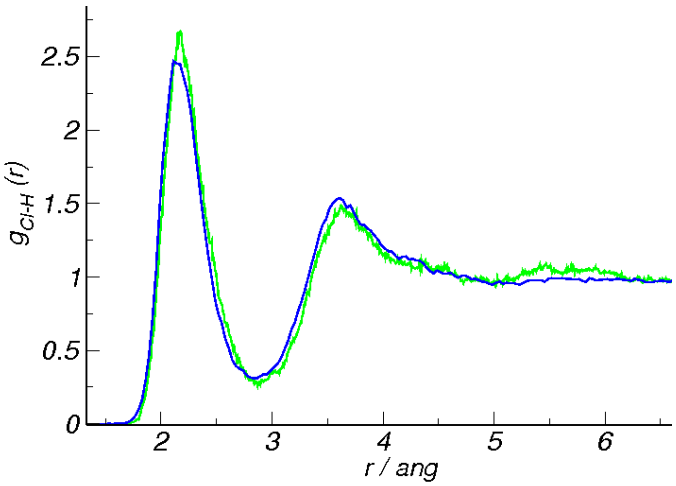

Figure 5.6: Cl-H radial distribution functions (RDF) for the diluted (green) and concentrated (blue) HCl solutions (47).

A proton was considered part of the first solvation shell of a chlorine anion if $d_{\text{Cl-H}} \leq 2.85$ $\mathring{A}$, which corresponds the minimum after the first peak in figure 5.6. Finally, all protons which were neither part of an Eigen/Zundel complexes nor sufficiently close to any Cl^- ion were defined as regular water hydrogens.

The NMR chemical shift contributions corresponding to these different types of geometrical configurations are given in table 5.1 and shown in figure 5.7. An estimation of the actual contributions to the average chemical shift can be obtained by multiplying the spectroscopic signatures given in table 5.1 with the appropriate weighting factors. For example, for the Eigen cations in the c=2.7M solution, this factor would be given by 0.78 x $3H^+$(three protons per H_3O^+) x 3 (three hydronium ions in the solution) / (125 protons in total).

The correlation between the structural arrangement in which a proton is found and the resulting chemical shifts is striking. While the regular water molecules are almost completely unaffected by the presence of the chlorine and hydronium ions, the protons which are part of an Eigen or Zundel cations are high-frequency shifted by about 7.4ppm (H_3O^+) and 5.8ppm ($H_5O_2^+$). The opposite is found for hydrogens in water molecules which solvate the chlorine anions: their computed NMR signal is located at low-frequency values, -0.3/-0.8ppm with respect to

system	regular water	Eigen cations	Zundel complexes	1^{st} Cl^- solv. shell	all protons (comp.)	all protons (exp.)
pure H_2O	0.0	-	-	-	0.0	0.0
single H^+_{aq}	0.0	7.4 (82%)	6.1 (18%)	-	0.2	-
2.7M HCl_{aq}	0.1	7.5 (78%)	5.9 (22%)	-0.8	0.7	0.7
4.9M HCl_{aq}	0.2	7.3 (85%)	5.6 (15%)	-0.3	1.3	1.4

Table 5.1: Individual ^{1}H NMR chemical shift signatures of the protons in Eigen-/Zundel-complexes, in the first solvation shells of the Cl^- ions, and in the regular water molecules. The relative probabilities for finding a solvated H^+ as an Eigen or Zundel cation are given in parenthesis. The total average and the corresponding experimental values are also shown.

regular water.

Qualitatively, this trend can be explained via electron density considerations. In a hydronium ion, the water electrons are shared by three protons, so that with respect to neutral water, there is less electronic density available per hydrogen. The same – to a lesser extent – is the case for a Zundel complex. In contrast to this, the hydrogens in a chlorine solvation shell point into a large electron cloud. In addition, this cloud is somewhat more delocalized than the lone pairs of a water oxygen, due to the negative charge of the chlorine. This results in a stronger shielding of the proton spin, and hence a more negative shift than for a normal proton that is H-bonded to a water oxygen.

Interestingly, the chemical shifts of these complexes depend only little on the total concentration of ions. This can be observed also in figure 5.7; the protons in Eigen cations have almost the same shift for a single solvated H^+ as for the strongly concentrated acid. For the Zundel complexes, the situation is similar; the small change of 0.2-0.3ppm between the protonated water and diluted and concentrated acids can be explained by the decreased amount of water molecules which are available for building the solvation shells. The same tendency towards smaller absolute shifts is seen for protons in the chlorine solvation shells; they also approach the shift of regular water (0.0ppm).

This data explains the histograms shown in figure 5.4: the maximum of the distribution, which corresponds to protons from regular water molecules, is essentially unmodified by the addition of the acid; the high-frequency tails in the region around 5-8ppm are exclusively due to the solvated H^+ cations, see figure 5.7. Both the hydronium cations and protons from the first solvation shells of Cl^- anions have a broad chemical shift distributions, especially in case of Eigen/Zundel complexes. That corresponds to a wide range of possible solvation situations for these ions, the most evident of them, such as a bridging the ions

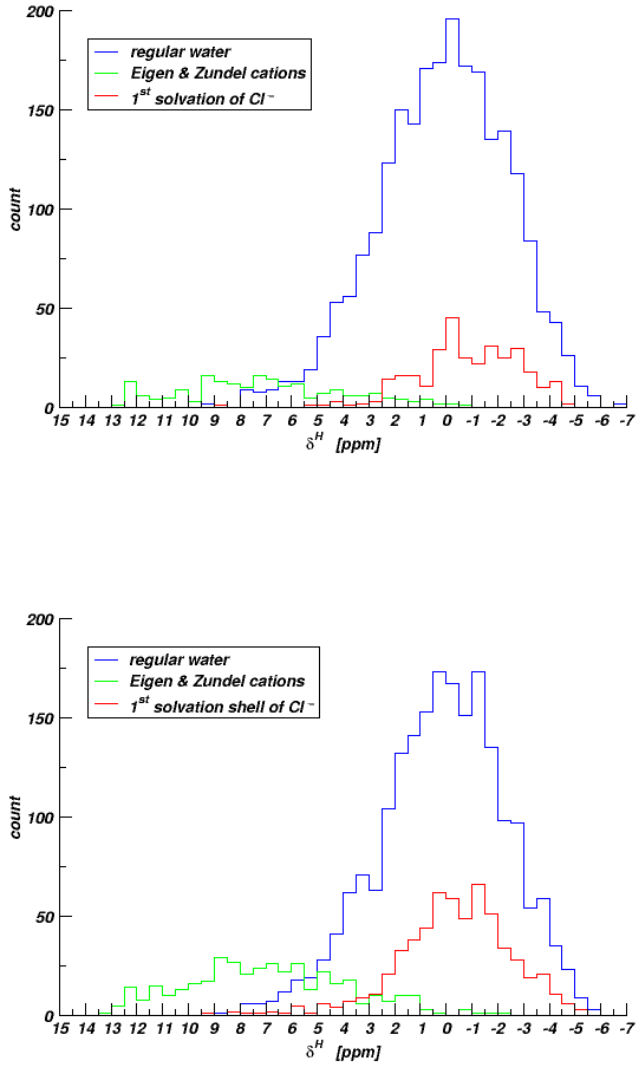

Figure 5.7: Decomposition of the chemical shift contributions from different geometrical classes of configurations (as mentioned in the text and table 5.1) to the histograms in figure 5.4, for c=2.6M (up) and c=4.9M (down).

by one or two water molecules or a presence of contact-ion pairs might be also resolved in radial distribution functions (47). Since the protons which solvate the Cl^- yield an NMR signal very close to that of regular water, their contributions are not clearly visible in the histograms. When using a better statistics, the NMR

signatures of those protons would possibly appear as a low-frequency-shoulder in the shift distributions. However, with the data available from the present calculations, this effect can only be seen in the decomposition of the shifts.

5.3.4 Chemical shift dependence on acid concentration

Finally, the comparison of the averaged NMR shifts from the ab-initio calculations with the measured liquid-state ^{1}H NMR spectra of the HCl acids at the two concentrations is presented in figure 5.8. As for the calculated shifts, the experimental values have been referenced to pure liquid water. The agreement is essentially perfect for the low concentration and very good for the sample at 4.9M. While the agreement at c_{HCl}=2.6M is probably fortuitous, the accuracy at the higher concentrated acid is in line with previous ab-initio calculations in similar systems (19; 23; 24; 167; 168). The numerical overall accuracy allows for an estimated error bar of ∼0.3ppm, due to the deficiencies of density functional theory in describing hydrogen bonds, the use of the pseudopotential approxima-

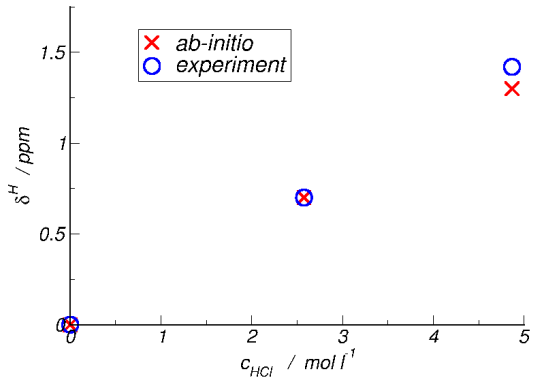

Figure 5.8: Dependence of the experimental and calculated NMR chemical shifts on the HCl concentration. In all cases, the actual concentrations (as obtained from titration, and computed in the simulation parameters, respectively) are used.

tion, and the incomplete basis set. Here the profit from error cancellations for chemical shift calculations is also taken into account according the argumentation given in section 4.3. Further minor approximations are the finite size of our computational water box, the thermodynamical equilibration of the Car-Parrinello simulations; however, they have only a neglegible impact on our results. The very good agreement also provides support that, despite these computational issues, the description of disordered and highly fluctuating liquids and solutions by means of Car-Parrinello molecular dynamics simulations as well as the ensemble averages of spectroscopic parameters based on them do give a realistic picture of microscopic structure of complex solutions.

5.4 Conclusions

In this chapter, a first principles analysis of the ^{1}H NMR chemical shift distributions and spectra of aqueous HCl at two concentrations is presented, accompanied by the corresponding measured NMR resonance lines. The agreement between experiment and the calculations is very good, giving a confidence that the underlying Car-Parrinello molecular dynamics simulations are well equilibrated and give a representative description of the acidic solutions. Both the trajectory generation and the determination of the NMR parameters is done under periodic boundary conditions, at consistent consideration of the spatial and temporal fluctuations in the atomic structure and hydrogen bonding network of the liquids.

A variety of H-bonding network arrangements in liquid water and acidic solutions is revealed by means of computed proton chemical shift histograms. The specific features of solvated hydronium cations and chlorine anions as well as dependence on HCl concentration are clearly visible in chemical shift distributions of acidic samples. While the shape of the acidic distributions around their central

peaks is still of Gaussian type like for liquid water, they exhibit a significantly more pronounced tail towards positive δ-values. Their intensity is almost twice as strong for the higher acid concentration.

Finally, the structural origins of the observed chemical shift trends are investigated in terms of Eigen and Zundel cations, the first chlorine solvation shell, and the remaining regular water molecules. This data reveals in unprecedented detail the correlation between microscopic configurations and resulting chemical shifts in this class of systems, giving access to structure-property relationships which are difficult to obtain from experiment alone. It is shown that the contributions of Eigen and Zundel ions, regular water molecules and the chlorine solvation shell to the ^{1}H NMR resonance line are actually very distinct and almost independent of the acid concentration.

Chapter 6

Proton conducting materials based on phosphonic acid derivatives

6.1 Motivation

The growing necessity for clean energy sources to substitute fossil energy has created high demands for battery and fuel cells. Among various fuel cell technologies, proton exchange membrane fuel cells (PEMFC, see figure 6.1) have emerged as one of the most promising power sources for portable electronics and transportation applications . Since the first development of Nafion by DuPont in the 1960s, the state of art technology has been the use of perfluorinated polymers with sulfonic acid sidechains as proton conducting membranes in PEMFC (169). The conductivity of Nafion-type membranes is highly dependent on the water content, which is loosely bound to the sulfonic acid moieties. The difficulty in maintaining a high level of hydration above the boiling temperature of water limits the operating temperature of PEMFC to 80°C. At this low temperature, CO poisoning

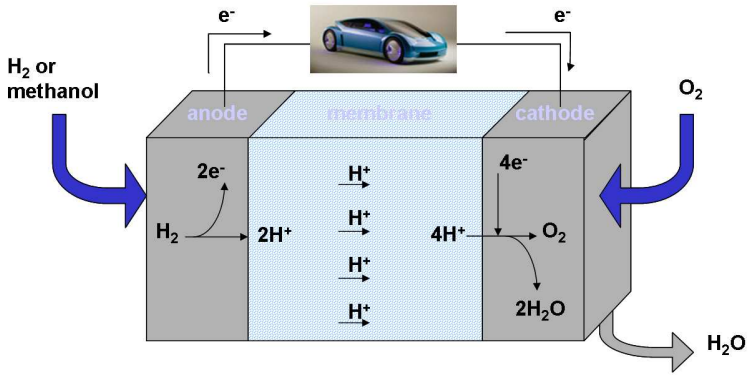

Figure 6.1: Schematic diagram of a proton exchange membrane fuel cell (PEMFC) .

of the electrode damages the catalyst and reduces the performance of the fuel cells. In order to avoid CO poisoning, highly pure hydrogen as fuel gas and noble metals as electrode material are required, which are not cost-effective. However, at high operating temperature, CO poisoning is reduced due to the increased activity of the catalyst. Therefore, various approaches have been proposed, aiming at developing new classes of proton conducting membranes for high temperature PEMFC. Replacing water with heterocyclic protonic solvent such as imidazole, pyrazole and benzimidazole has been proposed (170; 171). Organic-inorganic hybrid materials have shown enhanced stability at high temperature with high conductivity (172). Recently, cross linking between polymer chains containing sulfonic acid was reported to provide proton conductivity three times as high as Nafion and to enhance the mechanical stability (173). Another approach towards high temperature PEMFC is substituting the SO_3H acidic group by different protogenic groups. Polymer membranes containing phosphonic acid groups are one of the promising candidates. High conductivity has been observed for fused H_3PO_4 and proton transfer along the hydrogen bonded network has been shown as a major conduction mechanism (174; 175). Therefore, research has focused on developing new materials merging the high proton conductivity of phosphonic

acid and the mechanical strength of polymers and/or inorganic fillers.

There are two important mechanisms which govern the proton transport in the proton conducting membrane, one involving structural diffusion known as Grotthus mechanism and the other involving a vehicle-style migration (65; 66). In the Grotthus mechanism, proton transfer occurs between phosphonic acid groups and through reorganization of hydrogen bonds. In the vehicle mechanism, the proton is transported with the aid of carriers such as water in the form of H_3O^+.

In this project, poly(vinyl phosphonic acid) was chosen as a model system to study the local structure and the proton conducting mechanism in phosphonic acid tethered polymers, since it contains a high concentration of acid groups and adopts a simple structure. Phosphonic acid is considered to form a strong hydrogen bonding network involving both P=O and P-OH as proton acceptor and proton donor group. The chemical structure of poly(vinyl phosphonic acid) including a possible hydrogen bond chain is shown in figure 6.2. Poly(vinyl phosphonic acid) will be denoted as PVPA throughout the text.

Knowledge concerning the chemical environment and the proton motion is crucial to understanding the conduction mechanism of proton conducting materials. Solid state NMR spectroscopy is a powerful tool for probing the local structural properties and proton mobility of the new proton conducting polymer. Complementary to the experiments, quantum chemical simulations can be used to investigate local structure and dynamics of the proton conducting membrane. Force field molecular dynamics simulations together with coarse-grained polymer models could give insight into the global dynamics and morphology of this complex partlially amorphous and partially higher ordered superstructure. However, this work is focused on the description of *local* features, such as the hydrogen bonding network and chemical defects of the polymer, and the calculations of their spectroscopic signatures.

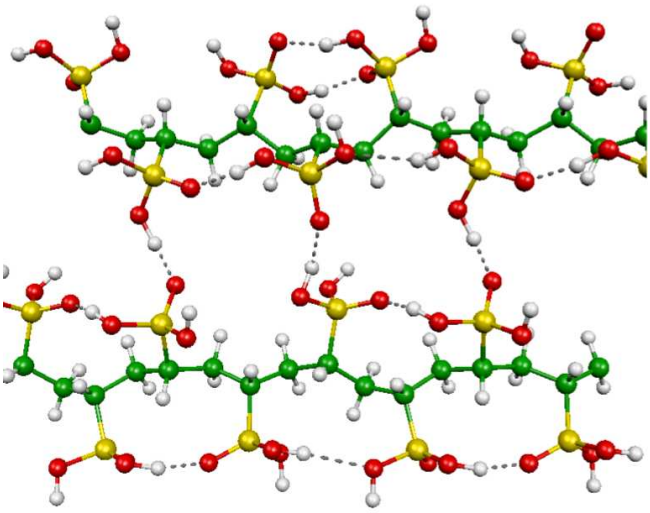

Figure 6.2: Illustration of a possible H-bonding network of polyvinyl phosphonic acid (PVPA) chains, where Grotthus-like proton transfer could take place between the phosphonic acid groups, followed by reorientation of their hydrogen bonds.

Hydrogen bonding between acidic groups is the most plausible candidate for the short-range proton transfer, which will in turn lead to a percolation phenomenon and long-range proton conduction. An influence of possible defects in the polymer on proton conduction, as well as their spectroscopic properties can also be obtained from first principles calculations.

Ab-initio molecular dynamics simulations provide structural propositions of the PVPA hydrogen bonding network, which are used to calculate ^{1}H chemical shift signatures of regular POH groups as well as neutral and negatively charged anhydride defects. The MD simulations reveal that the negative charge defects are trapped by anhydride groups and hence the new peak appearing in experimental proton NMR spectra at lower temperature can be assigned to a combination of these defects. It is found that both type of defects demonstrate the same temperature dependence trend: increase of chemical shift with decreasing temperature, which is consistent with experiment. The computed high frequency shift of 4-

5 ppm between the anhydrides and regular POH protons is also in agreement with experimental observations. In addition, the effect of chemical defects on ^{31}P NMR spectra is also calculated.

6.2 Models and computational methods

Two systems were investigated: crystalline methylenediphosphonic acid (MDPA) whose structure is known from x-ray diffraction (176) and poly(vinyl phosphonic acid) (PVPA) – complex partially amorphous, partially higher ordered polymer. In spite of the difference of the two materials in long-range order, the local structure of PVPA obtained by molecular dynamics simulations and presented in figure 6.5 is similar to that of MDPA based on crystallographic data, as shown in figure 6.3. Therefore, one can assume a similar local arrangement of hydrogen bonding between acidic groups. For MDPA, spectroscopic experimental data are also available in the literature (177), providing an opportunity to compare the computed proton chemical shifts with experimental spectra and to verify a feasibility of the ab-initio DFT approach. In addition, the systematic error in computed chemical shifts obtained for MDPA can be used in the PVPA spectroscopic calculations to estimate the error resulted from the deficiencies of DFT method, since the same computational setup is employed for the both crystalline and polymer phosphonic acid derivatives.

On all the considered systems, MDPA and different modifications of PVPA, molecular dynamics (MD) simulations of at least 2 ps duration were done in order to locally relax the hydrogen bond network of our configurations and to perform a certain sampling of the available phase space regarding structural disorder. For the fictitious electronic mass in the Car-Parrinello Lagrangian, a value of 700 a.u. was chosen, corresponding a timestep of 6.0 a.u. (0.145 fs).

NMR chemical shifts were computed on a subset of configurations extracted from the molecular dynamics trajectories, fully taking into account the periodic boundary conditions of the model systems (113). Typically ten randomly chosen snapshots were sampled for each system, which allowed the determination of semi-quantitative differences in the NMR signatures of different conformations. The computed nuclear shieldings were referenced to TMS shielding values which were calculated using the same computational setup.

For all MD and NMR calculations, the program package CPMD (165) was used, a plane wave pseudopotential code based on density functional theory. All calculations were done with the gradient-corrected exchange-correlation functional proposed by Becke (91) and Lee, Yang, and Parr (BLYP) (92) and norm-conserving Goedecker-type pseudopotentials (96; 158), together with an energy plane wave cutoff of 70 Ry.

6.2.1 Calculations on a structurally well-defined model system

Molecular dynamics simulations for crystalline methylenediphosphonic acid (MDPA) were performed at temperature T=273K corresponding to the experimental conditions. Crystallographic data of MDPA was taken from the Cambridge Structural Database, and the atoms were relaxed within the computational setup described above, keeping the crystal lattice fixed at the experimentally defined values.

The atomic coordinates of heavy (non-hydrogen) atoms did not change significantly, as expected, confirming the X-ray based structural data. The computed chemical shifts of the acidic protons (9.6 ppm and 11.7 ppm) deviate by about 0.2-0.7 ppm from the corresponding experimental values (10.3 ppm and

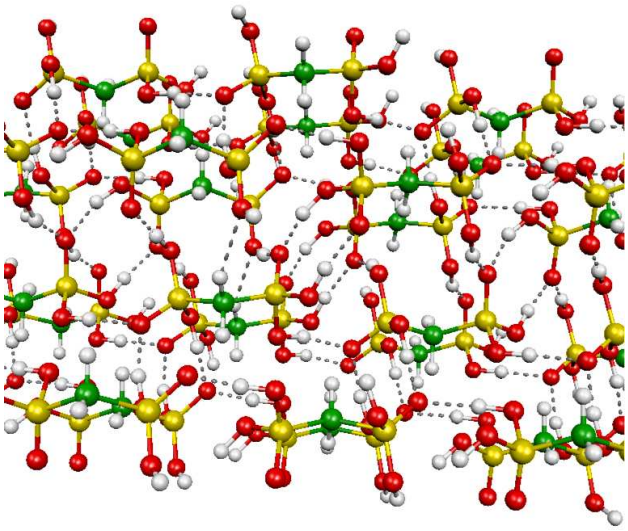

Figure 6.3: The geometry of crystalline methylenediphosphonic acid (MDPA) based on the crystallographic data from Cambrige Structural Database (176). Several periodically replicated unit cells are shown.

11.9 ppm) (177). This difference in absolute values of chemical shifts, which is typical for this kind of calculations, is mainly due to the deficiencies of density functional theory in describing hydrogen bonds, the use of the pseudopotential approximation, the incomplete basis set, and temperature effects (21; 178).

6.2.2 Design of a model for disordered polymeric system: PVPA

For the quantum-chemical analysis of poly(vinyl phosphonic acid) (PVPA), a simplified model system under periodic boundary conditions was designed, since no X-ray crystallographic structure of PVPA is available due to the lack of crystallinity. The creation of the model system was done in several steps. First, two linear (syndiotactic) PVPA polymers with a periodicity of 10.25 A, corresponding to two chains of four independent PVPA repeating units per unit cell, were build. According experimental data obtained by NMR spectroscopy (71), the

acidic groups should have a separation of about 5 $\AA$ from neighboring groups. In this model the average distance between acidic groups is 4.9 $\AA$. The lattice constants for the two directions orthogonal to the polymer axis were fixed at 8.5 $\AA$ and 19 $\AA$, respectively, in order to accommodate an appropriate amount of space between two polymer chains and their periodic images. In this way, it was attempted to let the two PVPA polymers arrange themselves in a hydrogen bonding structure suitable for them, while leaving enough degrees of freedom to allow for structural relaxation. Under the constraints imposed by the periodic lattice, hydrogen bonding is still possible between the two polymer chains, but not with their periodic images, see figure 6.4.

Within the chosen constraints, a series of Car-Parrinello (CP) Molecular Dynamics (MD) simulations was performed to find energetically favorable structural arrangements, in particular regarding the distances between two PVPA chains within the unit cell. For several initial conformations, the system relaxed to

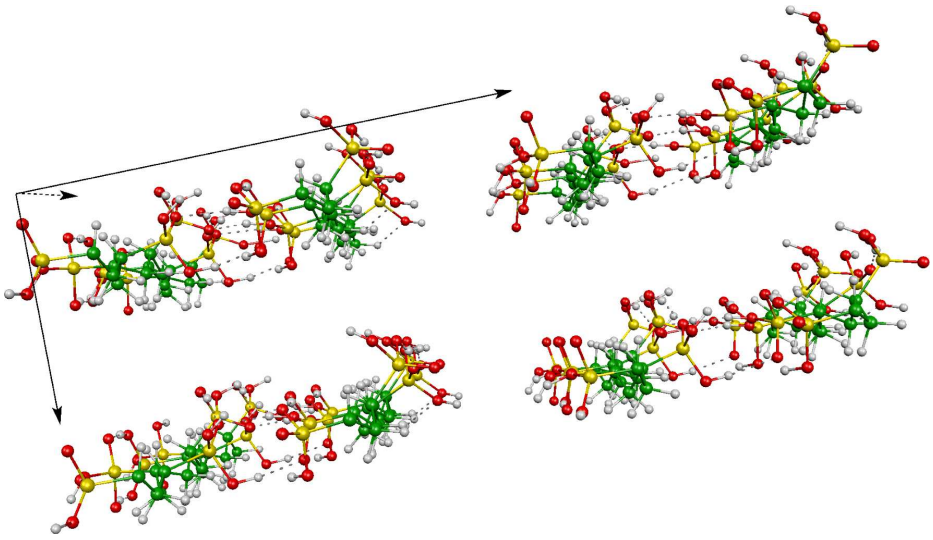

Figure 6.4: Geometric setup for a H-bonding network between an isolated pair of infinite PVPA chains. The lattice constants were chosen such that no H-bonding between the periodic images of the PVPA chains was possible.

inter-chain distances of about 8.3-8.5 $\mathring{A}$, which appears to be close to the energy optimal one.

All further MD simulations were performed with an adapted periodic supercell of volume V=10.25x8.5x16.5 $\mathring{A}^3$, such that the previously obtained spacing for the parallel polyvinyl chains (with 8.3-8.5 $\mathring{A}$ periodicity) was reproduced. This setup actually created a closed two-dimensional sheet of the periodic PVPA chains, separated by several angstroms of vacuum, see figure 6.5.

The designed model must clearly be seen as a considerable simplification of the true material, which is far more complex. However, no attempt was made to represent a full realistic picture of the partially amorphous and partially more ordered superstructure, and no statistical description of other polymer characteristics (such as the tacticity and the topology of the polymer backbone) was initiated. While such a modeling is in principle feasible by means of coarse-grained molecular dynamics simulations (179; 180; 181; 182), it exceeds the scope of the

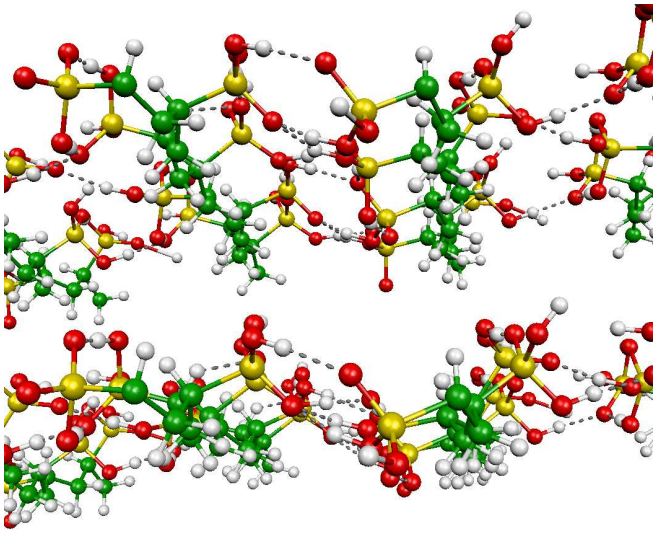

Figure 6.5: Geometric setup for a fully saturated H-bonding network. The lattice constants were taken from the equilibrium average distances obtained for the isolated pair of PVPA chains (see figure 6.4).

present investigation by far. In the present work, the focus lies on the description of local features, such as the hydrogen bonding network and chemical defects in the polymer, and the calculation of their spectroscopic signatures. Since NMR is a tool that probes only local ordering, this model should be in principle capable of representing the interplay of the H-bond network and steric effects, to a degree that allows us to give semi-quantitative predictions of the NMR resonance of particular local conformations (183) .

In this work, molecular dynamics simulations and spectroscopic NMR calculations for three polymer modifications were made: PVPA with regular POH groups, with anhydride defect (resulting from the condensation of two phosphonic acid groups) and with negatively charged (deprotonated) acidic group. Pictograms of the considered chemical defects are given in figure 6.6. The calculations were performed both at T=200 K and T=300 K in order to estimate a possible temperature effect on the structural properties and the chemical shift spectra. On the basis of the obtained CP trajectories, the calculations of the NMR chemical shifts were done according to the procedure described in 6.2. The same computational setup for all systems was used, in order to provide a consistent description for all considered PVPA modifications.

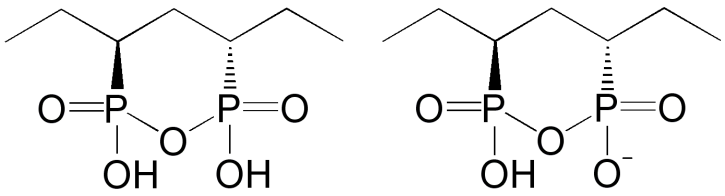

Figure 6.6: Pictogram of the neutral anhydride (left) and negatively charged anhydride (right) polymer defects.

6.3 PVPA: structural results

In order to gain a better understanding of the proton conduction mechanism, it is crucial to know details of how phosphonic acid groups interact with their neighbors by means of a hydrogen bonding network. The short-range proton transfer will most likely proceed through this H-bonding network, leading to a percolation phenomenon and eventually long-range proton conduction. In this context, ab-initio molecular dynamics simulations were performed to find possible local H-bonding arrangements of regular PVPA, as well as possible configurations of anhydrides and negatively charged (i.e. deprotonated) POH groups.

First, the MD simulations of perfect PVPA without defects were done. The computed hydrogen bonding network of this system is shown in figure 6.5. The presence of the hydrogen bonds between the neighboring phosphonic acids along the chain (intra-chain H-bonds) and between phosphonic acids residing on the different polymer chains (inter-chain H-bonds) is clearly seen there.

Furthermore, a series of MD simulations were carried out on the system with anhydride species (see the geometry of PVPA with neutral anhydride in figure 6.7). To investigate an acidic dissociation, a proton was removed from a regular P-OH group (leaving a charged P-OH) in a system containing neutral anhydride. During the subsequent MD simulations, the anhydride was immediately deprotonated, yielding one of its protons to the original proton vacancy. The charge defect remained at this anhydride during the rest of the MD run. This indicates that neutral anhydride groups could attract and keep negative charge defects.

Thus, the anhydride defects (resulting from the condensation of two phosphonic acid groups) may inhibit proton conduction in two ways, first via reducing the number of available OH groups, and secondly by immobilizing proton vacan-

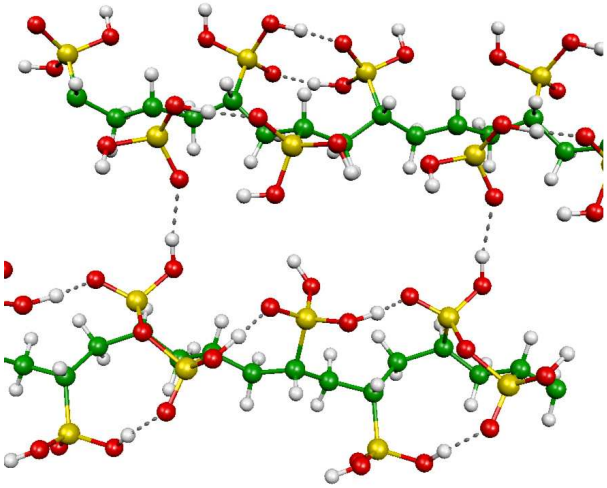

Figure 6.7: Geometric setup for PVPA with an anhydride defect (bottom chain). More than one unit cell are shown.

cies, which may occur in PVPA by spontaneous dissociation of phosphonic acid. A possible reason for this trapping effect is that in an anhydride, the negative charge can delocalize over two phosphonic acid groups instead of one. Also the anhydride species are less mobile than regular POH groups.

6.4 PVPA: chemical shift calculations

Using density functional theory methods described in detail in section 3.3, the instantaneous proton NMR chemical shifts have been calculated for the PVPA polymer with and without chemical defects at two different temperatures. Regular phosphonic acidic groups, backbone protons, neutral and deprotonated anhydride defects have been considered and their individual spectroscopic contributions in computed NMR spectra were calculated.

6.4.1 Proton NMR chemical shift of regular acidic groups

The ab-initio proton NMR signatures for regular PVPA are given in table 6.1 Corresponding experimental values are taken from the ^{1}H NMR spectrum (71) shown in figure 6.8. Some features are clearly visible from presented data.

The computed proton NMR chemical shift of backbone protons (1.6ppm) is lower than experimental one (2.3ppm) (71) by 0.7ppm. No dependence on temperature is observed in the both computed chemical shifts of the backbone and acidic protons, which is consistent with experimental results (71).

For the backbone protons the low-frequency off-set in chemical shifts is within the error bars estimated in section 6.2.1. However, ab-initio NMR calculations yield the chemical shifts of 8.4ppm for the phosphonic acid groups, which is about 2ppm smaller than the experimental peak of 10.6ppm. This additional discrepancy of about 1.5ppm is probably due to the incomplete H-bonding structure of the PVPA system in the created periodic model system. Furthermore, this periodic model neglects all the disorder in the spatial topology of the polymer backbone. In the real system, this disorder yields more strain in the covalent bonds, as well as a broader distribution of hydrogen bonding conformations. While these calculations therefore cannot be interpreted as quantitative predictions, they are indeed supposed to indicate trends and the magnitude of the effect of structural and charge defects on NMR spectroscopic parameters.

	T	regular POH	backbone
comp	200K	8.4	1.6
comp	300K	8.4	1.6
exp (71)	300K	10.6	2.3

Table 6.1: Individual ^{1}H NMR chemical shift signatures (in ppm) of the acidic and backbone protons in case of regular PVPA.

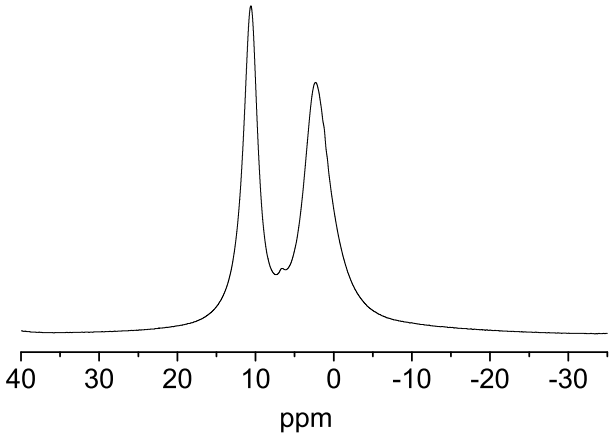

Figure 6.8: ^{1}H MAS NMR spectra of regular PVPA acquired at room temperature with spinning frequencies of 30 kHz (71).

6.4.2 Proton NMR signatures of polymer defects

To investigate the role of "condensation" in the PVPA polymer, both neutral and negatively charged anhydride defects have been considered, since the performed MD simulations have shown that the proton vacancies are trapped by the anhydrides. In case of the deprotonated anhydride three protons were assumed to be a part of the defect: the remaining proton left on the anhydride and two protons from neighboring regular acidic groups strongly hydrogen-bonded with delocalized negative charge on the proton vacancy.

The NMR chemical shift contributions of regular acidic protons and anhydride defects are given in table 6.2.

Two general features can be extracted from these ab-initio NMR chemical shift calculations. First, the protons of an anhydride have a NMR chemical shift of 12ppm, significantly higher than those of regular POHs. Secondly, the presence

system	regular P-OH	protons of anhydride
PVPA without defects	8.4	n/a
PVPA with anhydride	8.6	12.0
PVPA with neg. charged anhydride	9.6	13.5
exp (71)	10.6	14-16

Table 6.2: ^{1}H NMR signatures (in ppm) of protons from regular acidic groups and from neutral and charged anhydride defects.

of a negative charge on the anhydride enhances this effect, leading to a proton NMR signal around 13.5ppm. The increase in the chemical shifts of the regular POH groups in the charged system is probably a parasitic effect occurred due to the finite size of used simulation model and therefore not relevant for macroscopic PVPA.

The computed high frequency shift of 4-5 ppm between the anhydrides and regular POH protons is in agreement with experimental observations (71). Thus, the new peak appearing in ^{1}H MAS NMR experimental spectra at lower temperature (71) can be assigned to a combination of these defects.

6.4.3 Temperature dependence of anhydride chemical shift

Furthermore, the temperature dependence of the ^{1}H NMR chemical shifts was investigated by repeating the molecular dynamics simulations at T = 300 K. The results of NMR sampling of the trajectories obtained at this higher temperature are shown in table 6.3.

The ab-initio chemical shift calculations show a change in the NMR resonances of the anhydride protons towards low-frequencies, by about 1ppm (for 100 K temperature change). This increase in shielding corresponds to a weakening of the hydrogen bonding network around the defect, which is not unexpected. However, the regular P-OH hydrogen bonding network appears to be unaffected, since no

system	T, K	defect	regular POH
PVPA without defects	200 K	n/a	8.4
	300 K	n/a	8.4
PVPA with anhydride defect	200 K	12.0	8.6
	300 K	10.7	8.3
PVPA with neg. charged anhydride	200 K	13.5	9.6
	300 K	12.5	9.6

Table 6.3: Temperature dependence of computed proton NMR signatures (in ppm) of regular acidic groups and defects.

significant difference between T = 200 K and T =300 K could be seen in their calculated NMR lines.

The computed temperature trends of anhydride defects are in agreement with experimental observations (71) shown in figure 6.9, where the ^{1}H MAS NMR spectra of PVPA acquired below room temperature reveal more pronounced high-frequency shoulder at lower temperature.

According to experimental data (71), PVPA annealed at T=150° C contains normal phosphonic acid and anhydride defects in a ratio of 1:1, as determined by deconvolution of ^{31}P MAS NMR spectrum and this will give rise to ^{1}H NMR signal of normal and anhydride acid with intensity ratio of 2:1. However, the intensity of the measured high-frequency ^{1}H MAS NMR signal was smaller than predicted. Therefore, the origin of this high-frequency peak cannot be explained only by means of neutral anhydrides. Charged anhydrides show a stronger shift towards high-frequencies in computed NMR resonance and lesser concentration in the polymer. Thus, the additional high-frequency signal resulting in experimental proton spectra at 14-16ppm is believed to be most likely from the deprotonated anhydride defects. Even though the full dissociation of the acidic protons in PVPA is certainly hindered in a solid state sample, the remaining water content is most probably sufficient to allow a partial spontaneous dissociation. This may

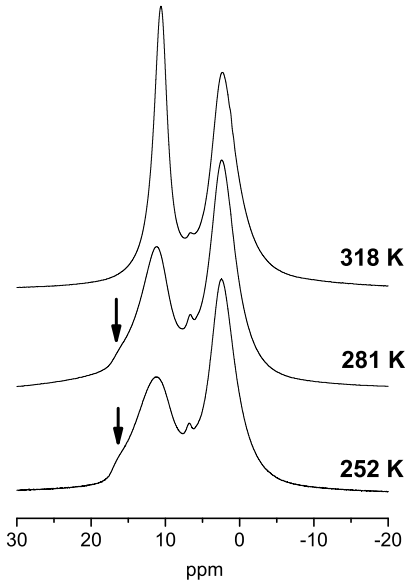

Figure 6.9: ^{1}H MAS NMR spectra of PVPA acquired below room temperature (71).

lead to full deprotonation of acid anhydride above room temperature, which can explain the disappearance of the high frequency signal above room temperature.

6.4.4 Effect of H-bonding on phosphorous NMR

To estimate the dependence of ^{31}P NMR chemical shift on changes in the spatial arrangement of the protons and their H-bonding network, the ab-initio NMR chemical shift calculations were performed on three small fragments of PVPA chains shown in figure 6.10, which represent regular PVPA structure and two possible geometries of "condensation" defects.

The geometries of these three systems were optimized under the density functional theory (DFT) approach using the B3LYP exchange-correlation functional (92; 184) with a 6-31G(p) basis set. The NMR chemical shifts were ob-

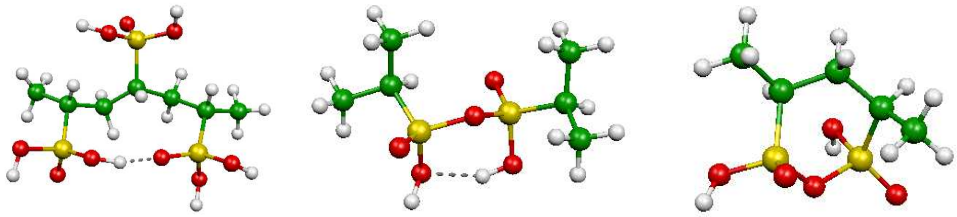

Figure 6.10: Geometries of isolated model systems used to calculate the effect of polymer defects on ^{31}P NMR spectra. No defect (left), PVPA with inter-chain-anhydride defect (middle) and intra-chain-anhydride polymer defect (right).

tained under the same computational setup but with a 6-31+G(d,p) basis set, using the GIAO method for achieving gauge invariance (185). All calculations were done with the Gaussian03 package (186).

Furthermore, the influence of a proton vacancy on regular and condensated P-OH groups on the ^{31}P shifts was investigated. A summary of the results is presented in table 6.4. The chemical shifts were obtained by the reference of the computed nuclear shieldings to the average value of regular PVPA. Several features could be extracted from these ab-initio NMR chemical shift calculations.

An influence of anhydride defect is clearly seen from the presented data. Condensation of neighboring phosphonic acid groups leads to the low-frequency shift

system	charge	chemical shift, ppm
PVPA without defects	neutral	0
	deprotonated	-18.2
inter-chain anhydride defect	neutral	-6.6
	deprotonated	-22.1
intra-chain anhydride defect	neutral	-14.3
	deprotonated	-19.4

Table 6.4: ^{31}P chemical shift signatures computed for three fragments of PVPA chains shown in figure 6.10, which represent regular PVPA structure as well as inter-chain and intra-chain anhydride defects.

in computed ^{31}P NMR signatures, by 6.6 ppm for inter-chain defect geometry and 14.3 ppm for intra-chain defect (see figure 6.10). Thus, ab-initio phosphorous NMR calculations give an opportunity to distinguish between regular and condensated acidic groups and also to identify possible geometries of the anhydride defect.

A deprotonation of P-OH group results in the low-frequency shift by about 18ppm for regular structure and by 15.5ppm and 5ppm for the anhydrides. For the latter, the deprotonation effect is three times weaker for the intra-chain condensation, since no H-bonding between phosphorous atoms on the anhydride is possible in this case. The difference in computed ^{31}P chemical shifts between regular P-OH groups and anhydrides is significantly higher for the deprotonated defects (19-22ppm vs. 7-14ppm for the neutral ones). Hence, the performed calculations give a possibility to distinguish between negatively charged and neutral anhydrides.

Based on the ab-initio phosphorous NMR chemical shift calculations, one might expect an additional signal at $\sim$20ppm in ^{31}P NMR experimental spectra of PVPA polymer at low temperatures due to the presence of the deprotonated anhydride defects. So far, however, this is not confirmed by supporting experiments, since the broadening of NMR spectra at low temperature obscures discrete resonances.

6.5 Conclusions

In this chapter, a first principles analysis of a new proton conducting polymer for fuel cell applications: poly(vinyl phosphonic acid) is reported. Three modifications of the polymer: PVPA with regular POH groups, with anhydride defect (resulting from the "condensation" of two phosphonic acid groups) and with neg-

atively charged (deprotonated) acidic group are investigated. The focus of this work is on the description of *local* features, such as the hydrogen bonding network and chemical defects of the polymer, and the calculations of their spectroscopic signatures.

Ab-initio MD simulations are performed to find possible local H-bonding arrangements of regular PVPA, as well as possible configurations of anhydrides and deprotonated POH groups. They reveal that proton vacancies are attracted and trapped by the anhydride defects. A possible reason for this trapping effect is that in an anhydride, the negative charge can be delocalized over two phosphonic acid groups instead of one. Also the anhydrite species are less mobile than regular POH groups. This finding indicates that condensation defects may inhibit proton conduction in two ways, first via reducing the number of available OH groups, and secondly by immobilizing proton vacancies, which may occur in PVPA by spontaneous dissociation of phosphonic acid.

On the basis of the obtained CP trajectories, the calculations of the proton NMR chemical shift signatures of neutral and deprotonated anhydride defects as well as regular POH groups are carried out. First, it is found that the protons of an anhydride have a significantly higher NMR chemical shift than those of regular POHs. Secondly, it is shown that the presence of a negative charge on the anhydride enhances this effect, leading to a high frequency shift of 4-5 ppm between the anhydrides and regular POH protons. Therefore, the new peak appearing in experimental proton NMR spectra at lower temperature is assigned to a combination of neutral and charged anhydride defects.

In order to estimate a possible temperature effect on the structural properties and the chemical shift spectra, the MD simulations and spectroscopic NMR calculations at T=200K and T=300K are performed. It is found that the hydrogen bonding network of the polymer backbone and regular POH groups appears to

be unaffected, since no significant difference between the two temperatures could be seen in their calculated NMR lines. In opposite to this, both type of considered defects demonstrate the same temperature dependence trend: increase of chemical shift with decreasing temperature, which indicates the strengthening of the hydrogen bonding network around the defect. The computed temperature trends are consistent with experimental observations.

Finally, a dependence of phosphorous NMR chemical shifts on changes in the spatial arrangement of the protons and their H-bonding network is investigated. The ab-initio ^{31}P NMR chemical shift signatures are computed for three small fragments of PVPA chains, which represent regular PVPA structure and anhydride defects. From these calculations, the influence of the dissociation effect on the phosphorous chemical shifts is determined. It is found that the condensation of neighboring phosphonic groups for both intra- and inter-chain geometries leads to a noticeable increase in the ^{31}P nuclear shieldings. Similar to the trend in proton chemical shifts discussed above, the deprotonated anhydrides reveal more pronounced change in computed ^{31}P NMR signatures than in case of neutral condensation. Thus, by means of ab-initio phosphorous NMR calculations the possible geometry and the charge of the anhydride defects can be determined.

6. PROTON CONDUCTING MATERIALS BASED ON PHOSPHONIC ACID DERIVATIVES

Chapter 7

Summary

In this thesis work, three molecular systems of very different types have been investigated by means of first principles electronic structure calculations based on density functional theory under periodic boundary conditions. The central quantities of interest were the local hydrogen bonding, as one of the most prominent structural driving forces eventually responsible for the physical and chemical properties of the considered systems, and spectroscopic features of characteristic local structures and hydrogen bonding conformations.

In Chapter 4, the initial steps of the water adsorption process on metallic nickel surfaces have been considered. The adsorption of water oligomers, both on a perfect (flat) surface and on a surface with a periodic step defect has been investigated. Of particular interest have been the interplay of hydrogen bonding between the water molecules and the water-surface interaction, and the role of a step defect. The energetics, the electronic density rearrangements and the changes in IR vibrational modes and frequencies upon adsorption have been determined.

From computed adsorption energies an increased binding strength on the step defect and in "top" geometries for both surface types has been found. The findings are in good agreement with previous theoretical and experimental results for

similar systems (130), where an energetic enhancement of water adsorption was found along step defects on platinum surfaces.

The electronic density difference maps show that additional water molecules tend to strengthen the nickel–oxygen bond. This effect leads to a significant stabilization of the binding of the first water molecule and to strongly increased binding energies of the dimer and trimer complexes, which can definitively compete with those found in liquid water.

Furthermore, the vibrational properties of water oligomers adsorbed on flat and stepped nickel surfaces are investigated. The changes in the stretch and bending modes as well as the frequencies of the new water-nickel modes which appear due to adsorption have been calculated. The dependencies of computed IR frequencies on the surface type and on the hydrogen bonding situation are consistent with adsorption energy calculations and electronic density difference maps. Complementary to this, the calculated IR spectra provide an opportunity to verify theoretical results by available experimental data. Although the agreement with experiment is qualitative, the overall accuracy of ab-initio calculations is sufficient to characterize vibrational modes and distinguish between relevant adsorption sites (perfect surface or step defect) and sizes of adsorbed clusters.

In Chapter 5, a combined experimental and ab-initio study of the ^{1}H NMR chemical shift resonance of aqueous hydrochloride (HCl) solutions has been presented. Apart from pure water as a reference system, dilute (2.6M) and concentrated (4.9M) acid solutions have been considered.

A variety of H-bonding network arrangements in liquid water and acidic solutions has been revealed by means of computed proton chemical shifts histograms. The specific features of solvated hydronium cations and chlorine anions as well as the dependence on HCl concentration have been reflected in chemical shift distributions of acidic samples. While the shape of the acidic distributions around

their central peaks is still of Gaussian type like for liquid water, they exhibit a significantly more pronounced tail towards positive δ-values. Their intensity is almost twice as strong for the higher acid concentration.

Due to the very fast molecular motion at ambient conditions, there is a steady exchange between the water molecules from the hydronium ions, from the chlorine solvation shell, and regular water. Hence, the NMR experiment only shows a single resonance line, which is the statistical average over the water molecules in these three categories. From the first-principles calculations, however, the individual ^{1}H NMR signatures of the different complexes are available, which allows us to clarify the origin of the computed chemical shift distributions. This data reveals in unprecedented detail the correlation between microscopic configurations and resulting chemical shifts in this class of systems, giving access to structure-property relationships which are difficult to obtain from experiment alone. It has been shown that the contributions of Eigen and Zundel ions, regular water molecules and the chlorine solvation shell to the ^{1}H NMR resonance line are actually very distinct and almost independent of the acid concentration. The average chemical shifts are in very good agreement with experiment for both diluted and concentrated acid solutions.

Chapter 6 has reported a first principles analysis of a proton conducting polymer which is a prototype for fuel cell membrane materials. The poly(vinyl phosphonic acid) (PVPA) contains a high concentration of acid groups and adopts a simple structure. It forms a strong hydrogen bonding network involving both P=O and P-OH as proton acceptor and proton donor groups. The hydrogen bonding between acidic groups is the most plausible candidate for the short-range proton transfer, which will in turn lead to a percolation phenomenon and long-range proton conduction. Therefore, the work has been focused on the description of *local* H-bonding network and on calculations of ^{1}H NMR signatures

of regular acidic groups and polymer defects which may effect the proton conduction. Three modifications of the polymer: PVPA with regular POH groups, with an anhydride defect (resulting from the "condensation" of two phosphonic acid groups) and with negatively charged (deprotonated) acidic group have been investigated.

Ab-initio MD simulations have been performed to find possible local H-bonding arrangements of regular PVPA, as well as possible configurations of anhydrides and deprotonated POH groups. They have revealed that proton vacancies are attracted and trapped by the anhydride defects, which indicates that condensation defects may inhibit proton conduction in two ways, first via reducing the number of available OH groups, and secondly by immobilizing proton vacancies, which may occur in PVPA by spontaneous dissociation of phosphonic acid.

Furthermore, spectroscopic calculations have provided chemical shift signatures of regular acidic groups and the neutral and negatively charged anhydride defects. It has been found that the protons of a neutral anhydride have a significantly higher NMR chemical shift than those of regular POHs and the presence of a negative charge on the anhydride enhances this effect.

In order to estimate a possible temperature effect on the structural properties and the chemical shift spectra, the MD simulations and spectroscopic NMR calculations at T=200K and T=300K have been performed. It has been found that the hydrogen bonding network of the polymer backbone and regular POH groups appears to be unaffected, since no significant difference between the two temperatures could be seen in their calculated NMR lines. Contrary to this, neutral and deprotonated anhydride defects demonstrate the same temperature dependence trend: increase of chemical shift with decreasing temperature, which indicates the strengthening of the hydrogen bonding network around the defect.

The computed high-frequency shift for the anhydrides defects with respect to

regular PVPA, which is about 4-5ppm, and their temperature dependence trends are consistent with experimental data obtained by Young Joo Lee in her high resolution solid-state NMR studies (71).

Finally, a dependence of phosphorous NMR chemical shifts on changes in the spatial arrangement of the protons and their H-bonding network has been investigated. The ab-initio ^{31}P NMR chemical shift signatures have been computed for three small fragments of PVPA chains, which represent regular PVPA structure and anhydride defects. From these calculations, the influence of the dissociation effect on the phosphorous chemical shifts has been determined. It has been found that the condensation of neighboring phosphonic groups for both intra- and inter-chain geometries leads to a noticeable increase in the ^{31}P nuclear shieldings. Similar to the trend in proton chemical shifts discussed above, the deprotonated anhydrides have shown more pronounced change in computed ^{31}P NMR signatures than in case of neutral condensation. Thus, by means of ab-initio phosphorous NMR calculations possible geometry and charge of the anhydride defects can be determined.

The findings of this thesis confirm that the symbiotic combination of ab-initio calculations and spectroscopic experiments allowing for the direct comparison of computed and measured properties provides significantly more insight into physical and chemical questions than either of these methods alone.

References

[1] B. E. Warren. *X-Ray Diffraction*. Dover, Mineola, 1990. 3, 79

[2] S. W. Lovesey, Ed. *Theory of Neutron Scattering from Condensed Matter*. Oxford University Press, 1988. 3

[3] U. Kolb and G. Matveeva. *Z. Kristallogr.*, **2003**, *218*, 259–268. 3

[4] B. Ruckert and U. Kolb. *Micron*, **2005**, *36*, 247–260. 3

[5] N. B. Colthup, L. H. Daly and S. E. Wiberley. *Introduction to infrared and Raman spectroscopy*. Academic Press, New York, 1975. 3, 35, 79

[6] R. R. Ernst, G. Bodenhausen and A. Wokaun. *Principles of Nuclear Magnetic Resonance in One and Two Dimensions*. Clarendon Press Oxford, 1987. 3, 9

[7] K. Wüthrich. *NMR of Proteins and Nucleic Acids*. Wiley, New York, 1986. 3, 9

[8] B. Hetényi, F. D. Angelis, P. Giannozzi and R. Car. *J. Chem. Phys.*, **2004**, *120*, 8632–8637. 3, 6, 81

[9] B. Hetenyi, F. D. Angelis, P. Giannozzi and R. Car. *J. Chem. Phys.*, **2006**, *124*, 099901. 3, 6, 81

[10] P. L. Silvestrelli, M. Bernasconi and M. Parrinello. *Chem. Phys. Lett.*, **1997**, *277*, 478–482. 3, 5, 80, 83

[11] P. Umari and A. Pasquarello. *Diam. rel. mat.*, **2005**, *14*, 1255–1261. 3

[12] W. Thiel. *Chimia*, **2004**, *58*, 276–280. 3

[13] V. van Speybroeck and R. Meier. *Chemical Society Reviews*, **2003**, *32*, 151. 3

[14] R. Iftimie and M. Tuckerman. *J. Chem. Phys.*, **2005**, *122*, 214508. 3

[15] C. J. Jameson and A. C. de Dios. *Nuc. Mag. Res.*, **2004**, *33*, 47–75. 3

[16] M. Bühl, M. Kaupp, O. L. Malkina and V. Malkin. *J. Comput. Chem.*, **1999**, *20*, 91–105. 3

[17] M. Kaupp, M. Bühl, M. Malkin and G. Vladimir, Eds. *Calculations of NMR and EPR parameters*. Wiley-VCH, Weinheim, 2004. 3

[18] G. Goward, D. Sebastiani, I. Schnell and H. W. Spiess. *J. Am. Chem. Soc.*, **2003**, *125*, 5792–5800. 3

[19] J. R. Yates, T. N. Pham, C. J. Pickard, F. Mauri, A. M. Amado, A. M. Gil and S. P. Brown. *J. Am. Chem. Soc.*, **2005**, *127*, 10216–10220. 3, 96

[20] C. Gervais, R. Dupree, K. J. Pike, C. Bonhomme, M. Profeta, C. J. Pickard and F. Mauri. *J. Phys. Chem. A*, **2005**, *109*, 6960–6969. 3

[21] J. Schmidt and D. Sebastiani. *J. Chem. Phys.*, **2005**, *123*, 074501. 3, 105

[22] M. Schulz-Dobrick, T. Metzroth, H. W. Spiess, J. Gauss and I. Schnell. *ChemPhysChem*, **2005**, *6*, 315–327. 3

[23] B. Pfrommer, F. Mauri and S. Louie. *J. Am. Chem. Soc.*, **2000**, *122*, 123–129. 3, 5, 84, 96

[24] D. Sebastiani and M. Parrinello. *ChemPhysChem*, **2002**, *3*, 675. 3, 5, 84, 88, 96

[25] M. Gaigeot and M. Sprik. *J. Chem. Phys.*, **2003**, *107*, 10344–10358. 3, 6, 80

[26] F. C. Lightstone, E. Schwegler, M. Allesch, F. Gygi and G. Galli. *ChemPhysChem*, **2005**, *6*, 1745–1749. 3, 6, 80

[27] K. Laasonen, M. Sprik, M. Parrinello and R. Car. *J. Chem. Phys.*, **1993**, *99*, 9080–9089. 5, 6, 80

[28] P. Silvestrelli and M. Parrinello. *J. Chem. Phys.*, **1999**, *111*, 3572. 5, 6, 80

[29] M. Sharma, R. Resta and R. Car. *Phys. Rev. Lett.*, **2005**, *95*, 187401. 5

[30] A. Putrino and M. Parrinello. *Phys. Rev. Lett.*, **2002**, *88*, 176401. 5

[31] M. A. Henderson. *Surf. Sc. Rep.*, **2002**, *46*, 1–308. 5, 50

[32] R. Ludwig. *Angew. Chem. Int. Ed. Engl.*, **2003**, *42*, 3458–3460. 5, 50

[33] D. Sebastiani and L. Delle Site. *J. Chem. Theory Comp.*, **2005**, *1*, 78–82. 5, 51, 53, 58, 59, 60, 61, 62

[34] A. Michaelides, A. Alavi and D. A. King. *Phys. Rev. B*, **2004**, *69*, 113404. 5, 53

[35] H. Over and A. P. Seitsonen. *Science*, **2002**, *297*, 2003–2005. 5

[36] T. Murakhtina, L. Delle Site and D. Sebastiani. *ChemPhysChem*, **2006**, *7*, 1215–1219. 5

[37] M.Nakamura and M.Ito. *Chem. Phys. Lett.*, **2004**, *384*, 256. 5, 75, 76, 77

[38] J. Ruczhowski. *Catalysis Today*, **2001**, *68*, 263. 6

[39] B. Weckhuysen. *Phys. Chem. Chem. Phys.*, **2003**, *5*, 4351. 6

[40] M. Sprik, J. Hutter and M. Parrinello. *J. Chem. Phys.*, **1996**, *105*, 1142. 6, 80, 83

[41] J. VandeVondele, F. Mohamed, M. Krack, J. Hutter, M. Sprik and M. Parrinello. *J. Chem. Phys.*, **2005**, *122*, 014515. 6, 82, 85

[42] S. Raugei and M. Klein. *J. Chem. Phys.*, **2002**, *116*, 196–202. 6, 80

[43] T. von Rosenvinge, M. E. Tuckerman and M. L. Klein. *Farad. Disc.*, **1997**, *106*, 273–289. 6, 80

[44] A. J. Sillanpaa, C. S. C, M. L. Klein and K. Laasonen. *J. Phys. Chem. B*, **2002**, *106*, 11315–11322. 6, 80

[45] S. L. Raugei and M. L. Klein. *ChemPhysChem*, **2004**, *5*, 1569–1576. 6, 80

[46] C. Simon and M. L. Klein. *ChemPhysChem*, **2005**, *6*, 148–153. 6, 80

[47] J. M. Heuft and E. J. Meijer. *Phys. Chem. Chem. Phys.*, **2006**, *8*, 3116–3123. 6, 80, 82, 91, 92, 95

[48] M. Boero, T. Ikeshoji and K. Terakura. *ChemPhysChem*, **2005**, *6*, 1775–1779. 6, 80

[49] A. K. Soper, F. Bruni and M. A. Ricci. *J. Chem. Phys.*, **1997**, *106*, 247. 7

[50] A. K. Soper. *Chem. Phys.*, **2000**, *258*, 121. 7

[51] J.M.Sorenson, G.Hura, R. Glaeser and T. Head-Gordon. *J. Chem. Phys.*, **2000**, *113*, 9149. 7

[52] S. Sharif, G. Denisov, M. Toney and H. Limbach. *J. Am. Chem. Soc.*, **2006**, *128*, 3375–3387. 7

[53] B. Grunberg, T. Emmler, E. Gedat, J. Shenderovich, G. H. Findenegg, H. H. Limbach and G. Buntkowsky. *Chem. Eur. J.*, **2004**, *10*, 5689–5696. 7

[54] S. P. Brown and H. W. Spiess. *Chem. Rev.*, **2001**, *101*, 4125. 7, 9

[55] D. Sakellariou, S. P. Brown, A. Lesage, S. Hediger, M. Bardet, C. A. Meriles, A. Pines and L. Emsley. *J. Am. Chem. Soc.*, **2003**, *125*, 4376–4380. 7, 9

[56] L. Duma, S. Hediger, B. Brutscher, A. Bockmann and L. Emsley. *J. Am. Chem. Soc.*, **2003**, *125*, 11816–11817. 7, 9

[57] G. Wulff, B. O. Chong and U. Kolb. *Angew. Chem. Int. Ed. Engl.*, **2006**, *45*, 2955–2958. 7

[58] P. M. Tolstoy, P. Schah-Mohammedi, S. N. Smirnov, N. S. Golubev, G. S. Denisov and H. H. Limbach. *J. Am. Chem. Soc.*, **2004**, *126*, 5621–5634. 7

[59] M. Wanko, M. Hoffmann, P. Strodet, A. Koslowski, W. Thiel, F. Neese, T. Frauenheim and M. Elstner. *J. Phys. Chem. B*, **2005**, *109*, 3606–3615. 7

[60] T. Murakhtina, J. Heuft, J.-E. Meijer and D. Sebastiani. *ChemPhysChem*, **2006**, *7*, 2578–2584. 7

[61] K. D. Kreuer. *Ann. rev. mater. res.*, **2003**, *33*, 333–359. 8

[62] K. D. Kreuer, S. J. Paddison, E. Spohr and M. Schuster. *Chem. Rev.*, **2004**, *104*, 4637–4678. 8

[63] K. D. Kreuer. *J. membr. sci.*, **2001**, *185*, 29–39. 8

[64] H. W. Spiess. *J. Polymer Sci. Part A*, **2004**, *42*, 5031–5044. 8, 9

[65] K. Kordesh and G. Simader. *Fuel Cells and Their Applications*, **1996**, *38*. 8, 101

[66] K. D. Kreuer, A. Rabenau and W. Weppner. *Angew. Chem.*, **1982**, *94*, 224. 8, 101

[67] R. P. Sijbesma, F. H. Beijer, L. Brunsveld, B. J. B. Folmer, J. H. K. K. Hirschberg, R. F. M. Lange, J. K. L. Lowe and E. W. Meijer. *Science*, **1997**, *278*, 1601–1604. 9

[68] I. Schnell. *Curr. anal. chem.*, **2005**, *1*, 3–27. 9

[69] H. W. Spiess. *Macromol. Chem. Phys.*, **2003**, *204*, 340–346. 9

[70] H. W. Spiess. *J. Polym. Sci.*, **2004**, *A 42*, 5031–5044. 9

[71] Y. J. Lee, B. Bingol, T. Murakhtina, D. Sebastiani, J. H. Ok, W. H. Meyer, G. Wegner and H. W. Spiess. *J. Phys. Chem. B (accepted)*. 10, 105, 111, 112, 113, 114, 115, 125

[72] P. Hohenberg and W. Kohn. *Phys. Rev.*, **1964**, *136*, B864. 11, 15

[73] W. Kohn and L. J. Sham. *Phys. Rev.*, **1965**, *140*, A1133. 11, 16

[74] R. O. Jones and O. Gunnarsson. *Rev. Mod. Phys.*, **1989**, *61*, 689–746. 11, 20

[75] R. G. Parr and W. Yang. *Density functional theory of atoms and molecules.* Oxford Science Publications, 1989. 11, 13

[76] Ashcroft. *Solid state physics.* Saunders, Philadelphia, 1976. 13, 25

[77] D. Marx, M. Tuckerman, J. Hutter and M. Parrinello. *Nature*, **1999**, *397*, 601. 14

[78] S. Raugei and M. Klein. *ChemPhysChem*, **2004**, *5*, 1569. 14

[79] D. Marx. *ChemPhysChem*, **2006**, *7*, 1848. 14

[80] M. Benoit, D. Marx and M. Parrinello. *Nature*, **1998**, *392*, 258. 14

[81] M. Tuckerman, D.Marx, M. Klein and M. Parrinello. *J. Chem. Phys.*, **1996**, *104*, 5579–5588. 14, 84

[82] D. Marx and M. Parrinello. *Z. Phys. B Cond. Mat.*, **1994**, *95*, 143–144. 14

[83] E. E. Pickett. *Comput. Phys. Reports*, **1989**, *9*, 115. 18

[84] S. Lundqvist and N. H. March, Eds. *Theory of the inhomogeneous electron gas.* Plenum Press, New York, 1983. 20

[85] D. M. Ceperley and B. J. Alder. *Phys. Rev. Lett.*, **1980**, *45*, 566. 20

[86] J. Perdew and A. Zunger. *Phys. Rev. B*, **1981**, *23*, 5048. 20

[87] P. Giannozzi, S. de Gironcoli, P. Pavone and S. Baroni. *Phys. Rev. B*, **1991**, *43*, 7231. 21

[88] X. Gonze, D. C. Allan and M. P. Teter. *Phys. Rev. Lett.*, **1992**, *68*, 3603. 21

[89] C. S. Wang, B. M. Klein and H. Krakauer. *Phys. Rev. Lett.*, **1985**, *54*, 1852. 21

[90] K. B. J. Perdew and M.Ernzerhof. *Phys. Rev. Lett.*, **1996**, *77*, 3865. 21

[91] A. D. Becke. *Phys. Rev. A*, **1988**, *38*, 3098. 21, 83, 104

[92] C. Lee, W. Yang and R. G. Parr. *Phys. Rev. B*, **1988**, *37*, 785–789. 21, 83, 104, 115

[93] D. R. Hamann, M. Schluter and C. Chiang. *Phys. Rev. Lett.*, **1979**, *43*, 1494. 23

[94] G. B. Bachelet, D. R. Hamann and M. Schluter. *Phys. Rev. B*, **1982**, *26*, 4199. 23

[95] N. Troullier and J. L. Martins. *Phys. Rev. B*, **1991**, *43*, 1993. 23, 52

[96] S. Goedecker, M. Teter and J. Hutter. *Phys. Rev. B*, **1996**, *54*, 1703. 23, 83, 104

[97] L. Kleinman and D. M. Bylander. *Phys. Rev. Lett.*, **1982**, *48*, 1425. 23

[98] P. Pulay. *Mol. Phys.*, **1969**, *17*, 197. 24

[99] W. H. Press, S. A. Teukoldky, W. T. Vetterling and B. P. Flannery. *Numerical recipes*. Cambridge University Press, 2 edition, 1992. 24

[100] J. Hutter et al. Computer code CP2K. `http://www.cp2k.org`. 24

[101] D. J. Chadi and M. L. Kohen. *Phys. Rev. B*, **1973**, *8*, 5747. 26

[102] H. J. Monkhorst and J. D. Pack. *Phys. Rev. B*, **1973**, *13*, 5188. 26, 32, 52

[103] J. Moreno and J. M. Soler. *Phys. Rev. B*, **1992**, *45*, 13891. 26

[104] R. Car and M. Parrinello. *Phys. Rev. Lett.*, **1985**, *55*, 2471. 28

[105] J. C. Grossman, E. Schwegler, E. W. Draeger, F. Gygi and G. Galli. *J. Chem. Phys.*, **2003**, *120*, 300–311. 28, 85

[106] A. Alavi, J. Kohanoff, M. Parrinello and D. Frenkel. *Phys. Rev. Lett.*, **1994**, *73*, 2599. 30, 31, 52

[107] M. Mermin. *Phys. Rev.*, **1965**, *137*, A1441. 30

[108] P. L. Silvestrelli, A. Alavi, M. Parrinello and D. Frenkel. *Europhys. Lett.*, **1996**, *33*, 551–556. 31, 52

[109] P. L. Silvestrelli, A. Alavi, M. Parrinello and D. Frenkel. *Phys. Rev. B*, **1996**, *53*, 12750–12760. 31

[110] D. McQuarrie. *Statistical Mechanics*. University Science Books, Sausalito, CA, 2000. 36

[111] J. Bader and B. Berne. *J. Chem. Phys.*, **1994**, *100*, 8359. 37

[112] A. Putrino, D. Sebastiani and M. Parrinello. *J. Chem. Phys.*, **2000**, *113*, 7102–7109. 39, 41, 42

[113] D. Sebastiani and M. Parrinello. *J. Phys. Chem. A*, **2001**, *105*, 1951. 41, 43, 44, 46, 84, 104

[114] H. Goldstein. *Classical mechanics*. Addison-Wesley, 1980. 42

[115] T. A. Keith and R. F. W. Bader. *Chem. Phys. Lett.*, **1993**, *210*, 223. 43

[116] K. Kobayashi and M. Tsukada. *Phys. Rev. B*, **1988**, *38*, 8566–8578. 44

[117] F. Mauri and S. Louie. *Phys. Rev. Lett.*, **1996**, *76*, 4246–4249. 44

[118] F. Mauri, B. Pfrommer and S. Louie. *Phys. Rev. Lett.*, **1996**, *77*, 5300–5303. 44

[119] D. Sebastiani, G. Goward, I. Schnell and H. W. Spiess. *J. Mol. Struct. (THEOCHEM)*, **2003**, *625*, 283–288. 44, 84

[120] G. Berghold, C. Mundy, A. Romero, J. Hutter and M. Parrinello. *Phys. Rev. B*, **2000**, *61*, 10040. 44

[121] W. Kohn. *Phys. Rev.*, **1959**, *115*, 809. 44

[122] D. Marx and J. Hutter. in *Modern Methods and Algorithms in Quantum Chemistry*, volume 1 of *NIC Series*, pp 301–449. Forschungzentrum Juelich, 2000. 46

[123] T. Housman, J. Feliu, R. Gomez and M. Koper. *ChemPhysChem*, **2005**, *6*, 1522. 49

[124] D. Nieskens, D. Ferre and J. Niemantsverdriet. *ChemPhysChem*, **2005**, *6*, 1293. 49

[125] D. Ferre, A. van Bavel and J. Niemantsverdriet. *ChemPhysChem*, **2005**, *6*, 473. 49

[126] O. Inderwildi, D. Lebiedz, O. Deutschmann and J. Warnatz. *ChemPhysChem*, **2005**, *6*, 2513. 49

[127] P. J. Feibelman. *Science*, **2002**, *295*, 99–102. 50

[128] D. Menzel. *Science*, **2002**, *295*, 58–59. 50

[129] T. Mitsui, M. K. Rose, E. Fomin, D. G. Ogletree and M. Salmeron. *Science*, **2002**, *297*, 1850–1852. 50

[130] M. L. Grecea, E. H. G. Backus, B. Riedmüller, A. Eichler, A. W. Kleyn and M. Bonn. *J. Phys. Chem. B*, **2004**, *108*, 12575–12582. 50, 77, 122

[131] S. Meng, L. F. Xu, E. G. Wang and S. Gao. *Phys. Rev. Lett.*, **2002**, *89*, 176104. 50

[132] P. Feibelman. *Phys. Rev. Lett.*, **2003**, *91*, 059601. 50

[133] S. Meng, L. F. Xu, E. G. Wang and S. Gao. *Phys. Rev. Lett.*, **2003**, *91*, 059602. 50

[134] A. Michaelides, V. A. Ranea, P. L. de Andres and D. A. King. *Phys. Rev. Lett.*, **2003**, *90*, 216102. 50, 59

[135] V. A. Ranea, A. Michaelides, R. Ramírez, J. A. Vergès, P. L. de Andres and D. A. King. *Phys. Rev. B*, **2004**, *69*, 205411. 50, 59

[136] J. Cerdá, A. Michaelides, M.-L. B. P. J. Feibelman, T. Mitsui, M. Rose, E. Fomin and M. Salmeron. *Phys. Rev. Lett.*, **2004**, *93*, 116101. 50

[137] V. A. Ranea, A. Michaelides, R. Ramírez, P. L. de Andres, J. A. Vergés and D. A. King. *Phys. Rev. Lett.*, **2004**, *92*, 136104. 50, 59

[138] L. Delle Site and D. Sebastiani. *Phys. Rev. B*, **2004**, *70*, 115401. 51, 59, 63

[139] S. Dahl, A. Logadottir, R. C. Egeberg, J. H. Larsen, I. Chorkendorff, E. Törnqvist and J. K. Nørskov. *Phys. Rev. Lett.*, **1999**, *83*, 1814. 51

[140] M. Mavrikakis, M. Bäumer, H. J. Freund and J. K. Nørskov. *Catal. Lett.*, **2002**, *81*, 153. 51

[141] V. Shah, T. Li, K. L. Baumert, H. S. Cheng and D. S. Sholl. *Surf. Sc.*, **2003**, *537*, 217. 51

[142] J. B. Hannon, M. Copel, R. Stumpf, M. Reuter and R. Tromp. *Phys. Rev. Lett.*, **2004**, *92*, 216104. 51

[143] P. et al. *Phys. Rev. Lett.*, **2005**, *94*, 246104. 52

[144] H. H.Zaidi and D.Paulmier. *Appl. Surf. Science*, **1993**, *70*, 180. 52

[145] M. Lee. *Ph.D. thesis*. Cambridge University, 1995. 52

[146] J. Perdew, K. Burke and M.Ernzerhof. *Phys. Rev. Lett.*, **1996**, *77*, 3865. 52

[147] P. Flükiger, H. P. Lüthi, S. Portmann and J. Weber. Molecular visualization program MOLEKEL, version 4.0. Swiss Center for Scientific Computing, Manno (Switzerland), 2000. 54

[148] F. Huisken, M. Kaloudis and A. Kulcke. *J. Chem. Phys.*, **1996**, *104*, 17 and references therein. 56

[149] M. Kolaski, H. Lee, Y. Choi, K. Kim, P. Tarakeshwar, D. Miller and J. Lisy. *J. Chem. Phys.*, **2007**, *126*, 074302. 56

[150] B. N. L. Fredin and G. Ribbegrd. *J. Chem. Phys.*, **1977**, *66*, 4065. 56

[151] A. Soper and P. Rossky. *Chem. Phys.*, **2000**, *258*, 107–108. 79

[152] P. Wernet, D. Nordlund, U. Bergmann, M. Cavalleri, M. Odelius, H. Ogasawara, L. Naslund, T. Hirsch, L. Ojamae, P. Glatzel, L. G. M. Pettersson and A. Nilsson. *Science*, **2004**, *304*, 995–999. 79, 87

[153] J. D. Smith, C. D. Cappa, K. R. Wilson, B. M. Messer, R. C. Cohen and R. J. Saykally. *Science*, **2004**, *306*, 851–853. 79, 87

[154] A. Nilsson, P. Wernet, D. Nordlund, U. Bergmann, M. Cavalleri, M. Odelius, M. Cavalleri, M. Odelius, H. Ogasawara, L.-Å. Naslund, T. K. Hirsch, L. Ojamae, P. Glatzel and L. G. M. Pettersson. *Science*, **2005**, *308*, 793a. 79, 87

[155] J. D. Smith, C. D. Cappa, K. R. Wilson, B. M. Messer, R. C. Cohen and R. J. Saykally. *Science*, **2005**, *308*, 793b. 79, 87

[156] E. Pines, D. Pines, Y. Z. Ma and G. R. Fleming. *ChemPhysChem*, **2004**, *5*, 1315–1327. 79

[157] I.-F. W. Kuo, C. J. Mundy, M. J. McGrath, J. I. Siepmann, J. VandeVondele, M. Sprik, J. Hutter, B. Chen, M. L. Klein, F. Mohamed, M. Krack and M. Parrinello. *J. Phys. Chem. B*, **2004**, *108*, 12990–12998. 82, 85

[158] C. Hartwigsen, S. Goedecker and J. Hutter. *Phys. Rev. B*, **1998**, *58*, 3641. 83, 104

[159] D. Sebastiani. *Mod. Phys. Lett. B*, **2003**, *17*, 1301–1319. 83, 85

[160] M. Tuckerman, D.Marx, M. Klein and M. Parrinello. *Science*, **1997**, *275*, 817–820. 84

[161] S. Rossano, F. Mauri, C. J. Pickard and I. Farnan. *J. Phys. Chem. B*, **2005**, *198*, 7245–7250. 84

[162] P. Vidossich, S. Piana, A. Miani and P. Carloni. *J. Am. Chem. Soc.*, **2006**, *128*, 7215–7221. 84

[163] M. D. Fenn and E. Spinner. *J. Phys. Chem.*, **1984**, *88*, 3993–3997. 84

[164] D. Sebastiani. *ChemPhysChem*, **2006**, *7*, 164–175. 84

[165] J. Hutter et al. Computer code CPMD, version 3.12, 1990-2005. Copyright IBM Corp. and MPI-FKF Stuttgart, `http://www.cpmd.org`. 86, 104

[166] J. Hutter and A. Curioni. *ChemPhysChem*, **2005**, *6*, 1788–1793. 86

[167] T. Gregor, F. Mauri and R. Car. *J. Chem. Phys.*, **1999**, *111*, 1815–1822. 96

[168] J. R. Yates, S. E. Dobbins, C. J. Pickard, F. Mauri, P. Y. Ghi and R. K. Harris. *Phys. Chem. Chem. Phys.*, **2005**, *7*, 1402–1407. 96

[169] K. Mauritz and R. Moore. *Chem. Rev.*, **2004**, *104*, 4535. 99

[170] K. D. Kreuer, A. Fuchs, M. Ise, M. Spaeth and J. Maier. *Electrochimica Acta*, **1998**, *43*, 1281. 100

[171] H. Hez, K. D. Kreuer, J. Maier, G. Scharfenberger, M. Schuster and W. Meyer. *Electrochimica Acta*, **2003**, *48*, 2165. 100

[172] S. Lee, G. Scharfenberger, W. Meyer and G. Wegner. *Adv. Mater.*, **2005**, *17*, 626. 100

[173] R. Service. *Science*, **2006**, *312*, 35. 100

[174] N. Greenwood and A. Thompson. *J. Chem. Soc.*, **1959**, p 3485. 100

[175] T. Dippel, K. Kreuer, J. Lassegues and D. Rodriguez. *Solid State Ionics*, **1993**, *61*, 41. 100

[176] S. W. Peterson, E. Gebert, A. H. Reis, M. E. Druyan, G. W. Mason and D. Perrard. *J. Phys. Chem.*, **1977**, *81*, 446. 103, 105

[177] R. Harris, P. Jackson, L. Merwin and B. Say. *J. Chem. Soc. Farad. Trans.*, **1988**, *84*, 3649. 103, 105

[178] J. Schmidt, A. Hoffmann, H. W. Spiess and D. Sebastiani. *J. Phys. Chem. B*, **2006**, *110*, 23204–23210. submitted. 105

[179] J. Baschnagel, K. Binder, P. Doruker, A. A. Gusev, O. Hahn, K. Kremer, W. L. Mattice, F. Muller-Plathe, M. Murat, W. Paul, S. Santos, U. W. Suter and V. Tries. *Adv. polym. sci.*, **2000**, *152*, 41–156. 107

[180] L. Delle Site, C. F. Abrams, A. Alavi and K. Kremer. *Phys. Rev. Lett.*, **2002**, *89*, 156103. 107

[181] S. Leon, N. van der Vegt, D. Site and K. Kremer. *Macromol*, **2005**, *38*, 8078. 107

[182] B. Hess, S. Leon, N. van der Vegt and K. Kremer. *Soft Matter*, **2006**, *2*, 409. 107

[183] A. Rapp, I. Schnell, D. Sebastiani, S. P. Brown, V. Percec and H. W. Spiess. *J. Am. Chem. Soc.*, **2003**, *125*, 13284–13297. 108

[184] A. D. Becke. *J. Chem. Phys.*, **1993**, *98*, 5648–5652. 115

[185] R. Ditchfield. *J. Chem. Phys.*, **1972**, *56*, 5688. 116

[186] M. J. Frisch, G. W. Trucks, H. B. Schlegel, G. E. Scuseria, M. A. Robb, J. R. Cheeseman, J. A. Montgomery, Jr., T. Vreven, K. N. Kudin, J. C. Burant, J. M. Millam, S. S. Iyengar, J. Tomasi, V. Barone, B. Mennucci, M. Cossi, G. Scalmani, N. Rega, G. A. Petersson, H. Nakatsuji, M. Hada, M. Ehara, K. Toyota, R. Fukuda, J. Hasegawa, M. Ishida, T. Nakajima, Y. Honda, O. Kitao, H. Nakai, M. Klene, X. Li, J. E. Knox, H. P. Hratchian, J. B. Cross, C. Adamo, J. Jaramillo, R. Gomperts, R. E. Stratmann, O. Yazyev, A. J. Austin, R. Cammi, C. Pomelli, J. W. Ochterski, P. Y. Ayala, K. Morokuma, G. A. Voth, P. Salvador, J. J. Dannenberg, V. G. Zakrzewski,

S. Dapprich, A. D. Daniels, M. C. Strain, O. Farkas, D. K. Malick, A. D. Rabuck, K. Raghavachari, J. B. Foresman, J. V. Ortiz, Q. Cui, A. G. Baboul, S. Clifford, J. Cioslowski, B. B. Stefanov, G. Liu, A. Liashenko, P. Piskorz, I. Komaromi, R. L. Martin, D. J. Fox, T. Keith, M. A. Al-Laham, C. Y. Peng, A. Nanayakkara, M. Challacombe, P. M. W. Gill, B. Johnson, W. Chen, M. W. Wong, C. Gonzalez and J. A. Pople. Computer code Gaussian 03, Revision B.03, 2004. 116